CONCEPTUAL DEVELOPMENT OF REMOTE MONITORING SYSTEM FOR PRESSURIZED WATER REACTOR SPENT FUEL DRY CASK STORAGE THROUGH NEUTRON AND GAMMA TRANSPORT SIMULATIONS

A Thesis

by

ALEXANDRA PETROVNA KHUDOLEEVA

Submitted to the Office of Graduate Studies of
Texas A&M University
in partial fulfillment of the requirements for the degree of

MASTER OF SCIENCE

Approved by:

Chair of Committee,	Sunil S. Chirayath
Co-Chair of Committee,	William S. Charlton
Committee Member,	Charles M. Folden III
Head of the Department,	Yassin A. Hassan

May 2013

Major Subject: Nuclear Engineering

ABSTRACT

The International Atomic Energy Agency (IAEA) needs to enhance its capabilities for safeguarding spent nuclear fuel (SNF) stored in dry cask storage facilities and for maintaining persistent continuity of knowledge (CoK) about it. The current safeguards approach relies heavily upon containment and surveillance measures, where seals are placed inside and outside the dry cask. The disadvantage of this approach is that, if a seal is broken, no method currently exists to verify the dry cask content other than opening it and checking the internal seal and the SNF inside. This is a costly and difficult activity. Thus other measures need to be developed. This study focused on the development of a remote monitoring system (RMS) for dry cask storage which is capable of detecting neutron and gamma radiation emitted by the SNF and the signal thus generated can then be continually transmitted to the IAEA to maintain the CoK about the dry cask content. The remote option was chosen after reviewing the current IAEA needs.

A computational approach was used to develop the proposed RMS. Monte Carlo N-Particle transport code (MCNP) was employed to develop a dry cask model with 32 SNF assemblies inside. The ORIGEN-ARP, fuel burn-up and depletion code, was used to generate a radiation source-term. A series of MCNP simulations were performed to investigate the neutron and gamma flux behavior inside the dry cask. The results of these simulations aided the design of the RMS and determination of the optimal location for its components. The RMS was placed inside the dry cask on the top of the multi-purpose canister (MPC). The final conceptual design of the RMS included two fission chambers (to detect neutrons) and one ionization chamber (to detect gamma radiation) enclosed in a polyethylene box with a thin cadmium plate inside, so the sequence of layers starting from the MPC lid was: polyethylene bottom layer, cadmium plate, chambers enclosed in polyethylene and polyethylene layer on top. Such configuration provided a suppression effect for thermal neutron flux coming from the bottom SNF assemblies and made system more sensitive to the opening of the dry cask lid and removal of SNF assemblies from the peripheral MPC cells. The proposed

RMS design was tested through diversion analysis. The fission chamber unit design was successfully able to detect all the SNF diversion scenarios studied. The ionization chambers were able to detect only removal of SNF assemblies located just below it. However, the ionization chamber was found to be able to identify the opening of the dry cask lid through reduction in signal whenever the lid was opened. Therefore, the ionization chamber was kept in the RMS design to provide secondary confirmation for the detection of dry cask lid opening.

ACKNOWLEDGEMENTS

I would like to take this opportunity to record my thanks to the U.S Department of Education for funding my study and research, and to my Advisory Committee for their guidance and support. A special thanks to Dr. Sunil S. Chirayath for being my advisor and for his help with learning Monte Carlo N-Particle transport code. I would also like to thank Dr. William S. Charlton for valuable comments and ideas about the system design, and Dr. Charles M. Folden III for being member of my Advisory Committee.

Besides my Advisory Committee, I would like to thank Dr. Alexander Solodov and Dr. Gennady Pshakin. This thesis work would not be possible without their help with redefining the focus and scope of this study. Dr. Alexander Solodov was the author of the core idea, and Dr. Gennady Pshakin provided valuable discussion about current IAEA needs and evolution of the safeguards.

It gives me great pleasure in acknowledging the support and help from other professors at our department that spent their time with me and consulted me on different topics: Dr. Marvin L. Adams, Dr. Leslie A. Braby, and Pre-Dr. Braden Goddard.

I am indebted to Dr. David Moses for his comments and review of this work.

My deepest thanks goes to my new French and Half-French friends, Annabelle Le Coq, Kevin Dugan and Marco Delchini for their endless support and pear cakes, to my parents, family and friends for their support and belief in me, and finally to my beloved husband for his patience and love.

NOMENCLATURE

IAEA	International Atomic Energy Agency
RMS	Remote Monitoring System
CoK	Continuity of Knowledge
MPC	Multi-Purpose Canister
NPP	Nuclear Power Plant
SNF	Spent Nuclear Fuel
NRC	U.S. Nuclear Regulatory Commission
SQ	Significant Quantity
NM	Nuclear Material
C&S	Containment and Surveillance
UMS	Unattended Monitoring System
NDA	Non-Destructive Assay
PWR	Pressurized Water Reactor
MCNP	Monte Carlo N-Particle transport code
LWR	Light Water Reactor
LLNL	Lawrence Livermore National Laboratory
CANDU	Canada Deuterium Uranium reactor

TABLE OF CONTENTS

Page

ABSTRACT ii
ACKNOWLEDGEMENTS iv
NOMENCLATURE v
TABLE OF CONTENTS vi
LIST OF FIGURES viii
LIST OF TABLES x
1. INTRODUCTION 1
1.1 Background 1
1.1.1 Spent Nuclear Fuel Inventory and Storage Options 1
1.1.2 Dry Cask Storage and IAEA's Concerns 4
1.1.3 Why Remote Monitoring System for Dry Cask Storage? 6
1.2 Previous Work 9
1.3 Objective and Motivations 11
1.4 Thesis Overview 12
2. DEVELOPMENT OF THE DRY CASK COMPUTER MODEL 13
2.1 Procedure 13
2.2 MCNP Modeling 13
2.2.1 MCNP Model of a PWR Fuel Assembly 14
2.2.2 MCNP Model of a Dry Cask 16
2.3 Generation of the Radiation Source-Term for PWR Spent Fuel Assembly 18
2.4 Analytical Calculations for the MCNP Model Validation 21
3. CONCEPTUAL DESIGN DEVELOPMENT OF THE REMOTE MONITORING SYSTEM 26
3.1 Procedure 26
3.2 Derivation of Design Requirements 27
3.2.1 Inherent Dry Cask Limitations and IAEA Requirements 27
3.2.2 Investigation of the Neutron and Gamma Flux Behavior Outside and Inside the Dry Cask 27
3.2.3 Final List of Requirements to the Preliminary RMS Design 36
3.3 Type and Number of Detectors 37
3.4 Detectors Mode of Operation and Output Signal 39
3.5 Other Materials and Their Dimensions 42
3.5.1 Review of the Preliminary RMS Design 50

4. SPENT NUCLEAR FUEL DIVERSION ANALYSES 53
4.1 Procedure 53
4.2 Diversion Analysis with Neutron Radiation Signal 57
4.3 Diversion Analysis with Gammas Radiation Signal 60
4.4 Final Design of the RMS 64
5. OTHER CONSIDERATIONS OF THE REMOTE MONITORING SYSTEM 66
5.1 Representation of Data to Inspectors 66
5.2 RMS and Current Safeguards Approach to Dry Cask Storage 68
5.3 RMS Lifetime 69
5.4 RMS Cost 70
6. FUTURE WORK 72
7. SUMMARY AND CONCLUSIONS 73
REFERENCES 75
APPENDIX A MCNP INPUT FILE FOR THE DRY CASK MODEL 79
APPENDIX B RADIATION SOURCE-TERM FOR ONE PWR SNF ASSEMBLY 86
APPENDIX C TOTAL ABSORPTION CROSS-SECTION FOR CADMIUM 88
APPENDIX D MCNP INPUT FILE FOR THE SIMPLIFIED DRY CASK MODEL 89
APPENDIX E DIVERSION ANALYSIS RESULTS FOR THE FISSION CHAMBERS IN GRAPHICAL FORM AND RELATED NUMERICAL DATA 91
APPENDIX F DIVERSION ANALYSIS RESULTS FOR THE IONIZATION CHAMBERS IN GRAPHICAL FORM AND RELATED NUMERICAL DATA 94

LIST OF FIGURES

Page

Fig. 1. Three types of SNF dry storage facilities: (a) vault, (b) silo and (c) cask 2

Fig. 2. Two main components of the dry cask: (a) inner metal liner with grid inside and (b) outer concrete canister with lid 3

Fig. 3. Principal of operation of the remote monitoring system 8

Fig. 4. Typical PWR fuel assembly (a) and its MCNP model used in this study: (b) top view, (c) axial view (truncated top part of the assembly).....16

Fig. 5. MCNP model of the dry cask for PWR SNF assemblies: (a) axial view and (b) top view.....18

Fig. 6. Gamma spectrum for the PWR SNF assembly with discharge burn-up 45 GWd/Mt burned at specific power 37.5 MW/t and cooled for 3 years 19

Fig. 7. Neutron spectrum for the PWR SNF assembly with discharge burn-up 45 GWd/Mt burned at specific power 37.5 MW/t and cooled for 3 years 21

Fig. 8. Detector positions for the isotropic point source test.....24

Fig. 9. Options for the RMS location inside the dry cask: side and top air gaps 28

Fig. 10. Setup for the row test 30

Fig. 11. Flux distribution on the top of the MPC inside the dry cask 32

Fig. 12. Setup for the open lid test 34

Fig. 13. Location of fission chambers (a) with respect to the MPC center and X, Y axis, and (b) inside polyethylene box. Blue line indicates location of the cadmium plate 44

Fig. 14. A simplified MCNP model of the dry cask used for simulations aiming to optimize dimensions of the polyethyelene and cadmium plate.....45

Fig. 15. Influence of the polyethylene bottom thickness on the neutron flux 46

Fig. 16. Influence of the polyethylene top thickness on the neutron flux 47

Fig. 17. Influence of the polyethelene box length on the neutron flux 48

Fig. 18. Influence of the cadmium plate thickness on the neutron flux 49

Fig. 19. Ionization (a, b) and fission chambers (c, d, e) layout in the preliminary RMS design 52

Fig. 20. Concept of the non-detection and false alarm probability with different measurement times: (a) measurement time – t_1, (b) measurement time – t_2, ($t_2 > t_1$) 57

Fig. 21. Diversion analysis results for the fission chamber unit. The yellow cell indicates removed SNF assembly and substituted with dummy assembly made of stainless steel. The blue cell indicates location of the fission chambers 59

Fig. 22. Diversion analysis results for the ionization chamber in the center position. The yellow cell indicates removed SNF assembly and substituted with dummy assembly made of stainless steel. The green cell indicates location of the ionization chamber 61

Fig. 23. Diversion analysis results for the ionization chamber in the edge position. The yellow cell indicates removed SNF assembly and substituted with dummy assembly made of stainless steel. The orange cell indicates location of the ionization chamber 63

Fig. 24. Final RMS design: (a) side view and (b) magnified side view 65

Fig. 25. RMS signal representation to the IAEA inspectors: (a) neutron case, and (b) gamma case 68

LIST OF TABLES

Page

Table 1. Significant quantities for different types of nuclear material 5

Table 2. Dimensions of the ACE 7 fuel assembly 14

Table 3. Dimensions for the MCNP model of the dry cask 17

Table 4. Concentration, half-lives, and prominent gamma energy of fission product isotopes with the highest gamma emission rate per one PWR SNF assembly 20

Table 5. Concentration, half-lives and spontaneous fission rates before and after cooling time for dominated actinides per one PWR SNF assembly 21

Table 6. Linear attenuation coefficients and densities for the dry cask shielding materials for 600 (keV) gamma energy 22

Table 7. Results for the gamma flux in the isotropic point source test 25

Table 8. Row test results for the gamma flux 30

Table 9. Row test results for the neutron flux 31

Table 10. Gamma energy distribution on the top of the MPC 32

Table 11. Results for the neutron flux in the open lid test 34

Table 12. Results for the gamma flux in the open lid test 34

Table 13. Results for the exposure rate in the open lid test 35

Table 14. Contribution of (n, γ) reactions to the total gamma flux based on the lattice test results 36

Table 15. Neutrons energy group structure used for calculation of the fission chamber response 40

Table 16. Response function values for the different gamma energies in air 41

Table 17. Results for simulations with combined geometry included cadmium plate and varying bottom polyethylene box thickness: closed and open lid cases 50

Table 18. Optimal dimensions for the polyethylene box and cadmium plate.....51

Table 19. Summary of diversion scenarios.....54

Table 20. Cost estimation of the RMS components.....71

1. INTRODUCTION

1.1 Background

1.1.1 Spent Nuclear Fuel Inventory and Storage Options

The worldwide demand for electric power generation is constantly increasing. Thereby the popularity of clean and efficient sources of electricity generation, like nuclear power, is rising fast in both the developing and industrialized countries. Both consider nuclear power as a main component of their energy strategies that will allow to secure their future demands of electricity and to preserve their finite natural resources. It is clear that increasing the number of nuclear power plants (NPP) will inevitably lead to the increase of spent nuclear fuel (SNF) inventory, the management and disposal of which has always been politically difficult and a technically challenging issue. After the SNF is discharged from the reactor, it is placed in storage pools at the NPP site for cooling. These pools have limited capacity and usually are designed to accommodate about 10 to 20 years of discharged SNF from the core. Therefore, after 3-5 years of cooling time, it is desirable to move the SNF to either a: (1) dry storage facility, (2) spent fuel reprocessing plant, or (3) geological repository [1]. Limited availability of SNF reprocessing plants and delay in construction of geological repositories led to the accumulation of SNF in both wet and dry storages. Also more and more countries accept "*wait and see*" policy, which means "first storing the fuel and deciding on disposal or reprocessing later" [2]. According to the International Atomic Energy Agency (IAEA), current SNF inventory approximately amounts to 290,000 tHM, 1/3 of which has been reprocessed. The IAEA forecast is 445,000 tHM by 2020, only 25% of which might be reprocessed. The rest of SNF will have to be stored [2].

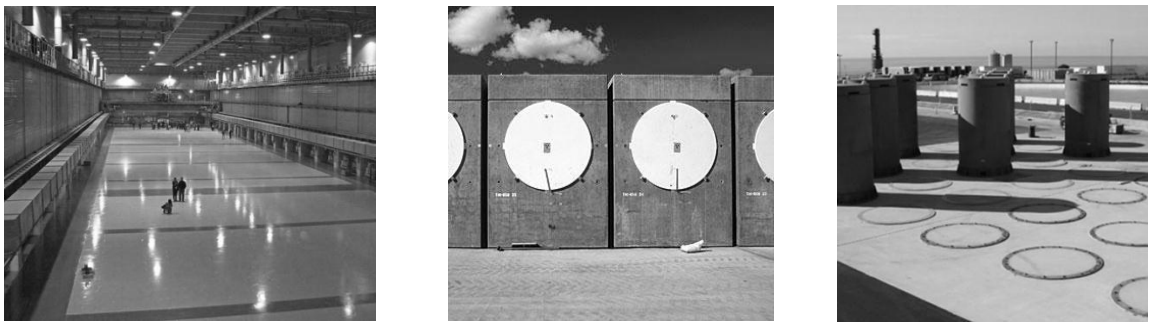

(a) (b) (c)

Fig. 1. Three types of SNF dry storage facilities: (a) vault, (b) silo and (c) cask

Dry storage facilities today are the most utilized SNF storage option. There are three types of these: (1) vaults, (2) silos and (3) casks. Vault is a large concrete building that has cavities for SNF, which is stored in sealed metal cylinders (Fig. 1, (a)). In a silo storage system, the fuel is stored in concrete cylinders, usually in vertical position (Fig. 1, (b)). Dry casks storage is a large number of metal-concrete casks placed on a flat concrete pad and usually located outside, near or away from the reactor (Fig. 1 (c)). Dry cask type storage has been widely used for the past 10 years. It gained popularity because of several convenient design features. It can be used for both storage and transportation. Its modular structure provides convenient flexibility if there are any changes in storing procedures with time, such as expansion, shrinkage or relocation of facility. Additional casks can be easily added to the existing facility as well as can be divided into several small sites if necessary [1] [2].

Typical dry cask consists of inner metal canister (multi-purpose canister or MPC) and outer concrete canister. It uses air as a coolant and metal and concrete as radiation shielding. The MPC is sealed by filling the gaps inside with an inert gas to prevent corrosion of SNF and structural materials. An MPC, depending on the dry cask design provided by different vendors, can store up to 40 pressurized water reactor (PWR) SNF assemblies. The MPC has metal grid inside that holds all fuel assemblies together (Fig. 2, (a)). After the SNF is loaded, metal canister is filled with inert gas and

welded. It is then placed inside the concrete canister and covered with a massive metal-concrete lid (Fig. 2, (b)). The space between the MPC and the outside concrete canister has air inlets for ventilation (passive cooling) and water drainage.

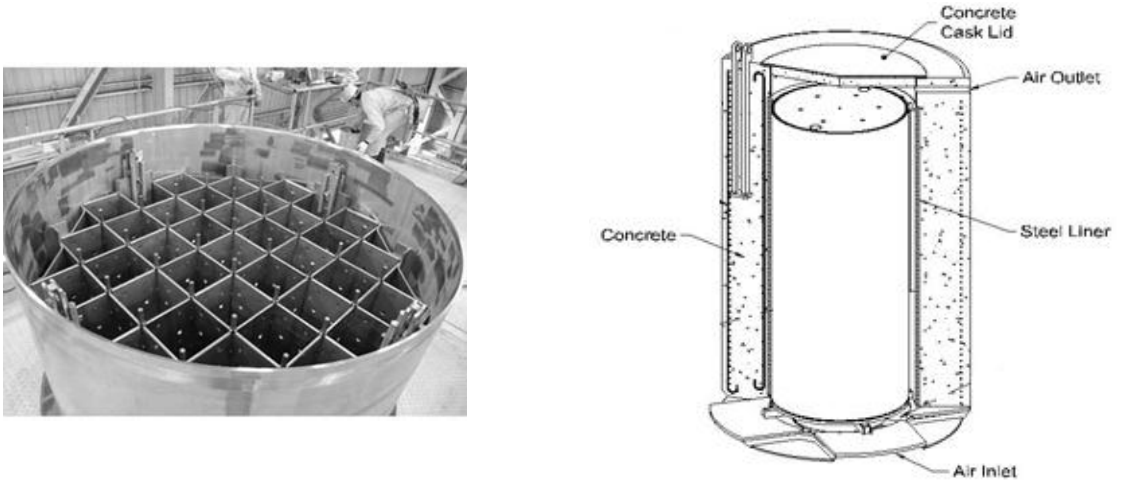

(a) (b)

Fig. 2. Two main components of the dry cask: (a) inner metal liner with grid inside and (b) outer concrete canister with lid

The United States Nuclear Regulatory Commission (NRC) recognized dry cask storage option as "safe and environmentally acceptable for a period of 100 years" [1]. Different research projects are currently underway to prove this statement, but so far nuclear community has had mostly positive experience with this type of SNF dry cask storages [3]. Another significant advantage is the cost. Interim dry storage is significantly cheaper than the reprocessing or direct disposal. However, there are also some problems associated with SNF stored in dry cask:

(1) First is fairly high radiation level around casks. The definition of this radiation level may vary from country to country, because of different regulations and norms, and also from one cask design to another[1];

(2) Second problem is growing number of such storages, which will require additional efforts from operators and IAEA inspectors to provide security and reliable safeguards measures.

1.1.2 Dry Cask Storage and IAEA's Concerns

The SNF should be subjected to the IAEA safeguards[2] as it is irradiated *"direct use material"*[3]. In addition to unused uranium, SNF contains large amounts of fission products and actinides. The actinide of concern is plutonium, which when extracted from the SNF, can be used for manufacturing of a nuclear explosive device. Significant amounts of plutonium are expected to be contained in each dry cask. For example, a single dry cask with a capacity of 32 PWR SNF assemblies could potentially contain up to 20 "*significant quantities*" (SQ). A significant quantity is defined by the IAEA as "the approximate amount of the nuclear material for which possibility of manufacturing a nuclear explosive device cannot be excluded" [4]. The SQ values currently in use are listed in Table 1.

---

[1] For instance, at Comanche Peak NPP dry cask storage facility, dose rate at contact and middle cask height is 75 (mrem·h^{-1}) and 1 (m) away is 36 (mrem·h^{-1}) [35]. U.S. NRC limits for annual dose for normal operation beyond the controlled area of the independent storage of SNF is 25 (mrem) [34]. Thus inspector who is working on the site and checking on seals will get annual dose within 1 hour of work.

[2] *Objective of IAEA safeguards* - the timely detection of the diversion of significant quantities of nuclear material from peaceful nuclear activities to the manufacture of nuclear weapons or of other nuclear explosive devices or for purposes unknown, and deterrence of such diversion by the risk of early detection [4].

[3] *Direct use material* - nuclear material that can be used for the manufacture of nuclear explosive devices without transmutation or further enrichment. It includes plutonium containing less than 80% Pu-238, high enriched uranium and U-233. Chemical compounds, mixtures of direct use materials (e.g. mixed oxide (MOX)), and plutonium in spent reactor fuel fall into this category. *Unirradiated direct use material* is direct use material which does not contain substantial amounts of fission products; it would require less time and effort to be converted to components of nuclear explosive devices than irradiated direct use material (e.g. plutonium in spent reactor fuel) that contains substantial amounts of fission products [4].

Table 1. Significant quantities for different types of nuclear material

Material	SQ
Direct use nuclear material:	
Plutonium containing less than 80% of Pu-238	8 kg
Uranium-233	8 kg
Highly enriched uranium (containing more than 20% of U-235)	25 kg of U-235
Indirect used nuclear material:	
Uranium containing less than 20% of U-235	75 kg of U-235 (or 10 t natural U, or 20 t depleted U)
Thorium	20 t

The IAEA's goal is to be able to maintain the continuity of knowledge (CoK) about the nuclear material (NM) inside the dry casks, as well as be able to verify it, during the entire storage period. Unfortunately, dry cask design has some disadvantages that do not facilitate effective verification process: (1) fairly high radiation levels for inspectors and (2) inaccessibility of the SNF. Fuel, placed in the dry cask, is no longer accessible to be verified by simple counting or attribute tests[4]. However, there is also one advantage – no movement of nuclear material at the site - that simplifies the safeguards routine significantly. Once the dry cask is shipped to the storage, it is not supposed to leave its place until there is a decision to move it to the reprocessing plant or to the geological repository. It means there are not a lot of activities that should be monitored or verified by the IAEA inspectors. Also inaccessibility of the SNF implies its inherent security.

Although the IAEA is currently putting dry cask storage facilities under safeguards, it is still lacking effective safeguards tools that can be used for verification of dry cask content. Based on the literature survey on the safeguards methods employed at the SNF

[4] *Attributes test* - a statistical test of a characteristic (or attribute) of an item to which the response is either 'yes' or 'no'. For example, seal verification is an attributes test: the seal is inspected and the result should be either that it shows evidence of tampering or it does not. Verification of items by non-destructive assay for radiation emission is also an attributes test: a tested item either emits radiation within a specified range or it does not. A 'no' answer identifies a defect [4].

dry cask storage facilities [5] [6] [7], it was found that current SNF safeguarding methods rely heavily upon containment/surveillance (C&S) measures with regular inspections to ensure that tamper indicating devices (seals) are still intact. The C&S measures include installation of seals and surveillance cameras. There are usually two seals placed inside and outside of the dry cask. There were several projects to develop and implement neutron/gamma radiation "*fingerprinting method*" [8] [9]. This method is supposed to be used for re-verification of the dry cask content and it is described in more details in section 1.2.

The increasing number of dry cask storage facilities will increase the likelihood of C&S failure and loss of CoK, as all dry casks are usually stored outside and exposed to different weather conditions. One of the potential problems is that if the external seal is broken there is no other way to verify dry cask content but by opening the concrete canister and checking on the internal seal. This is a very undesirable and expensive undertaking. Hence, alternate methods need to be developed for safeguarding SNF in addition to those mentioned above.

1.1.3 Why Remote Monitoring System for Dry Cask Storage?

Remote Monitoring System (RMS) is important component of Information-Driven Safeguards (IDS)[5] [10]. These are safeguards whose planning, conduct and evaluation are based on an ongoing analysis of all safeguards-relevant information available to the IAEA about a State. It helps optimizing IAEA's efforts and reducing the number of on-site inspections to the extent feasible. For instance, under the integrated safeguards (IS)[6], if "the IAEA has drawn a conclusion of the absence of undeclared nuclear material and activities in the State" [4], then the inspection frequency for SNF verification may be reduced from the present 3 month to a 12 month interval [11].

[5] More information about IDS can be found on IAEA web-site: <www: iaea.org>. The IDS concept was extensively discussed during Symposium on International Safeguards in 2010.

[6] "*Integrated Safeguards* (IS) is a specific case of IDS whereby the IAEA has drawn and maintained a "broader conclusion" regarding the completeness and correctness of a State's peaceful nuclear programme." [11]

The forerunner of the RMS was Unattended Monitoring Systems (UMS). It is important to distinguish these two types of monitoring systems. The UMS collects safeguards relevant data through non-destructive assay (NDA) instruments and C&S tools (seals, cameras) and stores it on the computer server installed at the site. At the time of scheduled inspection, inspector may review recorded information to clarify, if any, inconsistencies or mistakes in operator's reports and declarations. Today the use of unattended safeguards instruments is still a significant part of the IAEA safeguards. Surveillance cameras monitor relevant nuclear activities at the site; unattended NDA sensors are used to monitor reactor core refueling or any other flow of NM at various facilities. The transmission of the safeguards data off-site via communication networks to the IAEA Headquarters or another IAEA location makes UMS a remote system, or RMS [12]. The principal of the RMS operation is shown on Fig. 3: as unattended system, it first collects safeguards data from the NDA instruments and C&S tools, temporarily store them on the local server and then transmit this data via satellite or phone link to the IAEA Headquarters or Field Office. The RMS saves time and resources for both the IAEA and an operator. Such systems allow automating some inspection activities and reducing the presence of the IAEA inspectors at the site. The system runs 24 hours per day, 365 days per year and continuously collects and transmits safeguards data. In other words, such systems transfer some of the routine inspection work to the IAEA Headquarters thereby saving inspector's time on travelling, optimizing time and number of inspections and making a better use of the time when inspectors are in the field. The RMS also can enhance effectiveness of safeguards approach by providing real time indication of the anomalies and violations, which in turn, increases deterrence value of safeguards. For example, decision about inspection can be made if there is a suspicious change in the signal and inspectors will come to the site already prepared and ready to ask operator certain questions.

The RMSs are especially useful at the facilities with high radiation levels and in places where the direct access to NM is very difficult. Dry cask storage falls into this category of facilities [13] [11].

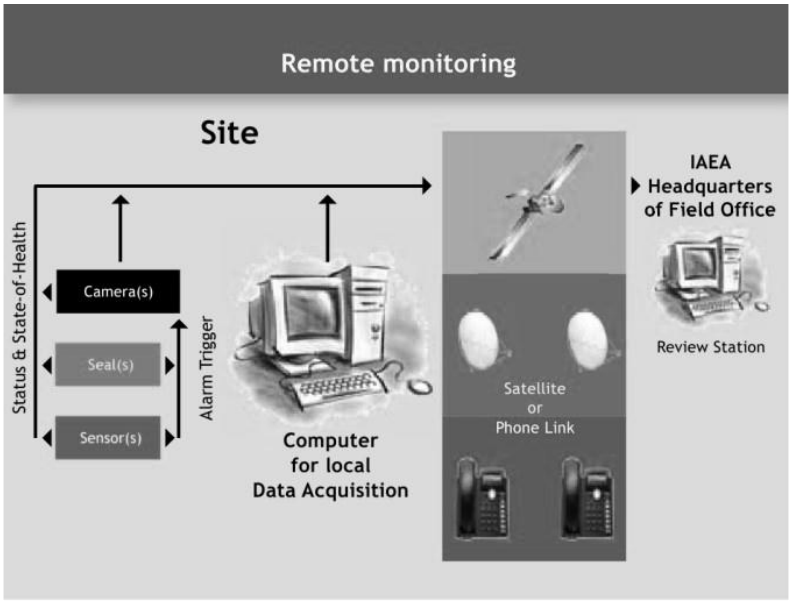

Fig. 3. Principal of operation of the remote monitoring system

To summarize, RMS could be a good safeguards tool for dry cask storage and, vice versa, dry cask storage facility is a good candidate for deployment of RMS because:

(1) Dry cask storage is a static facility. There is no movement of SNF or manipulations with SNF at the site. The RMS, installed at the time of SNF loading, stays there and provides continuous information to inspectors;

(2) Dry cask storage is an item facility[7]. It allows easy yes/no monitoring process.

(3) Dry cask is high radiation level facility. It does not allow for extended presence of inspectors at the site;

Dry cask storage is among the first facilities on the list for an extension of timeliness goal under Integrated Safeguards Approach: from 3 months to 12 months interval.

[7] *Item facility* - a facility where all nuclear material is kept in item form and the integrity of the item remains unaltered during its residence at the facility. In such cases, IAEA safeguards are based on item accountancy procedures (e.g. item counting and identification, non-destructive measurements of nuclear material and the verification of the continued integrity of the items). Examples of item facilities are most reactors and critical assemblies (critical facilities), and storage installations for reactor fuel [4].

Deployment of RMS may extend timeliness goal even more and transform classic on-site inspections to remote safeguards inspections [11].

1.2 Previous Work

Researchers at the Lawrence Livermore National Laboratory (LLNL) conducted studies to analyze the feasibility of the "*fingerprinting method*" [14]. The measurement campaign was performed at the Idaho National Laboratory at the Test Area North. They examined the radiation signals (both neutron and gamma) from six different types of SNF dry storage casks using thermal neutron and gamma-ray imaging systems. This type of NDA instruments uses the coded-aperture technique. To get a good quality image, the instrument requires certain installation procedures and a few hours measurements. The corrections to results should be made if wind changes the aperture position during the measurement. Also, it is important not to detect signal from the neighboring casks. The results of their research proved that the radiation pattern emitted by SNF inside the cask is dependent on the type of dry cask and can be used for producing images ("*fingerprints*"). However, certain complications were discovered with both gamma and thermal neutron signals:

(1) Gamma radiation unscattered component, which originates directly from the nuclide decay and does not undergo scattering before it reaches the detector, caries information about its actual point of origin inside the cask and therefore is useful for imaging (fingerprinting) of cask content. This component was easily detectable by germanium spectrometer, but was not visible for gamma imager used in the experiment. Instead, the scattered component, which originates directly from the nuclide decay and does undergo scattering before reaches the detector, was dominant in the obtained gamma images. It washed out all the details, because due to scattering these gammas did not carry information about its point of origin anymore. This observation led to a conclusion that a better gamma imager, sensitive to higher energies unscattered gammas and

with larger detector surface area, should be developed to produce images with sufficient details and within hour timescales.

(2) Neutron radiation signal has also two components: scattered (thermal neutrons) and unscattered (fast neutrons). Similar to the case of gammas, unscattered (fast) neutrons carry information about their origin inside the cask, while thermal neutrons, due to multiple scattering in cask concrete walls, can only create fuzzy images with no details about dry cask content, like distinction between SNF assemblies. During the experiment, it was proved that fast neutrons could leave the cask without scattering. But there is no currently existing fast neutron-imaging instrument; one is being developed by Brookhaven National Laboratory [14].

As a result of this study, LLNL researchers concluded that "further development and enhancement of non-destructive techniques and equipment are required in order to get better signal processing" and images ("*fingerprints*") with sufficient details about dry cask content. There is also one more limitation of the fingerprinting method that was not considered in this study. As mentioned above, emitted radiation pattern depends on the dry cask design. But this relation can be lost. It was found that some states might apply additional shielding around the dry casks to comply with their local regulations. For example, Taiwan Power Company put additional 30 (cm) thick concrete at the top and 35 (cm) concrete around the side of each storage cask to the original design of Universal Multi-Purpose System provided by NAC International Inc. [13]. Such design modifications may significantly influence both gamma and neutron signals. Another challenge may arise if dry cask design uses boron-bearing materials that absorb neutrons and may block thermal neutron signal. It is also important to note the cost of such imaging system. In the LLNL study, gamma imager cost was estimated about $1,000,000. The system includes germanium detector that requires cooling with liquid nitrogen, electronics, shielding materials and different coded-apertures.

Assessment of the fingerprinting method for CANDU[8] reactor SNF was conducted at the Nuclear Security Science and Policy Institute, Texas A&M University [15], which also determined that better re-verification methods are required to improve the non-detection probability. Another attempt was made on the development of a Compton Dry-Cask Imaging System by the Idaho National Laboratory [16], but publicly available information does not address the issue of various SNF diversion scenarios and does not elaborate on technical characteristics of the detection system.

From the survey of previous research work in this area, it can be concluded that there is not enough work performed on the investigation of neutron/gamma signals change for different SNF diversion scenarios, including opening of the dry cask and removal of SNF assemblies. There were also no references found about RMS option for dry cask storage facilities that could be designed and used for SNF safeguarding, which justified the reason for this thesis work.

1.3 Objective and Motivations

The objective of this thesis was to develop a conceptual design of a neutron and/or gamma based RMS that allows maintaining the CoK on SNF in dry cask storage and detection of possible diversion of SNF assemblies for various hypothetical diversion cases.

The growing amount of SNF and the wide use of dry cask storage facilities was the first motivation for this thesis work. The second one was the verification challenge associated with this type of dry storage.

This study used a computational approach. The thesis does not cover electronics and equipment required for the encryption and remote transmission of the signal from the RMS to the IAEA. It also does not include development of the uninterrupted power source.

[8] CANDU states for CANada Deuterium Uranium reactor

1.4 Thesis Overview

This thesis focused on the development of a neutron and/or gamma based RMS design and studied the feasibility of its deployment inside a PWR SNF dry cask. The goal of the study is to design such a system concept in a way that it would allow maintaining the CoK on the dry cask content and detecting the diversion under different scenarios.

Section 2 of this thesis elaborates on the development of the dry cask computer model created using MCNP transport code, including evaluation of the radiation source-term for one PWR SNF assembly conducted with ORIGEN-ARP. This section also includes procedure and results of the analytical calculations performed for MCNP dry cask model validation.

Section 3 describes the development of the conceptual RMS design. It includes the series of tests (purpose and setup) that were created to investigate neutron and gamma flux behavior inside and outside the dry cask; and review of the other factors used for derivation of general design requirements. The section is concluded with choice of the RMS components and review of the preliminary RMS design.

Section 4 presents the results of the diversion analysis with the preliminary RMS design, including calculation of non-detection probabilities for every diversion scenario. The diversion analysis outcome was used to arrive at the final design

Section 5 consists of concluding discussions of the RMS data representation to the IAEA, RMS lifetime and cost estimate of the RMS final design.

2. DEVELOPMENT OF THE DRY CASK COMPUTER MODEL

2.1 Procedure

The first step of this study was creation of a computer model of the dry cask with SNF assemblies inside. This model was used for simulation of the realistic radiation environment and SNF radiation signatures required to choose RMS components and evaluate its performance. The following tasks were completed to create computer model of the dry cask:

(1) Modeling of a generic dry cask with PWR SNF assemblies inside using the radiation transport code, MCNP;

(2) Estimation of the gamma and neutron radiation source terms for PWR reactor SNF assembly with typical initial enrichment and fuel burn-up;

(3) Validation of the MCNP model through analytical calculations.

2.2 MCNP Modeling

Today, computer simulations present a cost- and time-efficient opportunity to investigate the behavior of complex systems, like the one used in this study. Also use of computer codes allow testing different system designs, estimate their performance in the virtual world first and only after that, using simulation results, create a successful prototype of the system for testing in the field. One of the computer codes widely used today is MCNP, developed by Los Alamos National Laboratory. MCNP is a general-purpose Monte Carlo N-Particle code that can be used for neutron, photon, and electron or coupled neutron/photon/electron transport. The code also allows development of complex three-dimensional combinatorial geometry [17]. MCNP was utilized to create a dry cask computer model. The dry cask model was developed in two steps: (1) model of PWR assembly was designed and (2) dry cask was created and filled with the same 32 PWR assemblies. The following sections provide more detailed descriptions of the dry cask model development, dimensions and materials used.

2.2.1 MCNP Model of a PWR Fuel Assembly

The PWR under study is one of the types of light water reactors (LWR) that uses light water as primary and secondary coolant and as neutron moderator. The PWR fuel is usually made out of low enriched uranium in the form of uranium dioxide (UO_2). Uranium dioxide fuel pellets are placed inside Zircaloy tubes, which are then assembled together in 15×15 or 17×17 fuel rod arrays. There is no unified fuel assembly design for all types of PWR. The number of fuel rods, rods with burnable poison and control rods depends on reactor features and customer's needs. This study used PWR fuel assembly, ACE7, developed by Korean Nuclear Fuel Company. The technical specifications of the ACE7 PWR fuel assembly used to develop MCNP model were collected from Nuclear Engineering International Magazine [18]. This fuel assembly design uses a 17×17 fuel rod array with 25 unfueled positions that are either filled with water or boron absorber rods. Overall assembly length is 406.3 (cm) of which 388.1 (cm) is active fuel length and the rest is structural support material such as top and bottom nozzles, springs, fission gas plenums and filters. Each fuel rod contains about 394 fuel pellets in a Zircaloy tube with a wall thickness of 0.0572 (cm). Fuel pellets are 0.983 (cm) long and 0.8192 (cm) in diameter. They are stacked inside the rod and the gaps between them and cladding material is filled with helium gas to improve the conduction of heat from the fuel to the cladding. Other dimensions used in the model are presented in Table 2.

Table 2. Dimensions of the ACE 7 fuel assembly

Dimension	Value, (cm)
Pellet outside diameter	0.8192
Pellet length	0.983
Rod outside diameter	0.95
Rod inner diameter	0.8356
Clad thickness	0.0572
Rod length	388.1
Plenum length	9.1
Overall assembly length	406.3
Overall assembly width	21.4

For this study, the helium gap between fuel and cladding was not modeled. It was assumed that the fuel swelled after irradiation and the helium was displaced to the top and bottom of the fuel rod to the plenum region. Therefore the fuel density and materials composition were re-calculated to take into account those effects. To find a new density for the fuel after irradiation, the total fuel mass in one rod was divided by the rod volume that was occupied by the fresh fuel and helium gap together before irradiation. As a result the fuel density after swelling was found to be 9.97 ($g \cdot cm^{-3}$). For comparison, the density of the fresh uranium dioxide fuel is usually about 10.4 ($g \cdot cm^{-3}$). The plenum region after irradiation would contain displaced helium, Zircaloy and stainless steel. The volume fractions for these materials were estimated using information presented in [19] for the fuel region # 7. Those volume fractions were then multiplied by the volume of the plenum region and related densities to find materials weight fractions for usage in the MCNP input file. The final density of the homogenized mixture of helium, Zircaloy and stainless steel was found to be 2.46 ($g \cdot cm^{-3}$). Information about other materials used, their densities and compositions can be found in the MCNP input file in Appendix A or in "MCNP Material Primer" prepared by Pacific Northwest National Laboratory [20]. Also for simplicity, the structural assembly components, such as top and bottom nozzles, grid, etc., were not modeled. A picture of a typical PWR fuel assembly and drawing obtained using MCNP model through the visual editor software are shown in Fig. 4.

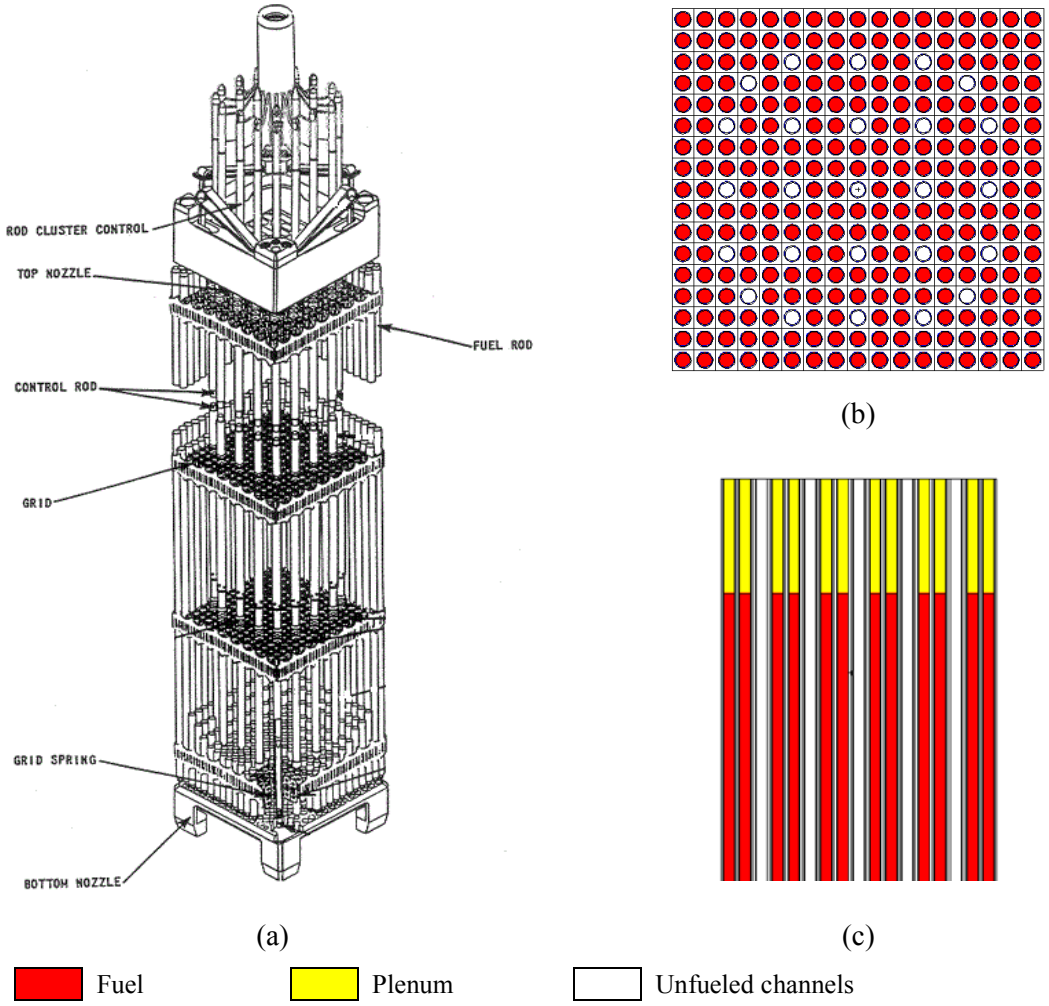

Fig. 4. Typical PWR fuel assembly (a) and its MCNP model used in this study: (b) top view, (c) axial view (truncated top part of the assembly)

2.2.2 MCNP Model of a Dry Cask

The dimensions and characteristics of the MCNP dry cask model were roughly based upon the dry cask design HI-STORM 100S Version B developed by HOLTEC Inc [21] [22]. This design can accommodate the MPC with a capacity of 32 PWR fuel assemblies. The MPC is made of stainless steel, and it has an inner grid with 32 cells for storing individual SNF assemblies. Each cell has liners made of Boral for additional neutron shielding. The outer concrete canister has three main layers: thin inner and outer

shells made of carbon steel and a thick concrete layer in-between. The dimensions used for the MCNP model are presented in Table 3, and the drawing of the model is shown in Fig. 5. Information about the materials used, their densities and compositions can be found in the MCNP input file in Appendix A.

As mentioned above, a dry cask storage site is usually a large number of casks placed on a flat concrete pad and located outside, near or away from the reactor. For this study, concrete pad and surrounding dry casks were not modeled; it was assumed that they do not affect neutron and gamma signal inside a single dry cask.

Table 3. Dimensions for the MCNP model of the dry cask

Dimensions for the multi-purpose canister (MPC)	Value, (cm)
Outer steel radius	84.4
Inner steel radius	83
Steel lid thickness	24
Grid thickness	0.72
Boral liner thickness	0.25
Cell dimension	23.03×23.03
Dimension for the outer concrete canister	**Value, (cm)**
Radial layers:	
Outer radius	165.1
Inner radius	91.9
Inner carbon steel shell thickness	2.5
Outer carbon steel shell thickness	0.7
Concrete thickness	69.8
Top layers:	
Concrete thickness	20
Stainless steel ring thickness	8
Stainless steel top thickness	2.5
Bottom layers:	
Stainless steel	26.5

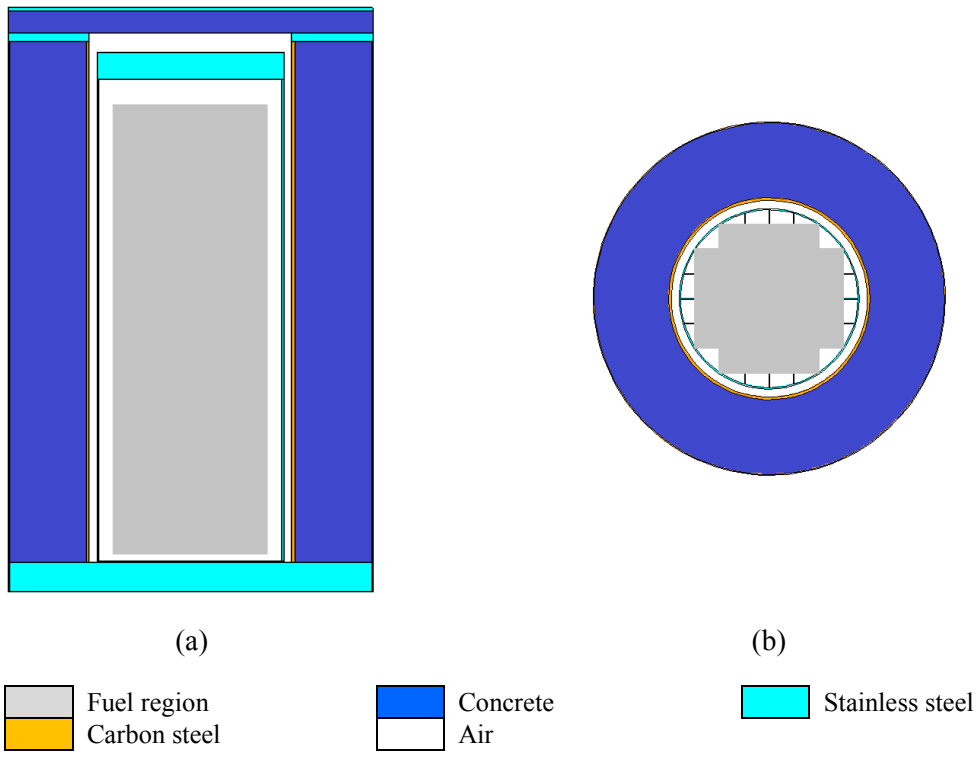

Fig. 5. MCNP model of the dry cask for PWR SNF assemblies: (a) axial view and (b) top view

2.3 Generation of the Radiation Source-Term for PWR Spent Fuel Assembly

To generate the radiation source-term, ORIGEN-ARP burn-up code was used [23]. ORIGEN-ARP was developed by Oak Ridge National Laboratory. It allows simulating fuel irradiation and radioactive decay during cooling, and then creating output files in terms of nuclide concentration, radioactivities and their neutron/gamma emission rates.

To produce radiation signature associated with SNF, it was necessary to simulate irradiation of fuel for 3 operational cycles as it stays in the reactor core. Typically each of those cycles lasts about 18-24 months. During this time, due to various nuclear reactions, fuel accumulates significant amount of fission products and actinides that absorbs neutrons. At this time fuel should be removed from the core and placed into a storage pool. After discharge, SNF becomes a source of high energy neutrons due to

spontaneous fission of actinides (e.g. Pu-240, Cm-244, Am-243) and (α, n) reactions on light elements; and of intense gamma radiation due to decay of fission products (e.g. Cs-137, Eu-154), and activation of the cladding material (e.g. Zr-95, Co-60). In the wet storage, SNF is usually cooled for 3-5 years before it can be moved into a dry storage facility.

For the purpose of this study, it was assumed that all 32 SNF assemblies have the same (1) initial enrichment – 3.9%, (2) burn-up – 45,000 MWd/Mt, and (3) cooling time – 3 years. The gamma source strength was estimated using 18 energy groups and neutron source strength using 44 energy groups. The gamma and neutron energy groups and respective source strength are given in Appendix B.

The gamma spectrum has the highest emission rate in the middle energy groups, low (0.001-0.03 (MeV)) and high energy (above 2 (MeV)) gammas provide less contribution to the total emission rate. As shown on graph in Fig. 6, gamma intensity peak is located around 0.6-0.7 (MeV). This is due to high and virtually constant concentration of fission products like Cs-137. Some other dominant gamma-emitting isotopes and their characteristics are shown in Table 4.

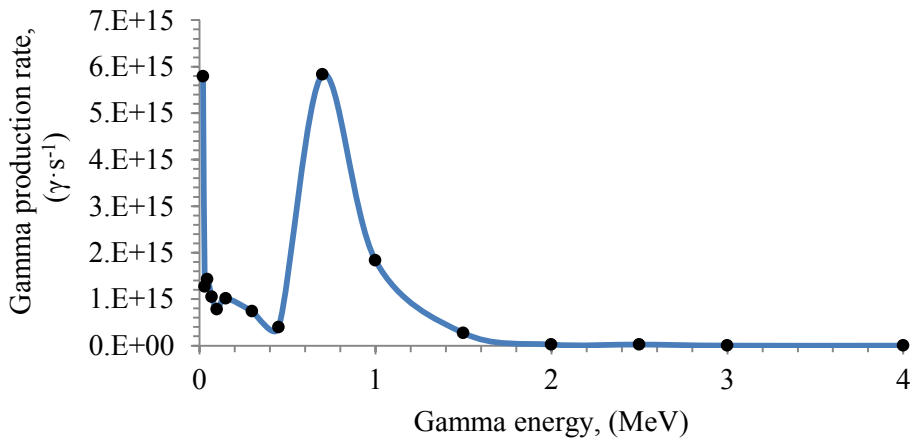

Fig. 6. Gamma spectrum for the PWR SNF assembly with discharge burn-up 45 GWd/Mt burned at specific power 37.5 MW/t and cooled for 3 years

Table 4. Concentration, half-lives, and prominent gamma energy of fission product isotopes with the highest gamma emission rate per one PWR SNF assembly

Isotope	Half-live, (years)	Gamma energy, (keV)	Intensity, (%)	Concentration after discharge, (g)	Concentration after 3 years of cooling time, (g)
Zr-95	0.17	724.2	43.1	7.49E+01	5.32E-04
		756.7	54.6		
Cs-134	2.06	604.7	97.6	1.06E+02	3.86E+02
		795.8	85.4		
Cs-137	30.17	661.6	85.1	8.45E+02	7.88E+02
Eu-154	8.5	1274.4	35.5	1.86E+01	1.46E+01

The neutron spectrum has two maximums in the region of high energies at about 1 (MeV) and 4.8 (MeV) as shown on graph in Fig. 7. The first peak is due to spontaneous fission of actinides and other transuranic elements. As it can be seen from Table 5, Cm-244 has the highest spontaneous fission rate and dominates SNF neutron source-term over long period of time. After Cm-244 decays, plutonium isotopes, Pu-240 and Pu-242, will provide stable neutron signal from SNF. The second peak around 4.8 (MeV) is due to neutrons from (α, n) reactions with oxygen present in fuel. The average neutron energy from such reaction with O-18 is 4.2 (MeV) and with O-17 is 5.5 (MeV).

Neutron and gamma source strengths for 1 SNF assembly were 4.23E+08 $(n \cdot s^{-1})$ and 2.04E+16 $(\gamma \cdot s^{-1})$ respectively. These values were multiplied by the number of fuel assemblies inside the dry cask. As a result, for 32 assemblies the total neutron source strength was 1.35E+10 $(n \cdot s^{-1})$, and the total gamma source strength was 6.54E+17 $(\gamma \cdot s^{-1})$. These source strength values were incorporated into the MCNP dry cask model for the radiation transport simulations described in the following sections.

At this point, it is also important to mention plutonium content in a single PWR assembly; it is about 5.51 (kg). Thus, single dry cask with 32 PWR SNF assemblies contains about 176.3 (kg) of plutonium which equals to about 22 SQ (see Table 1).

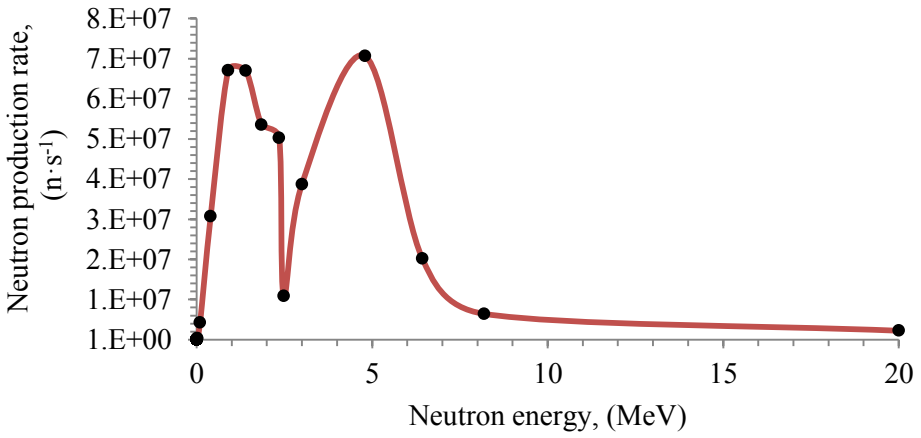

Fig. 7. Neutron spectrum for the PWR SNF assembly with discharge burn-up 45 GWd/Mt burned at specific power 37.5 MW/t and cooled for 3 years

Table 5. Concentration, half-lives and spontaneous fission rates before and after cooling time for dominated actinides per one PWR SNF assembly

Isotope	Half-life, (years)	Concentration after discharge, (g)	Concentration after 3 years of cooling time, (g)	Spontaneous fission neutron emission rate after 3 years of cooling time, ($n \cdot s^{-1}$)
U-235	7.00E+08	3.72E+03	3.72E+03	3.88E-02
U-238	4.40E+09	4.58E+05	4.58E+05	6.24E+03
Pu-238	8.77E+01	1.24E+02	1.24E+02	3.39E+05
Pu-239	2.40E+05	2.86E+03	2.95E+03	4.40E+01
Pu-241	1.43E+01	9.34E+02	8.08E+02	1.67E+00
Pu-240	6.56E+03	1.18E+03	1.18E+03	1.23E+06
Pu-242	3.73E+05	4.17E+02	4.17E+02	7.27E+05
Cm-244	1.81E+01	4.15E+01	4.15E+01	4.11E+08

2.4 Analytical Calculations for the MCNP Model Validation

Once the MCNP dry cask model was created and characterized with appropriate radiation source-term, it was validated with analytical calculations. Here validation process included a sample problem, which outcome was determined with analytical

calculations and also simulated with the MCNP dry cask model. Since this study did not include any field experiments, analytically calculated values were assumed to be accurate enough to represent real experiment results. In turn, the MCNP dry cask model was expected to be capable of replication of those results. For simplicity, calculations were done only for the single gamma energy of 600 (keV). This energy was chosen intentionally for two reasons: (1) to avoid interpolation for the linear attenuation coefficients, and (2) because this energy dominates in the radiation source-term as was shown before (see Fig. 5). The gamma source strength was chosen as 1E+06 (Ci) (or 3.70E+16 ($\gamma \cdot s^{-1}$)), which is comparable with the source strength for one SNF assembly. Linear attenuation coefficients for the dry cask shielding materials were calculated using "X-COM: Photon Cross Sections Database" developed by NIST [24], and they are presented in Table 6. Thicknesses of the shielding layers can be found in Table 3.

Table 6. Linear attenuation coefficients and densities for the dry cask shielding materials for 600 (keV) gamma energy

Material type	Material density, ρ, ($g \cdot cm^{-3}$)	Linear attenuation coefficient for 600 (keV), μ, (cm^{-1})
Stainless steel	7.92	6.10E-01
Carbon steel	7.82	6.03E-01
Concrete	2.55	2.07E-01
Air	0.001205	9.71E-05

The *isotropic point source test* was developed to validate the "*geometry splitting*" feature used in the MCNP dry cask model for the importance sampling variance reduction method. Geometry splitting with importance sampling is a variance reduction technique available in the MCNP code. The MCNP5 Manual (Volume I) provides a detailed description of this feature [25]. Briefly, the thick geometry layers are divided into multiple layers with thickness usually equal to 1 mean free path for the dominant

gamma energy. Every layer is assigned an importance, the further the layer from the source the higher the importance. So when particles get transported towards the direction of interest, their population increases to provide better statistical convergence and hence lower variance. An appropriate particle weighting scheme is used by the MCNP code for not altering the answer when importance sampling and population adjustments are made. The particles getting transported in other direction undergo Russian roulette (which is the reverse of the importance survival sampling) to avoid wasting of computational time.

For this test, an isotropic point source was placed in the center of an empty dry cask (with no SNF assemblies inside). Flux estimation was performed outside of the dry cask on the top, bottom and lateral radial (side) positions as shown in Fig. 8. Distance from the dry cask outside wall to the detector was 30 (cm). For analytical calculations, the formula for the isotropic point source case with several layers of slab shield was used [26]:

$$\phi = \frac{S}{4\pi R^2} \cdot e^{-\sum_{i=1}^{I} \mu_i \cdot t_i}, \quad (1)$$

where

ϕ - uncollided gamma flux, ($\gamma \cdot s^{-1} \cdot cm^{-2}$)

S – isotropic point source strength, ($\gamma \cdot s^{-1}$)

R – distance to the detector, (cm)

t – shielding layers thickness, (cm)

μ – total linear attenuation coefficient of shielding layers, (cm^{-1})

I – total number of shield layers.

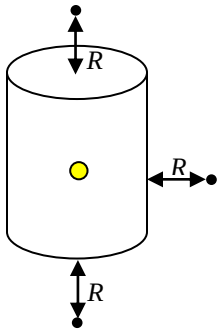

Fig. 8. Detector positions for the isotropic point source test

For MCNP simulation, a point detector (or F5 tally scoring)[9] and cell flux estimator (or F4 tally)[10] were used for uncollided gamma flux estimations. The F5 tally was used because this tally score provides output that gives results separately for two flux components: collided and uncollided. However, during the simulations, the use of F4 tally was found to be more accurate in comparison to F5 tally to estimate flux on the top of the dry cask as can be seen from the results shown below. To get the uncollided flux estimate using F4 tally, a small cell with radius of 1 (cm) and a transport cutoff energy of 599.99 (keV) were used.

The results of this point source test are presented in Table 7. From Table 7, it can be noticed that the results for F5 tally from the MCNP simulations at the side and bottom detector positions agree very well with the analytical calculations. The small disagreement between results may be attributed to the differences in linear attenuation coefficients libraries used in MCNP in comparison to those used in the analytical calculations. The F5 tally results for top detector position significantly overestimated analytically calculated value[11]. This was explained by F5 tally nature and the way

[9] *F5 tally* is the point detector next-event estimator. "It is the deterministic estimate (from the current event point) of a flux at a point in the space. Contributions to the point detector tally are made at source and collision events throughout the random walk." [25] For more information about F5 tally see [25].

[10] *F4 tally* is the track length estimate of a cell flux. It estimates flux by summing track length for all the particles and dividing it by the cell volume. For more information about F4 tally see [25].

[11] Debug simulations showed that F5 tally could replicate analytically calculated value for the top detector position, but only if radial cask layers were removed. With addition of the radial layers, F5 tally results were increasing with every other layer.

it estimates probabilities for particles that may contribute to the uncollided flux. For more information on F5 tally see [25].

Table 7. Results for the gamma flux in the isotropic point source test

Detector position	Analytical value, ($\gamma \cdot s^{-1} \cdot cm^{-2}$)	F5 MCNP value, ($\gamma \cdot s^{-1} \cdot cm^{-2}$)*	F5 tally percentage error, (%)	F4 MCNP value, ($\gamma \cdot s^{-1} \cdot cm^{-2}$)*	F4 tally percentage error, (%)
Side	2.51E+03	2.59E+03	2.97	2.82E+03	12.08
Bottom	1.66E+03	1.74E+03	4.21	2.16E+03	30.18
Top[8]	4.25E+01	2.53E+02	83.24	5.39E+01	26.9

**MCNP values have relative error of 4 to 5%*

Results for the F4 tally from MCNP simulations also agree reasonably well with the analytical calculations. The differences may be explained by the usage of cutoff energy card value of 599.99 (keV). MCNP does not allow use of source particles energy as cutoff energy for F4 tally. Thus, gammas that scattered on small angles and lost less than 1.11 (keV) of their energy could contribute to the total flux. The F4 tally measurement was also performed for all the detector positions to verify agreement between results. The difference between results increases with decreasing shielding thickness and is found to be consistent. It is higher at the bottom, where total shielding is thinner than at the side and the top, thus more scattered gammas could reach the detector.

Based on the isotropic point source test, it was concluded that geometry splitting along with the importance sampling methods used in the MCNP dry cask model worked well for the dry cask shielding layers to yield realistic results for the gamma flux compared to the analytical calculations.

3. CONCEPTUAL DESIGN DEVELOPMENT OF THE REMOTE MONITORING SYSTEM

3.1 Procedure

Designing of the RMS was a complex process consisting of several distinct steps. The following tasks were completed to arrive to the preliminary RMS design:

(1) Derivation of the design requirements through:
   - Reviewing of the IAEA requirements to the new safeguards systems;
   - Considering of the inherent dry cask limitations;
   - Investigating of the gamma and neutron flux behavior inside/outside the dry cask.

(2) Development of the preliminary RMS design based on the information from step (1) including:
   - Investigation of the concept feasibility;
   - Development of the schematic system design;
   - Selection of the detectors and materials that can be used, and
   - Optimization of the RMS components dimensions.

Based on the previous work overview in section 1.2, it was decided that RMS should be placed inside the dry cask. The LLNL study [14] showed that measurements outside the dry cask have certain disadvantages mainly due to heavy shielding of the radiation signal coming from the SNF. Also outside location will require additional system protection to avoid technical failures caused by different weather conditions. If the system placed inside the dry cask, then it will be protected from the environment and, what is more important, it will have potential to detect signal from all the SNF assemblies due to less shielding materials in between the system and SNF.

3.2 Derivation of Design Requirements

3.2.1 Inherent Dry Cask Limitations and IAEA Requirements

Dry cask dimensions put certain constraints on the system size. In the dry cask model under study, the air gap between MPC and concrete lids is 18 (cm). Once the RMS is placed in this gap, it is supposed to stay there untouched and continuously provide information about SNF until further decision on undertaking reprocessing or final disposal to geological repository. Thus the system will stay inside the dry cask for about 20 years[12]. During this time, it will be exposed to a high neutron and gamma flux (see section 2.3 for example of gamma and neutron production rates). All these imply that system should be very robust to withstand the harsh environment and be able to uninterruptedly transmit signal to the IAEA about the information on SNF. In other words, RMS has to maintain CoK about the dry cask content with minimum number of technical failures.

In addition to the technical constraints, IAEA requirements are stipulated by its limited budget and increasing number of nuclear facilities it needs to safeguard. Therefore, IAEA wants new safeguards systems to be [11]:

(1) Highly reliable and robust to reduce number of technical failures and number of maintenance inspections;
(2) Easy in operation to avoid, if possible, additional inspectors training;
(3) Cost-effective, and
(4) Remote to reduce number of on-site inspections.

3.2.2 Investigation of the Neutron and Gamma Flux Behavior Outside and Inside the Dry Cask

A set of tests was designed to investigate the neutron and gamma flux behavior inside and outside the dry cask in order to get information for choosing optimal RMS system location, type of detectors and their number. The series of tests included: (1) row test, (2) lattice test, and (3) open lid test. These tests used full MCNP model with radiation

[12] According to U.S Nuclear Regulatory Commission official web page, site-specific license for SNF storage is valid for 20 years [34].

source-term described in section 2.3. For plausibility, the dry cask was surrounded with the volume of air. Depending on the test purpose, point detector (F5 tally) or averaged flux in a cell (F4 tally) was used. Tests were performed for both gammas and neutrons. They were focused on the investigation of flux behavior in certain locations inside the dry cask, where RMS could potentially be placed, and also outside the dry cask. There were two main options for the RMS system placement: (1) side air gap between the MPC and the concrete canister; (2) and inside the air gap between the MPC lid and the concrete lid. These two options are highlighted in yellow in Fig. 9.

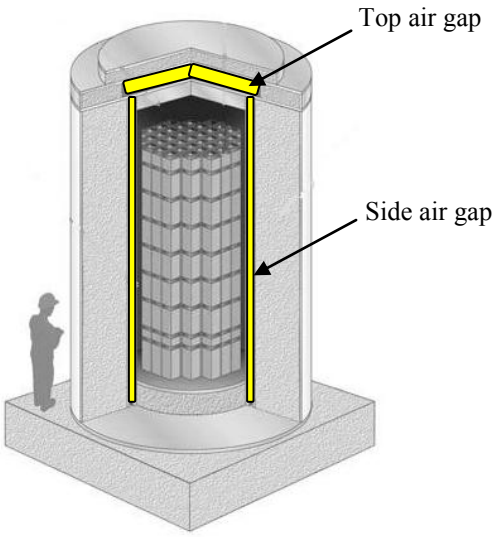

Fig. 9. Options for the RMS location inside the dry cask: side and top air gaps

3.2.2.1 Row Test

The *row test* was designed to find the contribution of each assembly row to the total flux or, in other words, to find out how deep one can "see" into the SNF rows behind the detector if a detector is placed on the dry cask side. It is clear that not all neutrons and gammas born inside the SNF will reach the detector placed either inside or outside the dry cask. Large number of particles gets absorbed inside the SNF and structural materials. Grid inside MPC (see Fig. 1 (d)), that holds all assemblies together, is usually

made of stainless steel and provides additional gamma shielding. Every grid cell also has Boral liner that serves as an additional neutron shielding. Therefore, if one places detector on the side, it is likely that not all SNF assemblies would contribute to the observed signal, especially those stores in the far back rows. It is fair to assume, that assemblies located closer to the detector provide larger contribution to the signal than those located on the opposite side of the dry cask. The test included four MCNP simulations. For the first simulation, radiation source-term was described in all 32 assemblies, which means that particles get started with equal probability in the whole volume of SNF. For the next three simulations, radiation source-term was described as if start in the first row of assemblies only, then in second and third row. The source strength was respectively changed depending on the number of assemblies in each row. The geometry of the model was the same for all four simulations, thus the first row of assemblies shielded signal from the second row; and the first and the second rows shielded signal from the third row. Point detector (F5 tally) was placed outside the dry cask at its middle height point, 30 (cm) away. Important to note that the outside detector position was also chosen with the intention to verify conclusions made in previous research work discussed in section 1.2, and it is assumed that the magnitude of flux inside a dry cask at the same middle height position is proportional to the one outside used in this test. The schematic of the test is shown in Fig. 10.

Results of the row test confirmed the assumption made about the peripheral assembly contributions: SNF assemblies from the first row dominate the signal estimated at the detector placed on the dry cask side. The row test results for the gamma flux are shown in Table 8. Obviously, gammas get heavily absorbed in the fuel due to their short mean free path in fuel and structural materials (about 2 (cm) for 600 (keV) gamma energy). Thus, the second row of assemblies contributes only 5% to the total flux and the signal from the third row is not virtually detectable (less than 1% contribution to the total measured flux). It was concluded that removal of assemblies from the second and third rows would be extremely hard to detect with gamma signal.

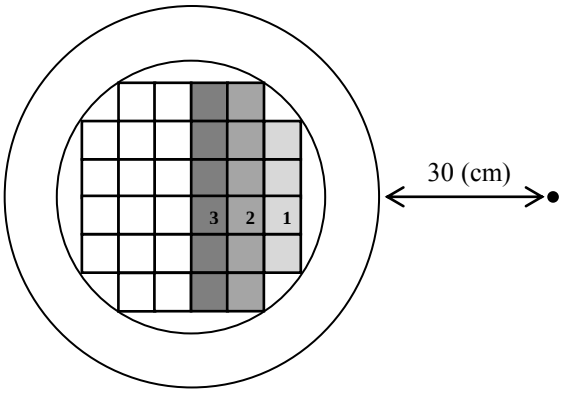

Fig. 10. Setup for the row test

Table 8. Row test results for the gamma flux

Row number	Total flux, ($\gamma \cdot s^{-1} \cdot cm^{-2}$)	Total flux rel. error	Row contribution, (%)	Row contribution rel. error
All	1.30E+05	0.034	100	0.033
1	1.22E+05	0.011	93.48	0.036
2	6.60E+03	0.044	5.05	0.056
3	9.28E+02	0.107	0.71	0.113
(1+2+3)	1.30E+05	0.116	99.25	0.122

The row test results for the neutron flux are shown in Table 9. The neutrons behavior is different, because they have longer mean free path (about 13 (cm) in stainless steel and 50 (cm) in concrete for 2 (MeV) neutron energy). Results of the test showed that even third row of assemblies provided considerable contribution of 13% to the total flux. However, if only one assembly is removed from the third or second row, it is unlikely that detector in side position will see at least 10% change of the signal. As in gamma case, it is fair to assume that only removal of assemblies from the first row will be detectable with neutrons in side position and will provide detectable change in the detector signal.

Table 9. Row test results for the neutron flux

Row number	Total flux, ($n \cdot s^{-1} \cdot cm^{-2}$)	Total flux rel. error	Row contribution, (%)	Row contribution rel. error
All	1.11E+02	0.013	100	0.015
1	4.94E+01	0.008	44.66	0.016
2	2.99E+01	0.004	27.04	0.013
3	1.49E+01	0.005	13.46	0.014
(1+2+3)	9.42E+01	0.01	85.17	0.017

3.2.2.2 Lattice Test

Another location for the RMS is the top of the MPC and between the MPC and concrete lids. In order to evaluate this location, the *lattice test* was set up. Its purpose was to investigate flux distribution on the top of MPC lid, in its center and at the edges. For this test point detector (F5 tally) was placed in the middle of the air gap on the top and against a center of each SNF assembly. For easier evaluation of test outcome, the results are presented in form of flux maps. These maps were created based on gamma and neutron flux values: the higher the value the darker the color. The maps are shown in Fig. 11.

The distribution of the gamma flux on the top of the MPC lid had expected behavior (Fig. 11 (a)). The minimum is in the center because large fraction of gammas gets absorbed in the fuel and mostly high energy gammas make through it. The maximum flux was observed above peripheral SNF assemblies. This phenomenon could be explained by MPC geometry. MPC has several empty cells on its edge (see Fig. 10) that are filled with air. Therefore, gammas easily leak to these cells from peripheral assemblies, and due to less attenuating materials on their way and collimation effect more gammas reach detectors on the edges. To further understand this behavior, it was also useful to look at the distribution of gamma energies on the top. After dividing the gamma energies in three main groups as it is shown in Table 10, it appeared that the number of high energy gammas reaching the MPC top is larger in the center. But on the edges, there are fewer amounts of high energy gammas because of the scattering. Also important to note, that high energy gammas constitute less than 1%

from the total flux. This explains the exposure rate behavior (Fig. 11 (b)). Even though high energy gammas should cause higher exposure rate than low energy, the number of high energy photons is significantly lower to cause higher exposure rate in the center of the MPC lid.

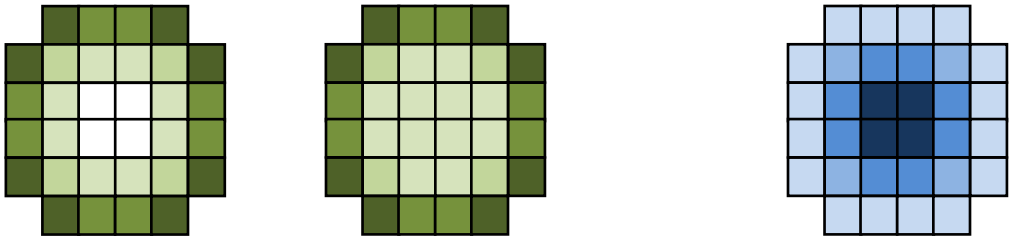

Gamma flux (a) Gamma exposure rate (b) Neutron flux (c)

Fig. 11. Flux distribution on the top of the MPC inside the dry cask

Table 10. Gamma energy distribution on the top of the MPC

Energy, (MeV)		Gamma flux, ($\gamma \cdot s^{-1} \cdot cm^{-2}$)*	
		Center	Edge
Low	(0 – 0.07)	7.56E+05	1.81E+06
Middle	(0.07 – 2.5)	2.38E+07	5.13E+07
High	(2.5 – 11)	1.03E+04	5.74E+02
Total:		2.46E+07	5.31E+07

**MCNP values have relative error of 10%*

Neutron intensity has completely opposite distribution than gamma (Fig. 11 (c)). As was already discussed, neutrons have larger mean free path, therefore they more easily pass through the fuel assemblies and MPC stainless steel lid causing flux maximum in the center of the MPC. Large mean free path also explains lower signal on

the edges, because neutrons from peripheral assemblies leak into the concrete easier than gammas and do not contribute to the signal on the top.

It is clear, that neutron and gamma flux measured on top against each assembly have two components: flux from assembly just below the detector and flux from adjacent assemblies. Thus removal of adjacent assemblies should supposedly change signal in the neighboring detector for both neutrons and gammas. Based on the lattice test results, if detectors are placed on the top of MPC, then gamma detector should be located at MPC edges and neutron detector in the center of the MPC lid. These positions correspond to the maximum flux values that were observed and should provide strong and reliable signal to the detectors.

3.2.2.3 Open Lid Test

The third test, named *open lid test,* was designed to evaluate both side and top detector positions with respect to the first action of any diversion scenario considered in this study – opening of the dry cask lid. Indeed, the first act that the adversary needs to do for diverting SNF assemblies from the dry cask is to open the concrete lid. A significant fraction of neutrons and gammas scatter off the concrete lid and contribute to the signal inside the detector kept below the concrete lid, thus lid removal should significantly affect the detector readings. It was expected that detectors would record significant drop in counts. Open lid test included two MCNP simulations with open and closed lid. Detector void cells (F4tally) were placed on the MPC top in the center and edge positions and one more detector was placed in the side gap at the cask middle height as shown in Fig. 12. Simulations were performed for the estimate of the neutron flux, gamma flux and gamma exposure rate. The results for the open lid test are shown in Table 11, Table 12 and Table 13.

Closed lid

(a)

Open lid

(b)

Fig. 12. Setup for the open lid test

Table 11. Results for the neutron flux in the open lid test

Detector Position	Neutron flux with closed lid, ($n \cdot s^{-1} \cdot cm^{-2}$)	Neutron flux rel. error	Neutron flux with open lid, ($n \cdot s^{-1} \cdot cm^{-2}$)	Neutron flux rel. error	Decrease in neutron flux, (%)	Decrease rel. error
Edge	5.11E+04	0.0169	1.56E+04	0.0293	69.47%	0.016
Center	6.18E+04	0.0155	2.00E+04	0.0259	67.56%	0.015
Side	3.65E+05	0.0067	3.65E+05	0.0067	0.18%	0.006

Table 12. Results for the gamma flux in the open lid test

Gamma flux						
Detector Position	Gamma flux with closed lid, ($n \cdot s^{-1} \cdot cm^{-2}$)	Gamma flux rel. error	Gamma flux with open lid, ($n \cdot s^{-1} \cdot cm^{-2}$)	Gamma flux rel. error	Decrease in gamma flux, (%)	Decrease rel. error
Edge	5.11E+04	0.0169	1.56E+04	0.0293	69.47%	0.074
Center	6.18E+04	0.0155	2.00E+04	0.0259	67.56%	0.111
Side	3.65E+05	0.0067	3.65E+05	0.0067	0.18%	0.005

Table 13. Results for the exposure rate in the open lid test

Exposure rate						
Detector Position	Exposure rate with closed lid, ($n \cdot s^{-1} \cdot cm^{-2}$)	Exposure rate rel. error	Exposure rate with open lid, ($n \cdot s^{-1} \cdot cm^{-2}$)	Exposure rate rel. error	Decrease in exposure rate, (%)	Decrease rel. error
Edge	1.30E+01	0.0797	3.01E+00	0.0631	76.82%	0.080
Center	8.17E+00	0.1413	2.50E+00	0.0591	69.36%	0.143
Side	3.58E+04	0.0062	3.52E+04	0.0140	1.74%	0.006

There are several observations that were made based on these results:

(1) The side detector position is not sensitive to open lid case for both neutron and gamma signal. The difference in flux constitutes less than 2%;

(2) The largest drop in gamma flux was observed in the edge detector position, which is consistent with the lattice test results;

(3) Neutron flux has almost equal drop for both edge and center positions. The edge value is higher than the center value by 1.91%, which is within 1σ interval and can be referred to statistical fluctuations. However, observed maximum value of neutron flux was consistent with the lattice test and was in the MPC center for both closed and open lid cases.

3.2.2.4 Contribution of (n, γ) Reactions to Total GammaFflux

The tests described above looked at gamma flux produced by fission products as a result of their decay. There is one more mechanism that could contribute to the total gamma flux - radiative neutron capture (n, γ) by certain nuclides. To simulate this contribution, MCNP input file could be modified to have neutrons as starting particles and gammas, produced through (n, γ) reactions, as particles counted by detectors. For this study lattice test was repeated to evaluate (n, γ) contribution. Based on its results decision was made not to consider (n, γ) contribution for the following reasons:

(1) Radiative capture gamma contribution is found to be less than 1% to the total flux (see Table 14);

(2) Most of these gammas are in high energy range - from 6 to 11 (MeV). They most likely will not be seen by detector. For instance, mean free path for 11 (MeV) gamma energy in air is 4000 (cm), in polyethylene – 50 (cm) and 16 (cm) in aluminum;

(3) Those MCNP simulations require a significant amount of additional computer time (about 8 hours per one simulation).

Table 14. Contribution of (n, γ) reactions to the total gamma flux based on the lattice test results

Energy, (MeV)	Total γ flux, ($\gamma \cdot s^{-1} \cdot cm^{-2}$)	(n, γ) flux, ($\gamma \cdot s^{-1} \cdot cm^{-2}$)	(n, γ) con*, (%)	Total γ flux, ($\gamma \cdot s^{-1} \cdot cm^{-2}$)	(n, γ) flux, ($\gamma \cdot s^{-1} \cdot cm^{-2}$)	(n, γ) con*, (%)
	Center			Edge		
Low	7.56E+05	1.75E+02	0.02%	1.81E+06	1.54E+02	0.01%
Middle	2.38E+07	8.64E+03	0.04%	5.13E+07	7.92E+03	0.02%
High	1.03E+04	3.03E+03	30%	5.74E+02	2.67E+03	100%
Total	2.46E+07	1.19E+04	0.05%	5.31E+07	1.07E+04	0.02%

** Con = contribution*

3.2.3 Final List of Requirements to the Preliminary RMS Design

The following requirements for the preliminary RMS design were derived from the previous analysis on the: (1) neutron/gamma flux behavior outside/inside the dry cask, (2) inherent dry cask limitations and (3) current requirements of the IAEA. The location of the RMS inside the dry cask was determined based on the review of the previous researchers work (section 1.2) and confirmed by the row test results described in the previous section. Row and open lid tests showed that system should be placed on the top of the MPC, between metal and concrete lids, because this position could detect opening of the dry cask concrete lid and has potential to detect the removal of SNF assemblies from different MPC cells (central and peripheral). Lattice test results suggested that neutron detectors should be placed in the center and gamma detectors on

the edges of the MPC lid. However, it was also decided to evaluate center position for the ionization chamber too.

To summarize, the following is the list of general requirements of the RMS design derived from the previous analysis and test results:

(1) Location on the top of the MPC lid:
   - Neutron detectors in the center;
   - Gamma detectors in the center or at the edges;

(2) Total height less than 18 (cm);

(3) Robustness to withstand high radiation environment for years;

(4) Low price.

Keeping in mind these general design requirements, the following sections describe in more details the choice of detectors, their number and other materials used to improve system performance and sensitivity.

3.3 Type and Number of Detectors

The choice of detectors was based on the requirement to measure both: neutron flux in the presence of gammas and gamma flux in the presence of neutrons.

There are different types of neutron detectors: plastic and liquid scintillators, gas filled detectors, lithium glass and fission chambers. Most of these detectors have high thermal neutron efficiency, but they are sensitive to the presence of a strong gamma field. The only exception is fission chambers. Fission chamber consists of a sensitive U-235 layer plated on its walls and filling gas (air or noble gases). It has the lowest detection efficiency for thermal neutrons, but this drawback is compensated by its low sensitivity to gamma exposure (up to 10^6 ($R \cdot h^{-1}$)) and large number of neutrons available for counting [27]. To minimize technical failures, like gas leakage, fission chambers can operate with fill gas under normal pressure. Fission chambers also meet such requirements as low price (compared to some other neutron detectors, for example, He-3 tubes) and ease of operation.

With regard to gamma detectors, ionization chambers were decided to be the best option. Semiconductor and scintillation detectors can be damaged by neutrons. Some of the ionization chamber fill gases may be sensitive to neutrons, like Xe. Thus air is a better alternative. Ionization chambers filled with air under normal pressure provides high reliability against technical failures such as loss of pressure and gas leakage. Also ionization chambers are cheap and easy to operate. More detailed information about neutron and gamma detectors, their operation principles and applications can be found in [27].

Today fission and ionization chambers can be manufactured in a variety of sizes. The diameter can vary from 1 (cm) to 15 (cm), and length – from 5 (cm) to 40 (cm). Also manufactures can produce chambers with custom dimensions and technical parameters required for certain application [28] [29]. For the purpose of this study, following detectors were chosen as a reference because of their appropriate dimensions [28]:

(1) LND, INC., 30783 Fission Counter;

(2) LND, INC., 50346 High Pressure Gamma Ionization Chamber.

This study did not include modeling of real detectors in MCNP, but instead void cells with realistic dimensions were used to represent them in the RMS model. Fission chamber cells have length equal to sensitive length of 20.32 (cm) and diameter 5.08 (cm), and its neutron sensitivity is 1 count per 10^3 thermal neutrons. Ionization chamber cells have length of 32.1 (cm) and diameter 5.08 (cm). The rest of technical specification and drawings of these detectors can be found and downloaded from manufacturer official web page [28].

Required number of detectors was determined by taking into account the requirements of robustness, effectiveness and minimization of technical failures. As a result, the RMS included two fission chambers and two ionization chambers. Two fission chambers were taken to provide more comprehensive coverage of MPC lid and to minimize number of technical failures. Two ionization chambers were chosen to

test their performance in the center and edge positions for different diversion scenarios described in the following section.

3.4 Detectors Mode of Operation and Output Signal

Fission chamber under consideration operates in a pulse mode. In this mode a separate electrical pulse is generated for every event, or in other words, for every interaction in a fissile material plated on the detector wall. Each pulse has its rise and decay times determined by electronics. It means that after each registered event, the system is not able to record another event until the previous pulse decays. This is called dead time of the system, which causes some fraction of neutrons not being detected. Along with other reasons, this dead time reduces the efficiency of the fission chamber. Therefore every fission chamber has a thermal neutron sensitivity parameter that determines how many of the incoming neutrons will be detected. For the chosen fission chamber it equals to 1 count per 10^3 thermal neutrons.

To distinguish between thermal, epithermal and fast neutrons in the current model, the incoming neutron flux was divided into energy groups according to the energy group structure presented in Table 15. This structure was determined based on natural cadmium[13] total cross-section behavior given in Appendix G. Every energy group includes cross-section feature like peak for thermal neutrons and resonance region. For calculating fission chamber neutron response only two thermal groups were used, which are 0.00E-00 - 6.00E-08 (MeV) and 6.00E-08 - 3.00E-07 (MeV). The rest of the groups were mainly used for investigation of other materials effect described in the following section. Thermal flux obtained from the MCNP model in units of ($n \cdot s^{-1} \cdot cm^{-2}$) was multiplied by measurement time (s), sensitive area (cm^2) and neutron sensitivity parameter ($count \cdot 10^{-3}$ neutrons) to get the number of counts produced by the fission chamber. To get thermal flux, detected in MCNP fission chamber cells,

[13] Natural cadmium was chosen because it was planned to be used as additional material in RMS design; the reasoning for that is described in the following section.

F2 tally[14] – average surface flux [25] – was used, as neutron interactions with sensitive layer occur in fission chamber walls.

Table 15. Neutrons energy group structure used for calculation of the fission chamber response

Group number	Energy	Cross-section feature	Energy group boundaries, (MeV)
1	Thermal	Before thermal peak	0.00E-00 - 6.00E-08
2	Thermal	Thermal peak	6.00E-08 - 3.00E-07
3	Epithermal	After thermal peak	3.00E-07 - 1.50E-05
4	Epithermal	Resonances	1.50E-05 - 1.60E-03
5	Fast	After resonances; fast region	1.60E-03 - 2.00E+01

Ionization chambers are rarely operated in pulse mode. Today ionization chambers are usually operated in current mode, which does not create separate electrical pulses for every event. Instead, it determines the mean intensity of gammas interacting with fill gas. It does not resolve incoming gammas by energy, it measures total exposure caused by gammas of different energies in fill gas volume. Gamma exposure for air is measured in units Roentgen per hour ($R \cdot h^{-1}$). To convert flux units ($\gamma \cdot s^{-1} \cdot cm^{-2}$) to ($R \cdot h^{-1}$) the response function for a range of gamma energies was calculated using the following formula [26]:

$$R(E) = \mathrm{C} \cdot E \cdot \left(\frac{\mu_{en}(E)}{\rho}\right)_{air}, \quad (4)$$

where

R(E) – energy dependent response function, ($R \cdot cm^2 \cdot \gamma^{-1}$)

E – gamma energy, (MeV)

$\left(\frac{\mu_{en}(E)}{\rho}\right)_{air}$ – mass energy absorption coefficient for air, ($cm^2 \cdot g^{-1}$)

[14] *F2 tally* is the average particle scalar flux on a surface. It can be thought as the limiting case of the track length estimator (f4 tally) when the cell thickness is approaching zero. For more information on F2 tally see [25].

$C = 1.835 \cdot 10^{-8}$ – constant for units conversion, ($C \cdot g \cdot kg^{-1} \cdot MeV^{-1}$). This constant takes into account conversion from (g) to (kg) and from ($C \cdot kg^{-1}$) to (R).

Then to get the total exposure rate, gamma flux for every energy bin is multiplied by related response function:

$$X = a \cdot \int dE\, R(E) \cdot \phi(E), \tag{5}$$

where

X – exposure rate, ($R \cdot h^{-1}$)

$R(E)$ - energy dependent response function, ($R \cdot cm^2 \cdot \gamma^{-1}$)

$\phi(E)$ – energy dependent gamma flux, ($\gamma \cdot s^{-1} \cdot cm^{-2} \cdot MeV^{-1}$)

$a = 3600$, conversion coefficient to convert seconds to hours, ($s \cdot h^{-1}$).

The response function calculated for every gamma energy bin and accepted energy structure is presented in Table 16. These numbers were used in MCNP input deck DE and DF cards [25], that way the model output results were shown exposure rate units right away. Important to note that this energy structure is different from one that used in generated radiation source-term (see section 2.3). The energy structure used in radiation source-term determines starting energy of gammas, while energy structure in Table 16 represents energy of gammas that enter ionization chamber volume.

Table 16. Response function values for the different gamma energies in air

Energy group boundaries, (MeV)		Mass energy absorption coefficient in air, $\left(\frac{\mu_{en}(E)}{\rho}\right)_{air}$, ($cm^2 \cdot g^{-1}$)	Response function, R(E), ($R \cdot cm^2$)
Lower boundary	Upper boundary		
0.00	0.01	4.74E+00	8.70E-10
0.01	0.015	1.33E+00	3.67E-10
0.015	0.02	5.39E-01	1.98E-10
0.02	0.03	1.54E-01	8.46E-11
0.03	0.04	6.83E-02	5.02E-11
0.04	0.05	4.10E-02	3.76E-11

Table 16. Continued

Energy group boundaries, (MeV)		Mass energy absorption coefficient in air, $\left(\frac{\mu_{en}(E)}{\rho}\right)_{air}$, ($cm^2 \cdot g^{-1}$)	Response function, R(E), ($R \cdot cm^2$)
Lower boundary	Upper boundary		
0.05	0.06	3.04E-02	3.35E-11
0.06	0.08	2.41E-02	3.53E-11
0.08	0.1	2.33E-02	4.27E-11
0.1	0.15	2.50E-02	6.87E-11
0.15	0.2	2.67E-02	9.81E-11
0.2	0.3	2.87E-02	1.58E-10
0.3	0.4	2.95E-02	2.16E-10
0.4	0.5	2.97E-02	2.72E-10
0.5	0.6	2.95E-02	3.25E-10
0.6	0.8	2.88E-02	4.23E-10
0.8	1	2.79E-02	5.12E-10
1	1.25	2.67E-02	6.12E-10
1.25	1.5	2.55E-02	7.01E-10
1.5	2	2.35E-02	8.61E-10
2	3	2.06E-02	1.13E-09
3	4	1.87E-02	1.37E-09
4	5	1.74E-02	1.60E-09
5	6	1.65E-02	1.81E-09
6	8	1.53E-02	2.24E-09
8	10	1.45E-02	2.66E-09

3.5 Other Materials and Their Dimensions

Essentially all neutrons born inside the SNF assemblies are fast because they emanate from spontaneous fission and (α, n) reactions. SNF itself and MPC structural materials do not provide sufficient moderation. If fission chambers are placed on top of the MPC lid without a moderating material, then 7.54E+03 ($n \cdot s^{-1} \cdot cm^{-2}$) thermal neutrons reach fission chambers, 2.21E+04 ($n \cdot s^{-1} \cdot cm^{-2}$) epithermal and 6.26E+04 ($n \cdot s^{-1} \cdot cm^{-2}$) fast. Therefore, in this case thermal neutrons fraction equals to ~8% from total incoming flux. To increase fraction of thermal neutrons and improve fission chamber detection efficiency, it is proposed to load it inside a polyethylene box, which can provide

moderation in order to slow down the fast and epithermal neutrons into thermal neutrons.

Another material proposed for usage is natural cadmium. Cadmium is known as strong thermal neutron absorber due to its 1/v behavior at the low energies and large resonance at ~ 0.2 (eV) (see Appendix C). It was suggested to place thin cadmium plate in between the MPC lid and fission chambers and inside polyethylene block as shown in Fig. 12 (b). Such configuration was expected to perform as thermal neutron flux suppressor: first neutrons coming from the bottom get thermalized in the bottom polyethylene layer and then get absorbed by the cadmium plate. It was assumed that this suppression effect would increase fission chambers sensitivity to the following cases:

(1) To the open lid case, because it suppress thermal flux coming from the bottom SNF assemblies and makes system rely more on thermalization of neutrons in the surrounding materials, particularly in the concrete lid;

(2) To the removal of SNF assemblies from periphery, because it suppresses thermal flux coming from the central SNF assemblies (located just below detectors) and makes system rely more on the neutron flux coming from the peripheral SNF assemblies.

Initial width and length for the polyethylene box and cadmium plate was chosen based on lattice test results. Figure 11 in section 3.2.2.2 shows that maximum neutron flux was observed just above four central assemblies or four MPC cells. According to developed design requirements, fission chambers were placed on the top of MPC lid and above these cells; centered with respect to X axis and symmetrical with respect to Y axis as shown in Fig. 13 (a). Therefore, polyethylene box and cadmium plate initial dimensions were chosen in such a way that they cover those four cells with maximum neutron flux and can enclose fission chambers inside. This corresponds to 46 (cm) for both length and width (see Table 3). The box thickness was chosen to be 7.08 (cm) which corresponds to 1 (cm) polyethylene layer thickness above and below detectors as shown in Fig. 13 (b).

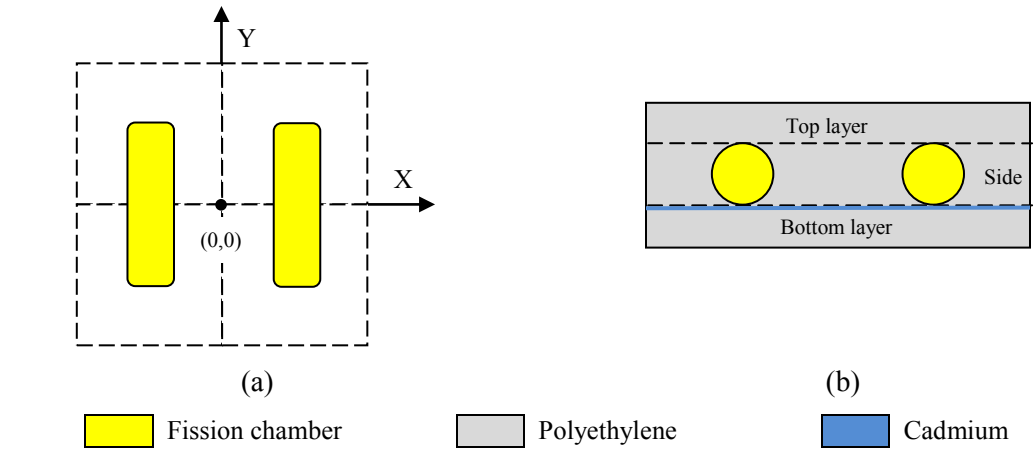

Fig. 13. Location of fission chambers (a) with respect to the MPC center and X, Y axis, and (b) inside polyethylene box. Blue line indicates location of the cadmium plate

Dimensions for the polyethylene box and cadmium plate were optimized through the series of MCNP simulations. In order to decrease computational time, these simulations used simplified dry cask model, created using MCNP feature of Surface Source-Write (SSW) and Surface Source-Read (SSR) [25]. The SSW card allows writing a surface source file that can be used in subsequent set of simulations. If particle crosses the surface of interest, it will be recorded, particularly its energy, position on the surface of interest and its direction cosines at each instant of surface crossing. Further, instead of using the whole model, one can use just the surface source. In this particular case, surface source was written over the fuel top surface. Then this surface source term was used in the simplified dry cask model that is shown in Fig.14. The input file for this model is presented in Appendix D. The SSR card was used in the subsequent MCNP simulations to read in the previously written SSW file as a surface source. This model does not include annular dry cask layers and, all the particles leaving the geometry were killed.

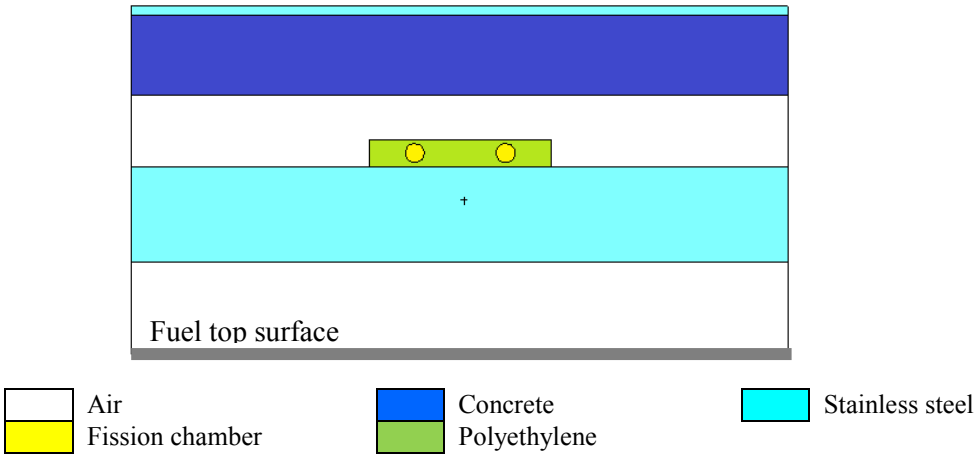

Fig. 14. A simplified MCNP model of the dry cask used for simulations aiming to optimize dimensions of the polyethyelene and cadmium plate

An impact of variation of polyethylene box size was studied through three separate series of MCNP simulations. The initial dimensions 46×46×7.08 (cm) were taken as a reference point. In each series, two of the initial dimensions were kept constant and one varied in the following order according to Fig. 12 (b): (1) polyethylene thickness below detectors (bottom layer), (2) polyethylene thickness above detectors (top layer) and (3) box length. Thus influence of each dimension was considered independently from others. The results of these simulations are graphically shown in Fig. 15, Fig. 16 and Fig. 17. Three neutron flux components (thermal, epithermal and fast) are plotted versus varying polyethylene thickness. Neutron flux values constitutes sum of fluxes observed in two fission chamber cells together. It is important to note that addition of polyethylene box with initial dimensions increased thermal neutron fraction up to ~50% from total incoming flux.

In first simulation series only bottom polyethylene thickness was varied from 0.1 to 7.5 (cm) with step 0.1 (cm) before 1 (cm) thickness and with step 0.5 (cm) after 1 (cm) thickness. It was found that increasing this dimension leads to increase of thermal flux and decrease of epithermal and fast flux components (Fig. 15). At thickness around 2.5 (cm) thermal flux reaches its maximum and starts to decrease, because less

and less thermal neutrons make it through polyethylene and get absorbed inside it without reaching the detectors; while epithermal and fast fluxes continuously decrease providing contribution to thermal flux component. The fact that thermal component continues to decrease shows that neutrons, coming from SNF assemblies just below detectors, provide main contribution into fission chamber count rate; and contribution from neutrons coming back to the detectors from other directions (from the top after scattering off concrete lid and sides) is not significant.

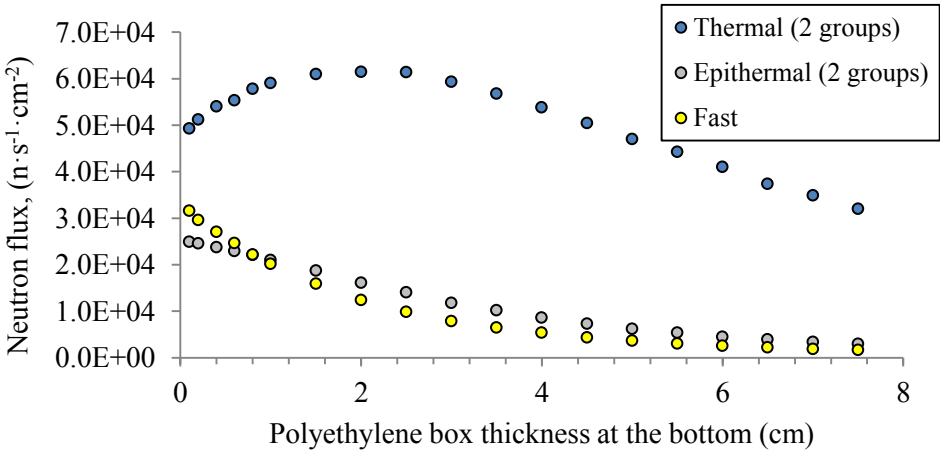

Fig. 15. Influence of the polyethylene bottom thickness on the neutron flux

The next simulation series was focused on varying polyethylene thickness above the detectors. The results, shown on graph in Fig. 16, demonstrate initial increase in thermal flux that eventually reaches the same value as in the previous test when top layer thickness became 1 (cm); after this point it continues to increase slightly until 2.5 (cm) thickness and finally remains virtually the same. This behavior can be explained by neutron reflection provided by this top layer of polyethylene: epithermal and fast neutrons, which came from the bottom and passed through detectors, now got thermalized in the top polyethylene layer and reflected back to the detectors. Further increasing of this top layer did not provide additional increase in thermal flux because

the thicker the layer the lesser amount of neutrons can make it back to the detectors without getting absorbed. Also these results confirmed that thermal neutrons coming from the bottom provide main contribution to count rate, and large part of thermal neutrons observed in this simulation series is due to constant 1 (cm) bottom layer of polyethylene. This constant bottom layer thickness also explains behavior of epithermal and fast fluxes. It can be seen from the previous simulation (Fig.15) that 1 (cm) bottom thickness allows only ~ 2.0E+04 epithermal and fast neutrons reach the detectors. The same value was observed in this test (Fig. 16) and it stayed constant until 1.5 (cm) top layer thickness; after this point number of epithermal and fast neutrons starts to decrease very slowly. This phenomenon confirmed that some fraction of fast and epithermal neutrons that were observed in the detector cells came from the top, and increase of top polyethylene layer cut this contribution.

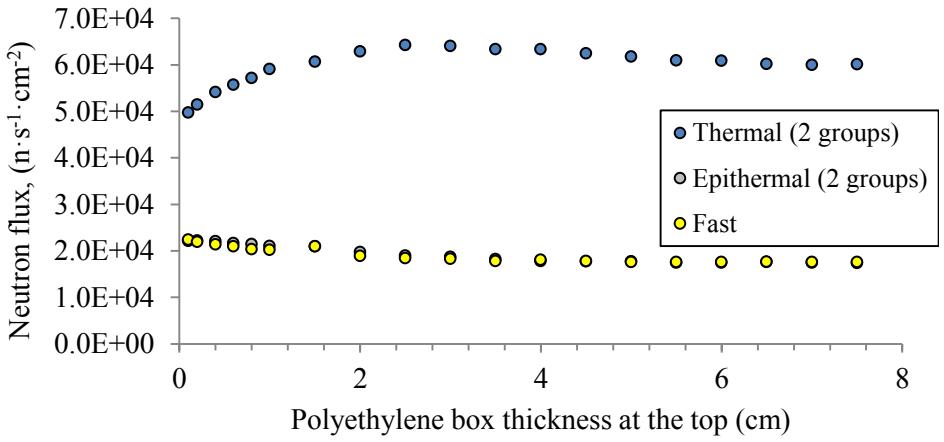

Fig. 16. Influence of the polyethylene top thickness on the neutron flux

The third simulation was performed with varying box length along X axis, keeping top and bottom polyethylene thickness constant and equal to initial dimension of 1 (cm). The box length varied from 30 to 46 (cm) with 4 (cm) step. The results are shown on graph in Fig. 17. This simulation showed that polyethylene box length does not affect

the detector count rate, because, as was shown before, system heavily relies upon neutrons coming from SNF assemblies that located just below it.

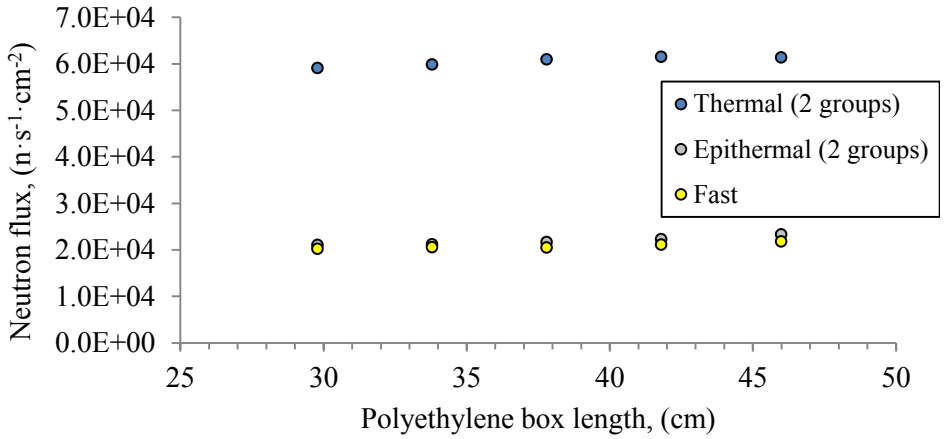

Fig. 17. Influence of the polyethelene box length on the neutron flux

Thus, it was concluded that polyethylene box with dimensions 46×46×7.08 (cm) does not reduce observable thermal flux and even provides additional moderation Also it was found that variation of polyethylene thickness below detectors affects thermal flux more than variation of this thickness above detectors. It was shown that thermal flux reaches its maximum with bottom layer thickness of 2.5 (cm) and with initial dimensions for top and side – 1 (cm) and 46 (cm) respectively. At this point it was not clear what bottom thickness should be chosen, the one that provides maximum thermalization or some value before it. The additional simulations were needed to determine this optimal bottom dimension. These simulations were decided to perform together with cadmium plate, but first cadmium plate thickness influence on thermal flux was studied.

The next series of simulations were performed to find optimal thickness for cadmium plate. The initial dimensions for polyethylene box remained the same: 46×46×7.08 (cm). The cadmium plate was placed between detectors and bottom polyethylene as shown in Fig. 13 (b). Its thickness was varied from 0.025 (cm) to 0.5 (cm) with step

of 0.025 (cm) until 0.1 (cm) thickness and with step of 0.1 (cm) after 0.1 (cm) thickness. The results of these simulations are shown in Fig. 18. It can be seen from the graph that 0.05 (cm) of natural cadmium was enough to absorb all thermal neutrons coming from the bottom. After this point thermal component curve reaches plateau. This is due to thermal neutrons coming to detectors from the top and sides that cadmium cannot affect. It was concluded that optimal cadmium thickness is 0.05 (cm).

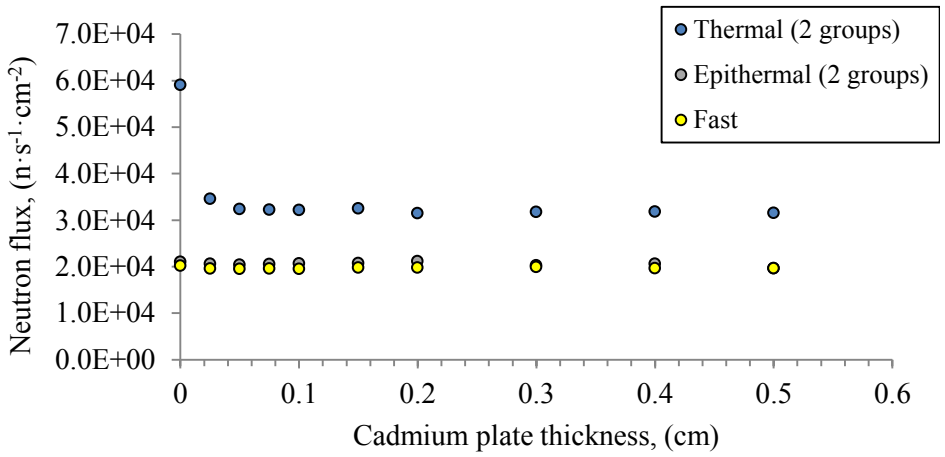

Fig. 18. Influence of the cadmium plate thickness on the neutron flux

As was mentioned above, after simulations with varying dimensions of polyethylene box, it was not clear what bottom thickness should be chosen, the one that provides maximum thermalization (2.5 (cm)) or some value before it (1 to 2 (cm)). The next set of four simulations with combination of polyethylene box and cadmium plate was performed to determine the optimal polyethylene bottom thickness. For this test optimal polyethylene box thickness was thickness that provides the largest drop in thermal flux with open dry cask lid. Simulations included polyethylene box with initial dimensions 46×46×7.08 (cm) and cadmium plate with thickness 0.05 (cm). The varying parameter was bottom thickness that was changed from 1 (cm) to 2.5 (cm) with step of 0.5 (cm). Simulations were performed with closed and open dry cask lid and results were

compared to calculate drop in thermal flux. Drop in thermal flux was calculated with respect to thermal flux observed with closed lid. The results are presented in Table 17.

Table 17. Results for simulations with combined geometry included cadmium plate and varying bottom polyethylene box thickness: closed and open lid cases

Polyethylene bottom thickness, (cm)	Thermal neutron flux with closed lid, ($n \cdot s^{-1} \cdot cm^{-2}$)	Thermal neutron flux with open lid, ($n \cdot s^{-1} \cdot cm^{-2}$)	Thermal flux drop, (%)
1	3.24E+04	1.99E+04	38.51%
1.5	3.04E+04	1.82E+04	40.06%
2	2.60E+04	1.45E+04	44.44%
2.5	2.39E+04	1.24E+04	48.11%

It can be seen from Table 17, that combination of cadmium plate and 2.5 (cm) polyethylene bottom thickness provided the largest drop in thermal flux than other combinations of the same cadmium plate and considered polyethylene bottom thicknesses. If one continues to increase this bottom thickness then ~90% drop in thermal flux can be achieved at 10 (cm). However, so much polyethylene in the design will make system bigger, and then it may not fit to the other dry cask models that have smaller gap between the MPC and concrete lids. Another disadvantage of thick polyethylene bottom layer is that with time it may significantly block the neutron signal and decrease system efficiency as neutron source will decay. Therefore ~50% drop in thermal flux, that can be achieved with 2.5 (cm) polyethylene bottom thickness, was accepted as optimal and balanced option.

3.5.1 Review of the Preliminary RMS Design

Based on all the previous analyses discussed (model tests, investigation of neutron/gamma flux behavior, simulations to choose optimal dimensions for polyethylene and cadmium) and carried out as part of this thesis study, the preliminary RMS design for SNF diversion test was made and it is shown in Fig. 19.

Figure 19 shows top and axial views to demonstrate the spatial position of RMS inside the dry cask. Ionization chambers are placed on the top of MPC stainless steel lid. Number of ionization chambers was already discussed before, and more than one was chosen to test its performance in different positions. There are total of two ionization chambers placed symmetrically in the center and at the edge positions. Fission chambers unit is placed on the top of the MPC too. Figure 19 (e) shows magnified image of the unit itself. Fission and ionization chambers are shown on separate figures and were modeled in separate MCNP input files, because MCNP simulations should be performed separately for gammas and neutrons.

The final dimensions of polyethylene box and cadmium plate are summarized in Table 18. It should be noted that proposed RMS design is easily fitted inside air gap between MPC lid and concrete lid, which is 18 (cm) for current dry cask model.

Table 18. Optimal dimensions for the polyethylene box and cadmium plate

Dimension	Value, (cm)
Polyethylene box:	
Length	46
Width	46
Height:	
Total	8.58
Top	1
Bottom	2.5
Cadmium plate:	
Length	46
Width	46
Thickness	0.05

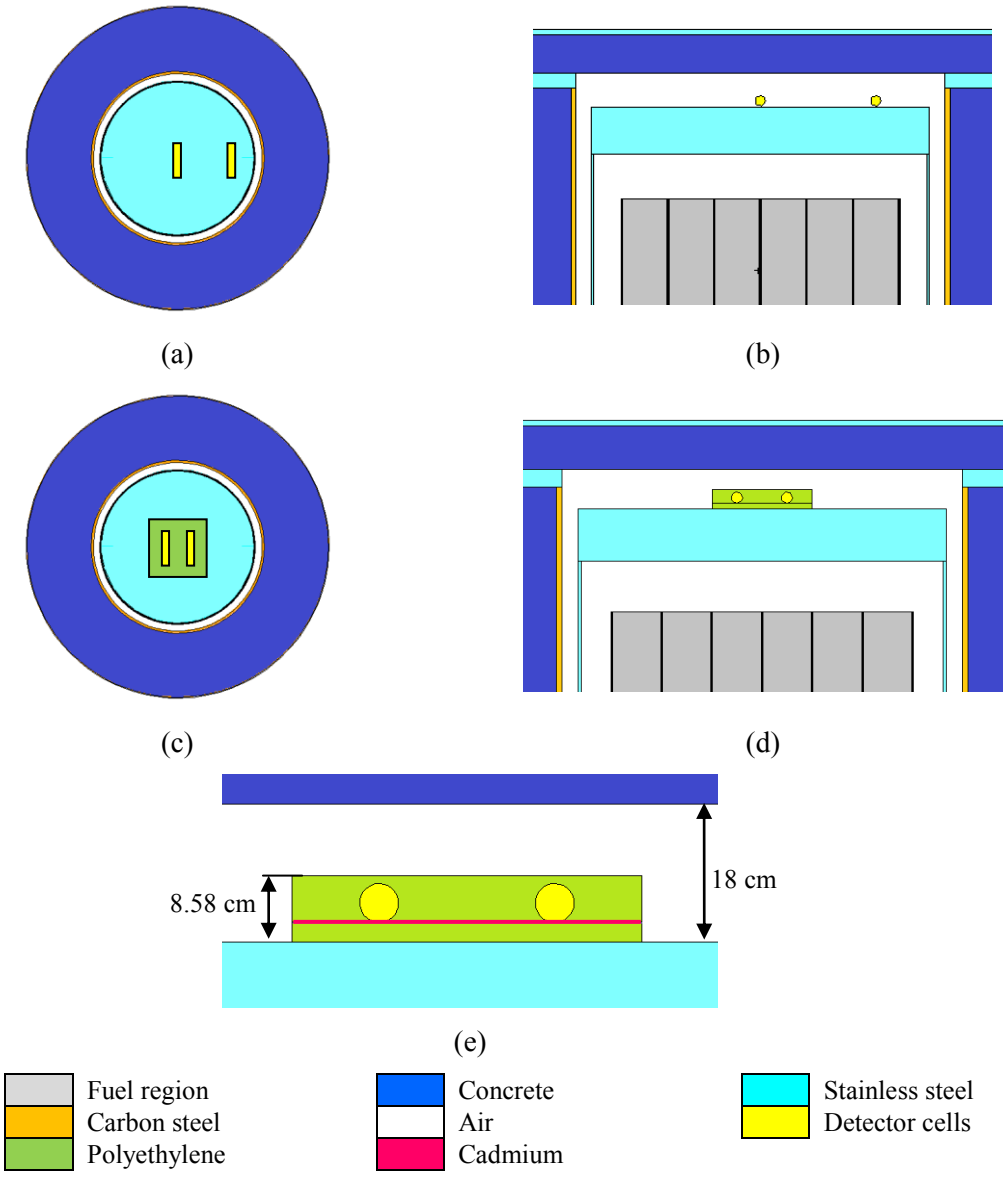

Fig. 19. Ionization (a, b) and fission chambers (c, d, e) layout in the preliminary RMS design

4. SPENT NUCLEAR FUEL DIVERSION ANALYSES

4.1 Procedure

The purpose of this section is to describe diversion analysis concept and important terminology from safeguards standpoint of view. The objective of the IAEA safeguards is "the timely detection of diversion of significant quantities of nuclear material from peaceful nuclear activities to the manufacture of nuclear weapons or of other nuclear explosive devices or for purposes unknown, and deterrence of such diversion by the risk of early detection" [4]. Diversion of nuclear material means "the undeclared removal of declared nuclear material from a safeguards facility" [4]. There are two types of diversions: abrupt and protracted. Abrupt diversion is referred to removal of 1 SQ or more of nuclear material in a short time that is less than the material balance period[15]; protracted diversion means removal of the nuclear material step-by-step in very small amounts (less than 1 SQ) over one or a few material balance periods. For this study, abrupt diversion of nuclear material was considered. The diversion pathway considered in this study included two steps: (1) opening of the dry cask lid and (2) removal of SNF assembly. It is also possible to remove individual fuel pins, but it is easier to do when SNF is stored in large storage pools. This type of diversion has been already considered by researches and special instrument was developed to detect individual fuel pins removal [30].

It was assumed that, if the adversary finds a way to remove SNF assemblies from the dry cask then he would substitute it with dummy assemblies. Otherwise, if adversary leaves empty cells, this diversion can possibly be detected by simple weighting of the dry cask. Therefore, each diversion scenario includes removal of SNF assembly from

[15] *Material balance period* (MBP) — under an INFCIRC/153-type safeguards agreement, the term is used to refer to the time between two consecutive physical inventory takings (PITs) (see No. 6.41) as reflected in the State's material balance report (see No. 12.7). Under an INFCIRC/66-type safeguards agreement, the term is used to refer to what more accurately should be called the book balance period, since the beginning and the ending dates of the period are not necessarily linked to PITs [4].*Depending on the type of NM and specific State's regulations, MBP can be from 1 month to 1 year.*

one of the MPC cells and substitution with dummy assembly, made out of stainless steel. This material was chosen, because it is easy to get and it does not fall under the IAEA safeguards; meanwhile, natural and depleted uranium export/import should be declared under INFCIRC/153 (article 34, (a), (b)) and INFCIRC/540 (article 2a(vi), (b), (c))[16]. Also INFCIRC/540 Article 2a (vi), (a) requires declarations about source material (i.e, depleted and natural uranium) "quantities, the chemical composition, the use or intended use whether in nuclear or non-nuclear use, for each location in [State] (if more than 10 (t) of U or 20 (t) of Th)".

The diversion scenarios analyzed considered the removal of one or two SNF assemblies from different MPC cells in the center and peripheral positions. Due to the symmetry of the MPC cell locations, assemblies were removed only from the top right quadrant. The diversion scenarios, with two dummy assemblies, were symmetrical version of some scenarios with one missing assembly. Radiation source-term was corrected to number of SNF assemblies present inside the dry cask after the SNF diversion. The simulations were performed for both neutron and gamma radiation. Description of the diversion scenarios in terms of source strength and SQ is presented in Table 19.

Table 19. Summary of diversion scenarios

Diversion scenario	Number of missing assemblies	Amount of Pu contained in missing assemblies, (kg) [Significant quantity]	Source strength corrected for missing assemblies	
			Gamma, ($\gamma \cdot s^{-1}$)	Neutron, ($n \cdot s^{-1}$)
1-5	1	5.51 [0.68]	6.54E+17	1.35E+10
6-8	2	11.02 [1.37]	6.33E+17	1.31E+10
0	0 (open lid)	0 [0]	6.13E+17	1.27E+10

[16] Full text of these documents can be found on official IAEA web page: <iaea.org>.

The reference run, which is dry cask with all 32 assemblies inside, was created to compare the results from the diversion scenario simulations. MCNP outputs for fission and ionization chambers signals were converted into counts and exposure rate ($R \cdot h^{-1}$) respectively. Since radiation measurements with large number of counts typically have Poisson distributions, it has assumed that the errors for all results were normally distributed. Therefore all results from both reference and diversion runs were plotted in the form of Gaussians. The mean value for the Gaussian was obtained directly from the MCNP simulations; the total uncertainty included MCNP uncertainty and virtual measurement uncertainty and was calculated using the following formula:

$$\sigma_{total} = \sqrt{\sigma_{mcnp}^2 + \sigma_{measurement}^2}\,, \tag{3}$$

where

σ_{total} – total uncertainty,

σ_{mcnp} – uncertainty from MCNP simulation,

$\sigma_{measurement}$ – virtual measurement uncertainty.

The virtual measurement uncertainty for fission chamber is a square root from counts recorded over certain period of time, because counts statistically represent direct number of successful events, i.e fissions in U-235 sensitive layer, which is a random process and obey normal distribution by nature. The measurement uncertainty for ionization chamber cannot be calculated the same way, because its readings are in form of exposure rate, which represents gamma energy deposition in air and does not directly represent number of decays resulting in gamma emission. Generally, ionization chamber measurement uncertainty is taken about 5-10%. For this study virtual measurement uncertainty was assumed to be 5%, and the total uncertainty also included relative error from the MCNP output[17].

[17] It is important to note that here MCNP uncertainty (random error) refers "only to the precision of the Monte Carlo calculations itself and not to the accuracy of the result compared to the true physical value" [25]. This random error is dependent on the number of particles used in simulation, and if one has enough computational time, it can be decreased to zero. The precision

Once all measurement results for the reference and diversion runs were obtained and plotted as Gaussians, *false alarm probability* (α) was set up as threshold and *non-detection probability* (β) was calculated for all diversions. False alarm probability is a probability that safeguards system detects diversion when, in fact, it did not occur. It is usually set at 5% or even less to avoid large number of false alerts. Non-detection probability is a probability to not detect diversion, when, in fact, it did occur [4]. This probability ideally should be about 5%, thus the detection probability (1-β) is close to 95-100%. It is always advisable to keep false alarm probability as low as possible, because every alarm requires response. In particular case it will require inspection, while the RMS goal is to reduce inspector's presence at the site to the time feasible. But then, minimization of the false alarm probability will increase non-detection probability as can be seen from the graph in Fig. 20 (a). On the other hand, increase of the false alarm probability will decrease non-detection probability. Therefore it is always important to find a balance between two of them.

The situation may be changed if one changes a measurement time. Increasing of the measurement time will give more counts in the detector and will reduce uncertainty, thus Gaussians will narrow down as shown in Fig. 20 (b). Then false alarm probability may be reduced to about 1% without increasing non-detection probability. But it is important to remember that time of measurement is critical parameter for the remote safeguards system. It should not be too long to facilitate adversary task, but it is also should not be too small to allow acceptable false alarm and non-detection probabilities. For the following diversion analysis the worst case scenario will be considered where, for simplicity of calculations, measurement time will be taken as 1 (s).

---

predicted in all the calculations performed for the SNF diversion analysis were less than 5% (see Appendix E and F). The MCNP accuracy was not verified in this study, because it does not involve any experiments. However, based on the previous MCNP validations, it is found to predict tally values (flux) within an accuracy of less than 10% [36] [37].

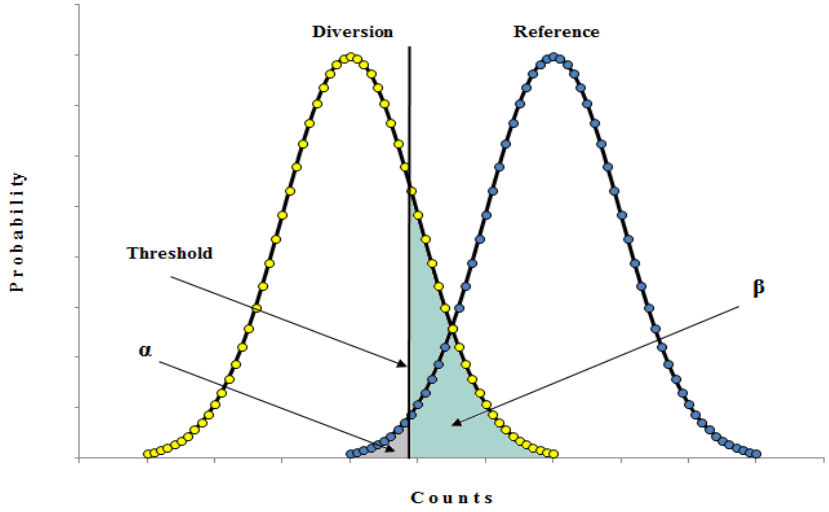

(a)

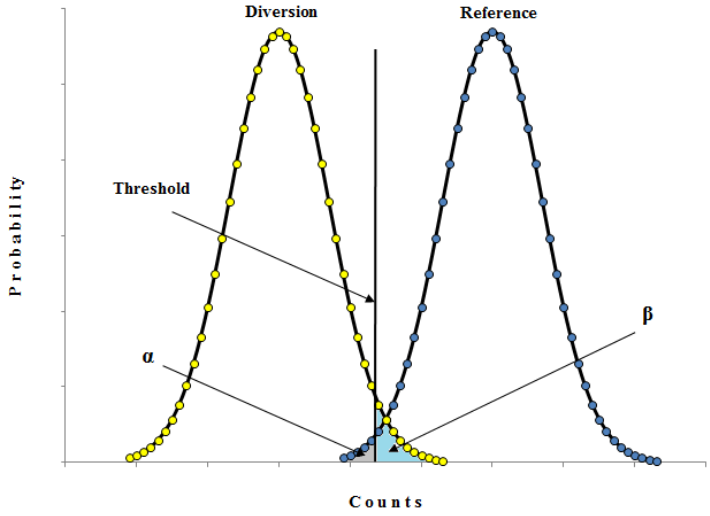

(b)

Fig. 20. Concept of the non-detection and false alarm probability with different measurement times: (a) measurement time – t_1, (b) measurement time – t_2, ($t_2 > t_1$)

4.2 Diversion Analysis with Neutron Radiation Signal

The results for the diversion analysis using neutron radiation signal and fission chambers are shown in Fig. 21 and on graphs in Appendix E. Here for the easier evaluation of the outcome, Fig. 21 presents only diversion scenario maps and calculated

non-detection probabilities. Appendix E contains results in graphical form (Gaussians) and related numerical data (detector readings and uncertainty used for plotting of Gaussians). For simplicity of calculations, measurement time was 1 (s). The number of counts presented is a sum of counts in two fission chambers together. The false alarm probability (α) was 5%, which correlated to 9.83E+03 counts from the reference run. The threshold was plotted on every graph in Appendix E and was used to calculate non-detection probability (β).

It can be seen from Fig.21, that all diversions with one SNF assembly removed were detected with non-detection probability less than 5%. Here it is important to note that the smallest β was observed not in the diversion scenario-3 (DS3), where assembly was removed just below detectors, but in the DS2 and DS1, where adjacent assemblies were missing. This is the effect of cadmium plate that suppresses thermal flux coming directly from the bottom and makes the system rely more on thermal flux coming from periphery assemblies. The cadmium plate effect was also verified by doing the same simulations but with polyethylene box only. This case yielded the non-detection probability about 30% for DS1 and DS4 where the farthest assemblies were removed. However, with cadmium plate these probabilities decreased to less than 5%.

The effect of cadmium plate was also observed in scenarios with removal of two SNF assemblies. The DS6 and DS8, where two assemblies were removed from the MPC periphery, were still confidently detected. At the same time, cadmium plate and polyethylene did not completely block neutron signal from SNF assemblies that are located just below the detector system. Even so cadmium plate cut thermal neutrons, epithermal neutrons can still come through, get attenuated in surrounding polyethylene box and contribute to count rate. Therefore the removal of SNF assemblies located just below detector unit was easily detected in DS7.

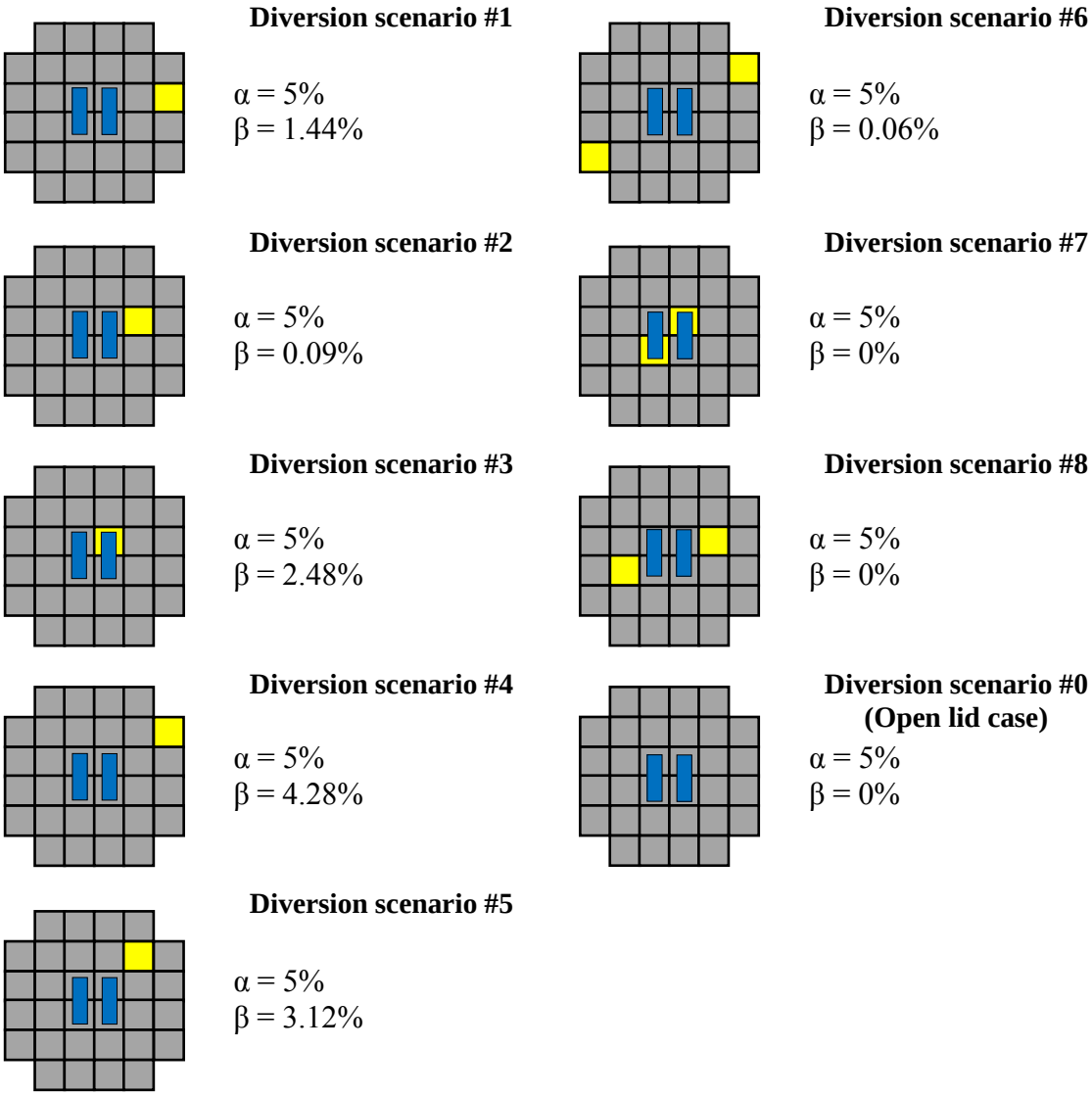

Fig. 21. Diversion analysis results for the fission chamber unit. The yellow cell indicates removed SNF assembly and substituted with dummy assembly made of stainless steel. The blue cell indicates location of the fission chambers

Open lid scenario was 100% detectable. Opening of the concrete lid causes a significant neutron leakage from the dry cask and significantly decreases the counts in detectors. This result justifies the chosen RMS location inside the dry cask. The results

also proved that the adversary could be caught at an early stage of diversion when dry cask lid is opened and before the removal of SNF assemblies.

As the last part of the diversion analysis with neutron radiation signal, measurement time was increased to 30 (s) to test if false alarm probability can be reduced to 1% while keeping acceptable values for the non-detection probability. It was found that increasing of measurement time up to 30 (s) decreased non-detection probability to 0% for all considered diversion scenarios. It means that proposed design can ensure low false alarm probability which is very important for safeguards systems working in remote operation mode. The results for the 30 (s) measurements are also presented in Appendix E in the graphical form with related numerical data (detector readings and uncertainties).

4.3 Diversion Analysis with Gammas Radiation Signal

The results for the diversion analyses using gamma radiation signal and ionization chambers in different positions on top of the MPC are shown in Fig. 22 and Fig.23 and also on graphs in Appendix F. The threshold, false alarm probability (α) was 5%, which correlated to exposure rate 5.48 ($R \cdot h^{-1}$) and 9.07 ($R \cdot h^{-1}$) respectively for the center and edge positions. These values were used to calculate non-detection probability (β). The only diversion case that was detected with confidence in both center and edge positions is the open lid case. The rest of the diversion scenarios did not cause significant drop in the gamma flux.

The ionization chamber located in the center position could not detect any diversions except for the open lid case. This outcome was partially caused by chamber location. It was placed above the edge of the metal grid between central MPC cells, so it did not look at any specific MPC cell. Due to short gamma mean free path in the fuel and structural materials this ionization chamber did not detect DS1, DS2, DS4, DS5, DS6 and DS8 where assemblies were removed from the far rows. However, the smallest non-detection probability was observed in DS1, DS4 and DS6 (Fig. 22), where assemblies were removed from the MPC periphery. This is consistent with gamma flux behavior observed in the lattice test: the maximum gamma flux was observed at the MPC

periphery, because gammas can easily escape through empty MPC cells and reach the detector. Thus, removal and substitution of peripheral assemblies causes less number of gammas escape through empty MPC cells and reach MPC top that leads to decrease in observed exposure rate.

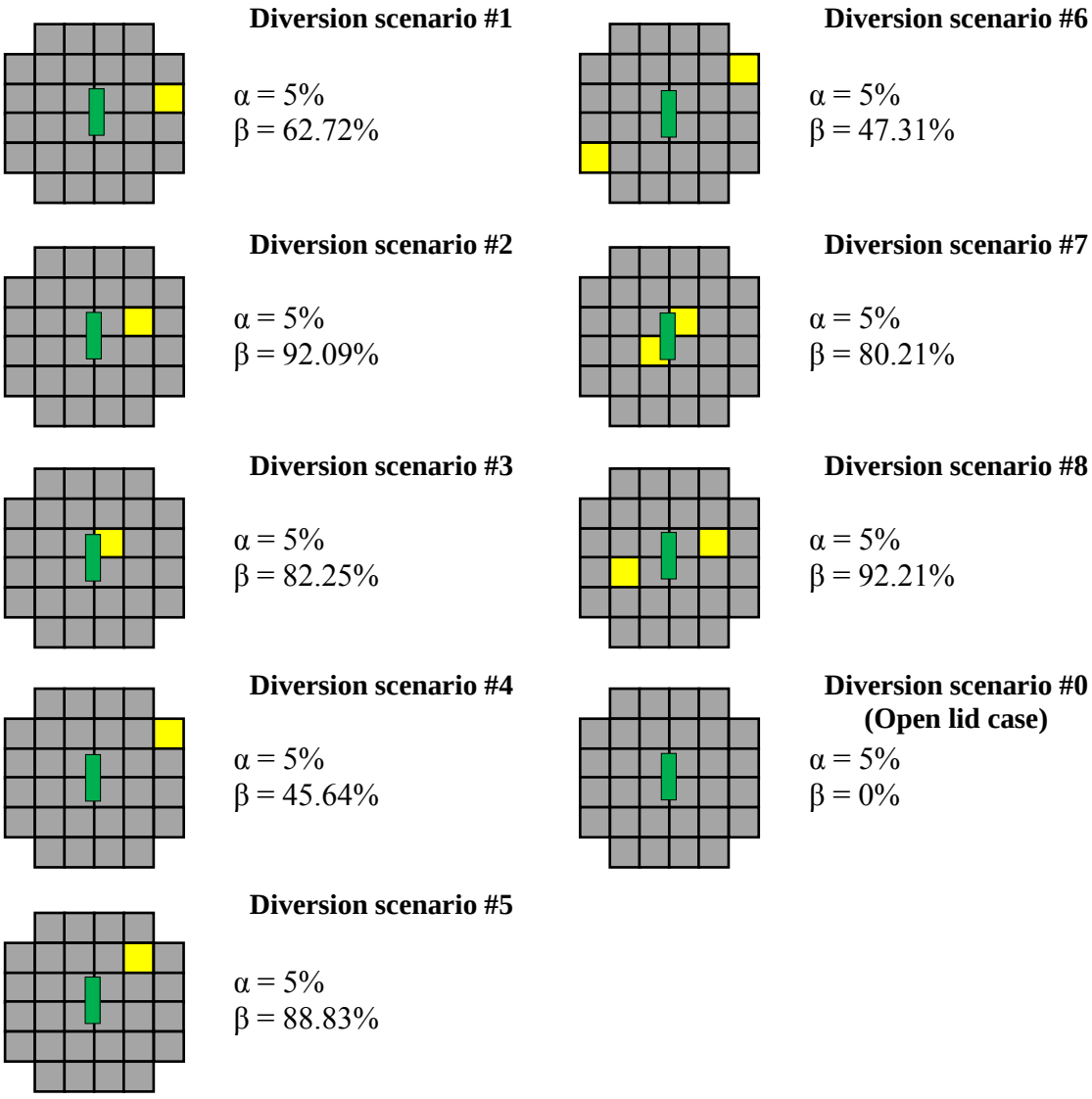

Fig. 22. Diversion analysis results for the ionization chamber in the center position. The yellow cell indicates removed SNF assembly and substituted with dummy assembly made of stainless steel. The green cell indicates location of the ionization chamber

Another observation that needs to be explained is the non-detection of DS3 and DS7, where SNF assemblies were removed from MPC cells just below the chamber. This phenomenon was explained by domination of high energy gamma in the center (see section 3.2.2.2) and its enhanced scattering off dummy assembly and also collimation effect that makes these scenarios hard to detect with gamma signal.

The ionization chamber located in the edge position had slightly better results. Important to note that besides location, there was one more difference from the previous case. This ionization chamber was actually placed directly above two of the MPC cells as can be seen from Fig. 19 and also Fig. 23. This chamber detected significant drop in the exposure rate when assemblies were removed from the MPC cells that are below or adjacent to it, like in the DS1, DS4 and DS6 (Fig. 23). However, it did not detect DS2, DS5 and DS8, where assemblies were also adjacent. This outcome was explained by assemblies' proximity to the edge of the MPC. In the DS1, DS4 and DS6 assemblies were next to the MPC edge and to the empty MPC cells; therefore their removal caused larger gamma flux leakage out of the geometry and eventually led to detection. On the contrary, in the DS2, DS5 and DS8 dummy assemblies were surrounded by other SNF assemblies, and this masked their substitution. Also dummy assemblies provided collimation of the gamma flux coming from the surrounded assemblies, which was an issue for the central ionization chamber too. The open lid scenario was detected with non-detection probability 0%. The DS3 and DS7 were not detected because removed assemblies were too far from the chamber.

Diversion analysis results with gamma radiation signal imply that for monitoring of all 32 assemblies several ionization chambers should be used. At least four ionization chambers have to be placed along MPC circumference to detect removal of peripheral assemblies with confidence.

A different measurement time was not considered for the ionization chambers, because they work in the current mode and provide continuous measurement of the exposure rate. As regard to the false alarm probability, if it will be reduced to 1%,

then both central and edge ionization chambers will still be able to detect the open lid scenario with non-detection probability 0%.

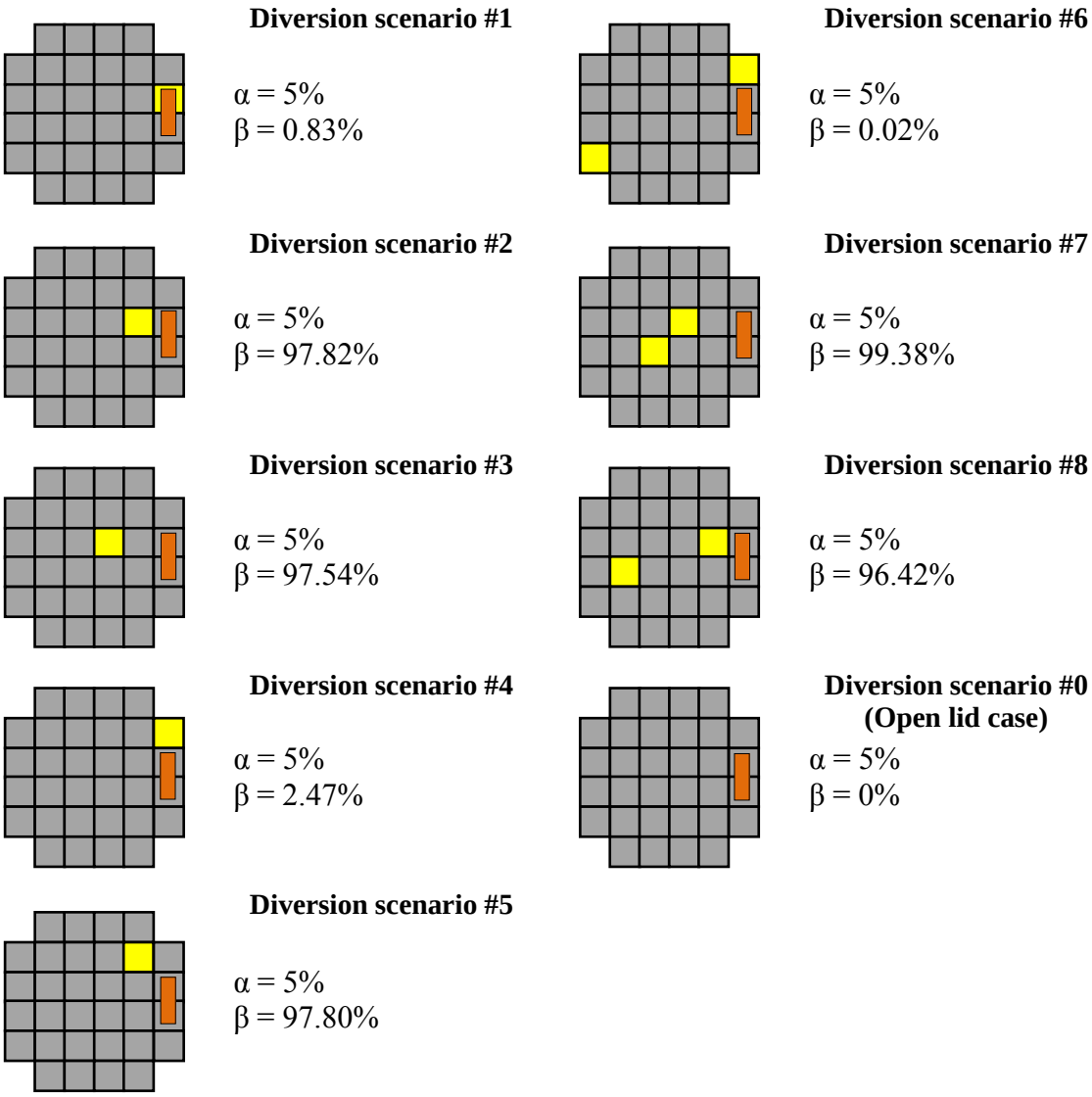

Fig. 23. Diversion analysis results for the ionization chamber in the edge position. The yellow cell indicates removed SNF assembly and substituted with dummy assembly made of stainless steel. The orange cell indicates location of the ionization chamber

4.4 Final Design of the RMS

Based on the results of diversion analyses, the preliminary design of RMS described in section 3.3.5 was slightly modified. The performance of the neutron detection unit (fission chamber with polyethylene box and cadmium plate) was satisfactory; therefore no changes to the initial design were needed. Gamma detection unit (ionization chambers) did not perform as expected. Diversion analysis showed that to achieve the same non-detection probability as with neutrons, one needs to place ionization chamber against each two adjacent SNF assemblies. This was not a desirable option as large number of ionization chambers will increase number of technical failures and complicate signal processing. Therefore, number of ionization chambers was reduced to one. In the interest of making RMS compact, this ionization chamber was left in the center position in between fission chambers as shown in Fig. 24.

Thus the primary detection mechanism of the RMS will be based on neutron radiation signal and fission chambers, and only one central ionization chamber will be kept to provide secondary confirmation for the open lid scenario. The final RMS design drawing is shown in Fig. 24.

The performance of the final design was tested only for the ionization chamber that was kept inside the polyethylene envelope. The test included two MCNP simulations with closed and open lid. The ionization chamber detected 55% drop in exposure rate and could detect the open lid scenario with non-detection probability $\beta = 0\%$. The additional performance testing for the fission chamber unit was not required, because the ionization chamber made of aluminum with air inside will be transparent for the neutrons due to their large mean free path. However, the addition of the ionization chamber decreased the total amount of polyethylene in the system that may affect thermalization of neutrons coming from the top and side. But it is not a concern here, because, as was shown earlier in section 3.5, the polyethylene top thickness did not influence neutron flux behavior as much as bottom polyethylene layer did, and bottom layer was not modified in the final RMS design.

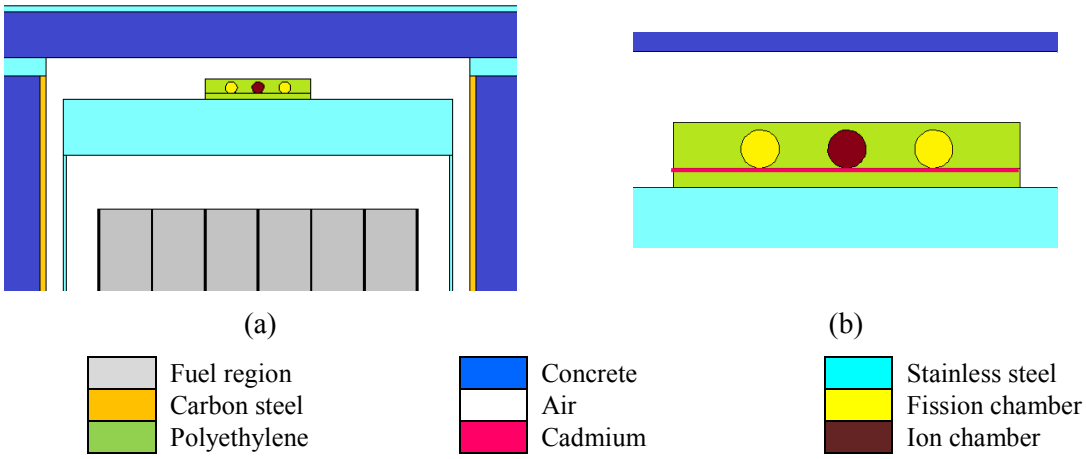

Fig. 24. Final RMS design: (a) side view and (b) magnified side view

It can be argued that usage of both neutron and gamma detectors is redundant, but then this redundancy ensures system reliability. A probability of failure is certainly higher for the fission chamber. Therefore if only fission chambers were used and they failed, then inspectors will need to go for an inspection to make sure that CoK about the dry cask content was not interrupted and also to fix the system. However, if there is an ionization chamber, which has very low probability of failure and ability to detect opening of the dry cask lid, then inspection can be postponed to the time feasible.

5. OTHER CONSIDERATIONS OF THE REMOTE MONITORING SYSTEM

5.1 Representation of Data to Inspectors

The important part of any detection system is to process and present the signal to decision makers, in particular case to the IAEA inspectors who will make a decision about requirement for an inspection. Once RMS is installed inside the dry cask, it will start measuring thermal neutron flux values and gamma exposure rate. It then can store and accumulate the measured data at the local server and then transmit it to the IAEA Headquarters in Vienna (see Fig.2, section 1.1.3). It is proposed that the readings from the fission and ionization chambers can be recorded in 30 (s) time intervals and be transmitted to the IAEA after an 8 hour period. Such small interval of 30 (s) was chosen because it is not long enough to open the dry cask lid and replace its content. These 30 (s) measurement results can be plotted against the predicted curve that will be calculated to reflect the expected detector readings taking into account neutron and gamma signal decay over time, loading SNF pattern and specific dry cask design. The predicted curve calculation can be based on depletion calculations using burn-up history for each assembly, and on MCNP model of the cask. It is expected that this curve should be different for every cask, because every cask has specific loading pattern with SNF assemblies of different initial enrichment, burn-up and cooling time. Then results can be presented to inspectors in the graphical form that shows RMS readings versus time and predicted curve. Further specially developed software could calculate the uncertainty and acceptable deviation from the predicted curve, and alarm in a case of anomaly or significant drop in neutron/gamma signal that could indicate opening of the dry cask lid or SNF diversion.

For this study expected neutron and gamma signal decay over 30 years was calculated using ORIGEN-ARP [23]. The results are presented on graphs in Fig. 25 in the form of production rates related to the 32 SNF assemblies with typical parameters for the enrichment, burn-up and cooling time previously used for source-term calculations (see section 2.3). It is fair to assume that production rates of both neutrons and gammas

are proportional to the counts and the exposure rate that will be observed in the detectors. Therefore Fig. 25 also presents probable detector readings (number of particles that will reach the detector) and simulated predicted curve. This data did not come from any experiments. It was simulated just to demonstrate how signal from the RMS can be presented to the inspectors. As can be seen from Fig. 25, the beginning of the RMS operation should start at the time of SNF loading. At this time inspectors will have certain knowledge about dry cask source-term and will take the first RMS measurement. These two points will serve as reference starting points for a construction of the related predicted curve for the particular cask.

The graphs on Fig. 25 also show contribution from particular isotopes that will dominate in the observed signal. Neutron emission rate will be dominated by Cm-244. It has about 18 years half-life and very high spontaneous fission rate, which ensures strong neutron signal for RMS over a long period of time. Gamma emission rate will be dominated by Cs-137 because of its long half-life (about 30 years) and it will continue to contribute to the ionization chamber gamma signal over a long period of time.

It can be also argued that proposed RMS can be used as re-verification instrument in a case of power outage or loss of communication. It can be assumed, that in the case of a power outage, system will be able to work for some time using emergency battery, but when the batteries are drained, the system will stop working. After power restoration, system will continue recording neutron/gamma signal and transmitting it to the inspectors. This signal can be compared against the predicted curve and previous readings to determine if it deviates more than expected within an accepted uncertainty. The same procedure is applicable for the case of communication loss. In both cases, evaluation of RMS readings should be coupled with evaluation of C&S data, like integrity of seals and security camera video records.

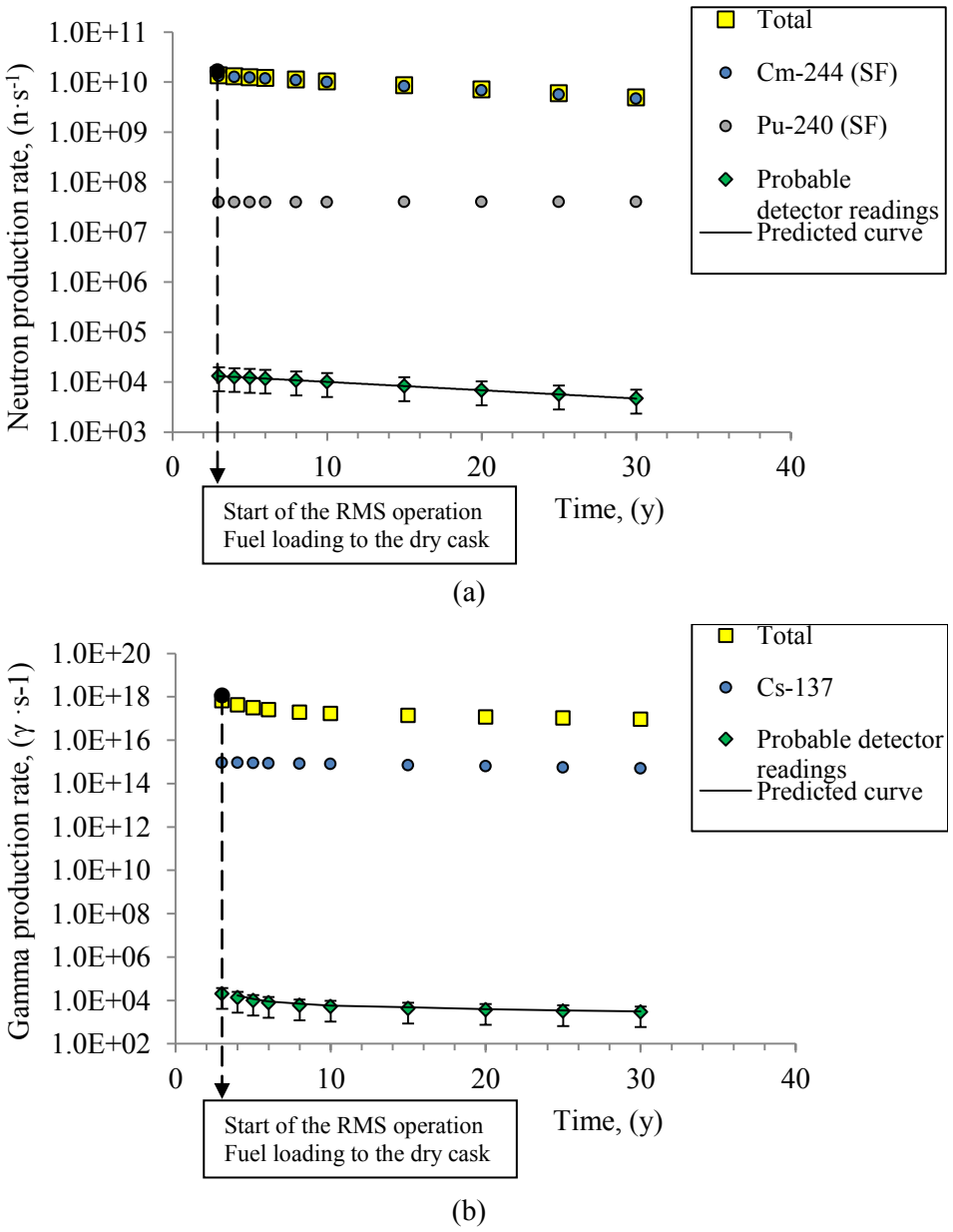

Fig. 25. RMS signal representation to the IAEA inspectors: (a) neutron case, and (b) gamma case

5.2 RMS and Current Safeguards Approach to Dry Cask Storage

The current safeguards approach for the dry cask storages was described in the introductory section. It was mentioned that usage of C&S measures as the core component of the current safeguards approach. This thesis study does not suggest that

application of proposed RMS should eliminate the usage of C&S; on the contrary all these measures should be working together to ensure that dry cask content is remaining as it was at the time of cask loading. For instance, failure of tamper indicating devices (seals) will not be of a big concern if RMS readings will follow predicted curve and no anomalies will be detected. In this case failure will more likely be caused by weather conditions. However, if RMS indicates anomaly with intact seals, then inspectors will need to undertake additional measurements to verify dry cask content, because corruption of seals is easier than corruption of neutron signal originating from SNF.

5.3 RMS Lifetime

One of the critical characteristics for the proposed RMS is its lifetime in high radiation environment. The RMS lifetime will be mainly dependent on the fission chambers and electronics durability under the constant neutron and gamma exposure.

There is one main component of the fission chamber that can degrade with time - fissile material layer (U-235). The degradation of this layer will be simply caused by thermal neutron interactions leading to fission events and thus decreasing uranium atoms density. This in turn will cause loss of fission chamber sensitivity. It was estimated that with constant thermal neutron flux equal to 6.18E+04 ($n \cdot s^{-1} \cdot cm^{-2}$) (see Table 11, center location) and sensitive material amount of 243 (mg) per one fission chamber [28], the expected fission rate in chamber walls will be 2.02E+04 ($fissions \cdot s^{-1}$) that will lead to decrease of uranium atoms density by less than 1% over 25 years. Thus burning-out of the fission chamber should not be the main problem in the RMS lifecycle.

The other point of concern is the electronics required for the RMS signal processing, like pre-amplifier. It most likely will fail first because of constant radiation exposure. Therefore it is probably worthwhile to place pre-amplifier outside the dry cask.

Other RMS materials, like polyethylene, will also degrade with time. The irradiation of polyethylene, in the presence of oxygen and at high dose rates, makes it brittle due to oxidative degradation and polymer cross-linking [31]. To prevent polyethylene envelope from a breakdown, the whole RMS unit can be placed inside a metal case with required

openings for the detectors and cables. However, continual irradiation may also cause build-up of hydrogen radicals (hydrogen gas) that need to be released out of the RMS case to prevent risk of explosion. The hydrogen build-up rate will depend on dose rate and polyethylene composition [32] [33]. The realistic polyethylene performance should be determined during the future RMS testing, and if hydrogen build-up will be indicated as an issue, then the RMS design should provide a mechanism for the pressure relief from the RMS case.

5.4 RMS Cost

It was mentioned several times before that due to increasing number of nuclear facilities, the IAEA needs to optimize number of inspections and make use of cost-efficient safeguards systems. Therefore cost of the proposed RMS design is an important factor for consideration. Table 20 below summarizes costs for all RMS components considered in this study. The total price constitutes $13,935. It does not include cost for the electronics and cables that will probably add a couple of thousand dollars more, which is negligible addition to the dry cask average cost about $1,000,000. Also this price does not include fabrication, installation and maintenance costs. In the future, if RMS will become an integral part of the dry cask designs, installation cost can be reduced significantly. At the current moment, RMS should be installed after SNF is loaded and sealed inside the MPC. It will require additional measures from the operator that needs to be negotiated with the IAEA inspectors.

Also important to remember, that this estimated price is for one RMS unit, i.e. per one dry cask. Thus RMS installation at the dry cask storage facility with 50 casks will cost about $700,000. This price become comparable with the cost of the imaging system, described in section 1.2, the cost of which is about $1,000,000. However, proposed RMS design provides remote monitoring option, high reliability and high detection probability of diversion with potential to decrease false alarm probability to 1%. Therefore RMS cost will be compensated by all the benefits it will provide to the IAEA inspectors.

Table 20. Cost estimation of the RMS components

RMS component	Cost, ($)
*Cadmium plate, (46×46×0.05) cm	1,135
*Polyethylene box, (46×46×7.08) cm	300
**Fission chamber (2 pieces)	12,000
***Ionization chamber (1 piece)	500
Total:	13,935

**The prices for cadmium and polyethylene were estimated using Goodfellowusa.com*
*** The price for fission chamber was obtained from the manufacturer*
****The price for ionization chamber was estimated during consultation with the thesis Advisory Committee*

6. FUTURE WORK

There are no doubts that additional experiments needed to evaluate other RMS parameters before it can be used. The most important question for the future consideration is the RMS lifecycle and degradation of the RMS components and supplemental materials under the constant radiation exposure. Another important field of study is the required electronics for the RMS operation and remote signal transmission. The other future work may also include:

(1) MCNP simulations with different dry cask designs;

(2) MNCP simulations with different SNF loading patterns that may include different burn-up and cooling time;

(3) Building the actual device and testing it inside a real dry cask;

(4) Investigation of feasibility of the RMS integration with different dry cask designs.

7. SUMMARY AND CONCLUSIONS

The diversion of SNF is one of the pathways in acquiring a nuclear weapons capability. There are few places where it can be obtained: nuclear reactor core, SNF wet storage, SNF dry storage and during SNF transportation. Diversion of SNF from reactor core and storage pool is a complicated task due to SNF radioactivity and sophisticated safeguards tools that are available to inspectors. However, once SNF is removed to dry storage, there is no more non-intrusive option to verify individual SNF assembly attributes. Moreover there is lack of efficient safeguards tools for re-verification of the dry cask content. The on-going research on development of re verification tools that can be used during inspections showed that radiation signal observed from dry cask is dominated by peripheral assemblies, and further research is needed to develop detectors that are able to see the inside of the dry cask. From other considerations, the IAEA has limited budget and wants to reduce on-site inspection activities wherever it is possible and replace them with remote monitoring systems [11]. Thus this study focused on the development of remote monitoring system (RMS) that is able to detect neutron and gamma signal coming from SNF inside the dry cask, detect diversions of both central and peripheral SNF, be cheap and robust.

A number of tests, simulations and analyses were performed to investigate neutron and gamma flux behavior inside the dry cask. Also diversion analyses were conducted to arrive at the final RMS design. It was concluded that RMS should rely on neutron signal with respect to the SNF removal detection and use neutron and gamma signal for detection of the open lid scenario. The final RMS design includes:

(1) For neutron detection: two fission chambers placed on top of the MPC lid and enveloped in the polyethylene box with a thin cadmium plate separating the detectors and polyethylene bottom layer. More than one fission chamber was used to decrease the number of technical failures that could happen and also to provide more comprehensive MPC lid coverage. The polyethylene provides additional moderation to increase the fraction of thermal neutrons. The cadmium

plate improves fission chamber sensitivity to opening of dry cask lid, but what is more important to removal of peripheral SNF assemblies.

(2) For gamma detection: one ionization chamber was placed on top of the MPC lid inside the same polyethylene box as fission chambers and in between those fission chambers. Since ionization chamber was able to see only the removal of SNF located just below it, it was decided that gamma signal will be used for detection of the open lid only and thus will provide secondary confirmation.

The proposed RMS design was able to detect diversions of one and two SNF assemblies using neutron signal and lid opening through neutron and gamma signal. Non-detection probability for all diversion scenarios using neutron signal was less than 5% (with false alarm probability – 5%). Non-detection probability for the open lid case using both neutron and gamma signal constitutes 0%. It was also shown that false alarm probability can be reduced to 1% with increase of measurement time up to 30 (s), which will yield non-detection probability 0% for all considered diversion scenarios using neutron signal for the open lid case and removal of the assemblies, and using gamma signal for the open lid case.

The proposed RMS design is the compact and cost-effective option. The RMS size and module structure should facilitate its installation process inside the dry cask with minimal annoyance of the operator. The choice of the detectors and simple operation principal ensures system robustness and easy signal processing. The system provides opportunity for the remote monitoring of the dry cask storage facilities, meeting all the established IAEA requirements. In the future RMS should be integrated in the future dry cask designs as part of the efforts to develop safeguards-friendly nuclear facilities.

REFERENCES

[1] M. Bunn, J. P. Holdren, A. Macfarlane, S. E. Pickett, A. Suzuki, T. Suzuki and J. Weeks, "Interim Storage of Spent Nuclear Fuel," Harvard University and University of Tokyo, Harvard, MA, June 2001.

[2] IAEA, "Operation and Maintenance of Spent Fuel Storage and Transportation Casks/Containers," IAEA, Vienna, Austria, January 2007.

[3] J. D. Werner, "U.S. Spent Nuclear Fuel Storage," Congressional Research Service, Washington, DC, May 2012.

[4] IAEA, "IAEA Safegaurds Glossary," IAEA, Vienna, Austria, June 2002.

[5] A. Jussofie, R. Graf and W. Filbert, "German Approach to Spent Fuel Management," in *Proceedings of Symposium on International Safeguards: Preparing for Future Verification Challenges*, Vienna, Austria, 1-5 November 2010.

[6] I. Perez Herrera, K. Murakami, H.-J. Schreiber, C. Olivieri, Y.-G. Lee, A. Ignachenko and V. Kulbakova, "IAEA Safeguards Implementation at Dry Spent Fuel Storage at Zaporoshe Nuclear Power Plant," in *Proceedings of the International Conference on Storage of Spent Fruel from Power Reactors*, Vienna, Austria, June 2003.

[7] R. Benjamin, Q. B. Truong, R. Keeffe and B. Green, "Designing a Safegaurds Approach for the Transfer and Storage of Used Fuel," in *Proceedings of the International Conference on Storage of Spent Fuel from Power Reactors*, Vienna, Austria, June 2003.

[8] M. Zendel, "IAEA Safeguards: Challenges in Detecting and Verifying Nuclear Materials and Activities," in *Proceedings of the 6th International Conference on Tunable Diode Laser Spectroscopy*, Reims, France, July 2007.

[9] R. Abedin-Zadeh, G. Bosler, R. Carchon and A. Lebrun, "IAEA Safeguards Verification Methods for Spent Fuel in Wet and Dry Storage," in *Proceedings of the International Conference on Storage of Spent Fuel from Power Reactors*, Vienna, Austria, June 2003.

[10] M. Barletta, N. Zarimpas and R. Zarucki, "Open Source Information Acquisition and Analysis in the International Atomic Energy Agency Department of Safegaurds," *Nuclear Technology,* vol. 179, no. 1, pp. 156-159, July 2012.

[11] J. Araujo, C. Charlier, D. Hatt, A. Lebrun, N. Muroya, P. Rance, I. Tsvetkov, R. Zarucki and M. Zendel, "Enhancing and Optimizing Safeguards Implementation by remote Safeguards Inspections," in *Proceedings of Symposium on International Safeguards: Preparing for Future Verification Challenges*, Vienna, Austria, November 2010.

[12] IAEA, "Staying Ahead of the Game," IAEA, Vienna, July 2007.

[13] A. Chen, Y. Chen, J. Wang, R. Sheu, Y.-W. Liu and S. Jiang, "A Comparison of Dose Rate Calculations for a Spent Fuel Storage Cask by Using MCNP and SAS4," *Annals of Nuclear Energy,* vol. 35, no. 12, pp. 2296-2305, December 2008.

[14] K.-P. Ziock, G. Caffrey, A. Lebrun, L. Forman, P. Vanier and J. Wharton, "The Feasibility of Cask "Fingerprinting" as a Spent-Fuel, Dry-Storage Cask Safegaurds Technique," LANL, Los Alamos, NM, October 2005.

[15] N. G. Chandergowda, "Assessment of the Fingerprinting Method for Spent Fuel Verification in MACSTOR KN-400 CANDU Dry Storage," Texas A&M University, College Station, TX, August 2012.

[16] INL, "Compton Dry-Cask Imaging System," 2011. [Online]. Available: http://www.inl.gov/rd100/2011/compton-dry-cask-imaging-system/. [Accessed 18 December 2012].

[17] "MCNP," Los Alamos National Laboratory, 2010. [Online]. Available: http://mcnp.lanl.gov/. [Accessed 18 12 2012].

[18] "Fuel Design Data," *Nuclear Engineering International,* vol. 48, no. 9, p. 28, September 2004.

[19] L. B. Wimmer, "Summary Report of Commercial Reactor Criticality Data for Three Mile Island Unit 1," Bechtel SAIC Company, LLC., Las Vegas, NV, August 2001.

[20] R. G. Williams III, C. J. Gesh and R. T. Pagh, "Compedium of Material Composition Data for Radiation Transport Modeling," PNNL, Richland, WA, April 2006.

[21] "Holtec International Final Safety Analysis Report for the HI-STORM 100 System (pp. 24, 125-125, 137)," HOLTEC, Jupiter, FL, January 2010.

[22] "Industry Spent Fuel Storage Handbook," Electric Power Research Institute, Palo Alto, CA, July 2010.

[23] "ORIGEN-ARP. Isotopic Depletion and Decay Analysis System," Oak Ridge National Laboratory, 2011. [Online]. Available: http://www.ornl.gov/sci/origen-arp/. [Accessed 18 12 2012].

[24] NIST, Radiation and Biomolecular Physics Division, "X-COM: Photon Cross Sections Database," The National Institute of Standard and Technology, December 2011. [Online]. Available: http://www.nist.gov/pml/data/xcom/index.cfm. [Accessed 28 December 2012].

[25] X-5 Monte Carlo Team, "MCNP Manual - A General Monte carlo N-Particle Transport Code, Version 5," Los Alamos National Laboratory, Los Alamos, NM, April 2003.

[26] K. Shultis and R. Faw, "Radiation Shielding", La Grange Park, IL: American Nuclear Society Inc., March 2000.

[27] D. Reilly, N. Ensslin, H. Smith and S. Kreiner, "Neutron Detectors," in *Passive Nondestructive Assay of Nuclear Materials*, Washington, DC, U.S. NRC, March 1991, pp. 377-407.

[28] "Designers and Manufacturers of Nuclear Radiation Detectors," LND, INC., [Online]. Available: http://www.lndinc.com/. [Accessed 12 11 2012].

[29] "PHOTONIS Nuclear Instrumentation," PHOTONIS, [Online]. Available: http://www.photonis.com/nuclear/. [Accessed 12 11 2012].

[30] Y. S. Ham, G. I. Maldonado, J. Burdo and T. He, "Development of a Safeguards Verification Method and Instrument to Detect Pin Diversion from PWR Spent Fuel Assemblies," in *Proceedings of the Symposium on International Safeguards*,

Vienna, Austria, October 2006.

[31] M. Pascu and C. Vasile, "Practical Guide to Polyethylene", Shawbury, UK: Rapra Technology Limited, April 2005.

[32] A. Singh, "Irradiation of Polyethylene: Some Aspects of Crosslinking and Oxidative Degradation," *Radiation Physics and Chemistry,* vol. 56, no. 4, pp. 375-380, October 1999.

[33] D. T. Reed, J. Hoh, J. Emery, S. Okajima and T. Krause, "Gas Production Due to Alpha Particle Degradation of Polyethylene and Polyvinylchloride," ANL, Argonne, IL, July 1998.

[34] "U.S Nuclear Regulatory Comission, Spent Fuel Storage Licensing," [Online]. Available: http://www.nrc.gov/waste/spent-fuel-storage/licensing.html. [Accessed 11 11 2012].

[35] *Private communication with Dr. Sunil S. Chirayath,* 2012.

[36] K. V. Subbaiah, D. Gopalani, C. S. Gautam, A. S. Jodha and L. R. Meghwal, "Gamma Radiation Protection Factor of Buikding Materials - Validation of wall reflections from measurements," *Indian Journal of Pure & Applied Physics,* vol. 48, no. November, pp. 774-777, November 2010.

[37] D. A. Torres, R. D. Mosteller and J. E. Sweezy, "Comparison of MCNP5 and Experimental Results on Neutron Shielding Effects for Materials," LANL, Los Alamos, NM, June 2004.

APPENDIX A

MCNP INPUT FILE FOR THE DRY CASK MODEL

```
Dry Cask Model with Capacity of 32 PWR SNF Assemblies

c    -- Cell Cards --
c    -Fuel rods-
101   1  -9.975    -102 -106 +105       u=1 imp:p=1
102   3  -2.46     -102 +106            u=1 imp:p=1
103   3  -2.46     -102 -105            u=1 imp:p=1
104   2  -6.53    +102 -103             u=1 imp:p=1
105   4  -1.205e-3  +103                u=1 imp:p=1
c
c    -Air (water) holes-
201   2  -6.53       +102  -103         u=2 imp:p=1
202   4  -1.205e-3   -102               u=2 imp:p=1
203   4  -1.205e-3  +103                u=2 imp:p=1
c
c    -Lattice cell #1-
301   0           -301 +302 -303 +304  lat=1  u=3 fill=0:18 0:18 0:0
     2 2 2 2 2 2 2 2 2 2 2 2 2 2 2 2 2 2 2
     2 1 1 1 1 1 1 1 1 1 1 1 1 1 1 1 1 1 2
     2 1 1 1 1 1 1 1 1 1 1 1 1 1 1 1 1 1 2
     2 1 1 1 1 1 2 1 1 2 1 1 2 1 1 1 1 1 2
     2 1 1 1 2 1 1 1 1 1 1 1 1 2 1 1 1 1 2
     2 1 1 1 1 1 1 1 1 1 1 1 1 1 1 1 1 1 2
     2 1 1 2 1 1 2 1 1 2 1 1 2 1 1 2 1 1 2
     2 1 1 1 1 1 1 1 1 1 1 1 1 1 1 1 1 1 2
     2 1 1 1 1 1 1 1 1 1 1 1 1 1 1 1 1 1 2
     2 1 1 2 1 1 2 1 1 2 1 1 2 1 1 2 1 1 2
     2 1 1 1 1 1 1 1 1 1 1 1 1 1 1 1 1 1 2
     2 1 1 1 1 1 1 1 1 1 1 1 1 1 1 1 1 1 2
     2 1 1 2 1 1 2 1 1 2 1 1 2 1 1 2 1 1 2
     2 1 1 1 1 1 1 1 1 1 1 1 1 1 1 1 1 1 2
     2 1 1 1 2 1 1 1 1 1 1 1 1 2 1 1 1 1 2
     2 1 1 1 1 1 2 1 1 2 1 1 2 1 1 1 1 1 2
     2 1 1 1 1 1 1 1 1 1 1 1 1 1 1 1 1 1 2
     2 1 1 1 1 1 1 1 1 1 1 1 1 1 1 1 1 1 2
     2 2 2 2 2 2 2 2 2 2 2 2 2 2 2 2 2 2 2        imp:p=1
c
c    -Assembly with boral on top-
401   0                -401 +491 -402 +492  fill=3 u=4 imp:p=1
402   4  -1.205e-3  +406 -403 -492 +405
                      #406 #407 #408 #409          u=4 imp:p=1
403   4  -1.205e-3  +401 -403 +492 -402           u=4 imp:p=1
404   4  -1.205e-3  +402 -404 +405 -403           u=4 imp:p=1
405   4  -1.205e-3  +405 -491 +492 -402           u=4 imp:p=1
406   6  -1.7        +406 -701 +777 -704          u=4 imp:p=1
407   5  -7.92     +701 -702 +777 -704        u=4 imp:p=1
```

```
408   5  -7.92     +703 -777 +406 -702        u=4 imp:p=1
409   5  -7.92     +704 -744 +406 -702        u=4 imp:p=1
410   5  -7.92    (+403:-406:+404:-405)       u=4 imp:p=1
c
c    -Assembly with boral on left-
501   0              -401 +491 -402 +492  fill=3  u=5 imp:p=1
502   4  -1.205e-3  +406 -403 -492 +405           u=5 imp:p=1
503   4  -1.205e-3  +401 -403 +492 -402
                    #506 #507 #508 #509          u=5 imp:p=1
504   4  -1.205e-3  +402 -404 +405 -403           u=5 imp:p=1
505   4  -1.205e-3  +405 -491 +492 -402           u=5 imp:p=1
506   6  -1.7        +705 -403 +733 -708          u=5 imp:p=1
507   5  -7.92       +706 -705 +733 -708          u=5 imp:p=1
508   5  -7.92       +707 -733 +706 -403          u=5 imp:p=1
509   5  -7.92       +708 -788 +706 -403          u=5 imp:p=1
510   5  -7.92      (+403:-406:+404:-405)         u=5 imp:p=1
c
c    -Assembly with boral on top and left-
601   0              -401 +491 -402 +492  fill=3 u=6 imp:p=1
602   4  -1.205e-3  +406 -403 -492 +405
                    #610 #611 #612 #613          u=6 imp:p=1
603   4  -1.205e-3  +401 -403 +492 -402
                    #606 #607 #608 #609          u=6 imp:p=1
604   4  -1.205e-3  +402 -404 +405 -403           u=6 imp:p=1
605   4  -1.205e-3  +405 -491 +492 -402           u=6 imp:p=1
606   6  -1.7        +705 -403 +733 -708          u=6 imp:p=1
607   5  -7.92       +706 -705 +733 -708          u=6 imp:p=1
608   5  -7.92       +707 -733 +706 -403          u=6 imp:p=1
609   5  -7.92       +708 -788 +706 -403          u=6 imp:p=1
610   6  -1.7        +406 -701 +777 -704          u=6 imp:p=1
611   5  -7.92       +701 -702 +777 -704          u=6 imp:p=1
612   5  -7.92       +703 -777 +406 -702          u=6 imp:p=1
613   5  -7.92       +704 -744 +406 -702          u=6 imp:p=1
614   5  -7.92      (+403:-406:+404:-405)         u=6 imp:p=1   l
c
c    -Assembly with no boral-
701   0              -401 +491 -402 +492  fill=3 u=7 imp:p=1
702   4  -1.205e-3  +406 -403 -492 +405           u=7 imp:p=1
703   4  -1.205e-3  +401 -403 +492 -402           u=7 imp:p=1
704   4  -1.205e-3  +402 -404 +405 -403           u=7 imp:p=1
705   4  -1.205e-3  +405 -491 +492 -402           u=7 imp:p=1
706   5  -7.92      (+403:-406:+404:-405)         u=7 imp:p=1
c
c    -Air for cask lattice #2-
801   4  -1.205e-3  -501                          u=8 imp:p=1
802   0              +501                         u=8 imp:p=0
```

```
c    -Cask lattice #2-
901   0           -408 +410 -409 +411  lat=1  u=9 fill=0:7 0:7 0:0
      8 8 8 8 8 8 8 8
      8 8 5 5 5 7 8 8
      8 5 6 6 6 6 7 8
      8 6 6 6 6 6 4 8
      8 6 6 6 6 6 4 8
      8 6 6 6 6 6 4 8
      8 8 6 6 6 6 8 8
      8 8 8 8 8 8 8 8                                  imp:p=1
902   0                -601 +104  -107 fill=9          imp:p=1
903   5  -7.92         +601 -602  +621 -623            imp:p=1
904   4  -1.205e-3  +602 -603 +629  -623               imp:p=1
9041  4  -1.205e-3  +602 -603 +623  -6231             imp:p=2
9042  4  -1.205e-3  +602 -603 +6231 -6232             imp:p=4
9043  4  -1.205e-3  +602 -603 +6232 -6233             imp:p=8
9044  4  -1.205e-3  +602 -603 +6233 -6234             imp:p=16
9045  4  -1.205e-3  +602 -603 +6234 -6235             imp:p=32
9046  4  -1.205e-3  +602 -603 +6235 -6236             imp:p=64
9047  4  -1.205e-3  +602 -603 +6236 -6237             imp:p=128
9048  4  -1.205e-3  +602 -603 +6237 -6238             imp:p=256
9049  4  -1.205e-3  +602 -603 +6238 -6239             imp:p=512
9030  4  -1.205e-3  +602 -603 +6239 -6240             imp:p=1024
9031  4  -1.205e-3  +602 -603 +6240 -6241             imp:p=2048
9032  4  -1.205e-3  +602 -603 +6241 -6242             imp:p=4096
9033  4  -1.205e-3  +602 -603 +6242 -6243             imp:p=8192
9034  4  -1.205e-3  +602 -603 +6243 -624              imp:p=16384
905   7  -7.82      +603 -604 +629  -623              imp:p=1
9051  7  -7.82      +603 -604 +624  -626              imp:p=16384
9052  7  -7.82      +603 -604 +623  -6231             imp:p=2
9053  7  -7.82      +603 -604 +6231 -6232             imp:p=4
9054  7  -7.82      +603 -604 +6232 -6233             imp:p=8
9055  7  -7.82      +603 -604 +6233 -6234             imp:p=16
9056  7  -7.82      +603 -604 +6234 -6235             imp:p=32
9057  7  -7.82      +603 -604 +6235 -6236             imp:p=64
9058  7  -7.82      +603 -604 +6236 -6237             imp:p=128
9059  7  -7.82      +603 -604 +6237 -6238             imp:p=256
9060  7  -7.82      +603 -604 +6238 -6239             imp:p=512
9061  7  -7.82      +603 -604 +6239 -6240             imp:p=1024
9062  7  -7.82      +603 -604 +6240 -6241             imp:p=2048
9063  7  -7.82      +603 -604 +6241 -6242             imp:p=4096
9064  7  -7.82      +603 -604 +6242 -6243             imp:p=8192
9065  7  -7.82      +603 -604 +6243 -624              imp:p=16384
906   8  -2.55      +604 -605 +629  -623              imp:p=1
9066  8  -2.55      +604 -605 +624  -626              imp:p=16384
9067  8  -2.55      +604 -605 +623  -6231             imp:p=2
9068  8  -2.55      +604 -605 +6231 -6232             imp:p=4
9069  8  -2.55      +604 -605 +6232 -6233             imp:p=8
9070  8  -2.55      +604 -605 +6233 -6234             imp:p=16
9071  8  -2.55      +604 -605 +6234 -6235             imp:p=32
9072  8  -2.55      +604 -605 +6235 -6236             imp:p=64
9073  8  -2.55      +604 -605 +6236 -6237             imp:p=128
9074  8  -2.55      +604 -605 +6237 -6238             imp:p=256
```

```
9075   8  -2.55      +604 -605 +6238 -6239          imp:p=512
9076   8  -2.55      +604 -605 +6239 -6240          imp:p=1024
9077   8  -2.55      +604 -605 +6240 -6241          imp:p=2048
9078   8  -2.55      +604 -605 +6241 -6242          imp:p=4096
9079   8  -2.55      +604 -605 +6242 -6243          imp:p=8192
9080   8  -2.55      +604 -605 +6243 -624           imp:p=16384
907    7  -7.82      +605 -606  +622 -626           imp:p=1
908    5  -7.92        -602 -621 +629              imp:p=1
909    4  -1.205e-3  -601 -104 +621                imp:p=1
910    5  -7.92        -605 -629 +622              imp:p=1
924    4  -1.205e-3  -601 -623  +107               imp:p=1
925    5  -7.92       -602 -6231 +623             imp:p=2
9251   5  -7.92       -602 +6231 -6232            imp:p=4
9252   5  -7.92       -602 +6232 -6233            imp:p=8
9253   5  -7.92       -602 +6233 -6234            imp:p=16
9254   5  -7.92       -602 +6234 -6235            imp:p=32
9255   5  -7.92       -602 +6235 -6236            imp:p=64
9256   5  -7.92       -602 +6236 -6237            imp:p=128
9257   5  -7.92       -602 +6237 -6238            imp:p=256
9258   5  -7.92       -602 +6238 -6239            imp:p=512
9259   5  -7.92       -602 +6239 -6240            imp:p=1024
9260   5  -7.92       -602 +6240 -6241            imp:p=2048
9261   5  -7.92       -602 +6241 -6242            imp:p=4096
9262   5  -7.92       -602 +6242 -6243            imp:p=8192
9263   5  -7.92       -602 +6243 -624             imp:p=16384
926    4  -1.205e-3  -603 -625  +624              imp:p=16384
927    5  -7.92        -606 +603  -625 +626       imp:p=16384
929    8  -2.55        -606 -6271 +625            imp:p=32768
9291   8  -2.55       -606 +6271 -6272            imp:p=65536
9292   8  -2.55       -606 +6272 -6273            imp:p=131072
9293   8  -2.55       -606 +6273 -6274            imp:p=262144
9294   8  -2.55       -606 +6274 -627             imp:p=524288
930    5  -7.92       -606 -628  +627             imp:p=1048576
931    4  -1.205e-3  -999 (+606:-622:+628)       imp:p=1048576
999    0               +999                       imp:p=0

c    -- Surface Cards --
c    -Fuel rod surfaces-
102    c/z   -1.258823529 -1.258823529 0.4178
103    c/z   -1.258823529 -1.258823529 0.475
104    pz     0.0
105    pz     9.1
106    pz   397.2
107    pz   406.3
c
c    -Lattice #1 cell surfaces-
301    px    -0.629411765
302    px    -1.888235294
303    py    -0.629411765
304    py    -1.888235294
c
c    -Lattice #1 boundaries and additional layers around-
401    px    20.82519824
```

```
491    px    -0.684021765
402    py    20.82519824
492    py    -0.684021765
403    px    21.22524824
404    py    21.22524824
405    px    -1.084071765
406    py    -1.084071765
c
c    -Lattice #2 cell surfaces-
408    px    21.58843574
409    py    21.58843574
410    px    -1.447259265
411    py    -1.447259265
c
c    -Air in lattice #2-
501   cz     50
c
c    -Outer cylinders-
601    c/z   90.69552076 90.69552076 83.05637951
602    c/z   90.69552076 90.69552076 84.40187951
603    c/z   90.69552076 90.69552076 91.94637951
604    c/z   90.69552076 90.69552076 94.48637951
605    c/z   90.69552076 90.69552076 164.3363795
606    c/z   90.69552076 90.69552076 165.1013795
c
c     -Top and bottom layers-
621    pz    -6.35
622    pz   -34.2555
623    pz   429.59
6231   pz   431.2981538
6232   pz   433.0063075
6233   pz   434.7144613
6234   pz   436.422615
6235   pz   438.1307688
6236   pz   439.8389226
6237   pz   441.5470763
6238   pz   443.2552301
6239   pz   444.9633838
6240   pz   446.6715376
6241   pz   448.3796913
6242   pz   450.0878451
6243   pz   451.7959989
624    pz   453.59
625    pz   471.59
626    pz   463.59
627    pz   491.59
6271   pz   476.3514966
6272   pz   480.5518566
6273   pz   484.7522166
6274   pz   488.9525766
628    pz   494.13
629    pz    -7.6955
```

```
c    -Boral-SS layer-
701    py    -0.827531765
702    py    -0.738631765
703    px     0.540511765
733    py     0.629411765
704    px    19.5117647
744    px    19.6006647
705    px    20.96870824
706    px    20.87980824
707    py     0.540511765
777    px     0.629411765
708    py    19.5117647
788    py    19.6006647
c
c    -Problem boundary-
999    s     90.69552076 90.69552076 0 5000

c     -- Data Cards --
MODE p
SDEF POS=D1 x=FPOS D2  y=FPOS D9  z=D16  ERG=D17
SI1  L  0 0 0  0 0 0  0 0 0  0 0 0  0 0 0  0 0 0
          0 0 0  0 0 0  0 0 0  0 0 0  0 0 0  0 0 0
          0 0 0  0 0 0  0 0 0  0 0 0  0 0 0  0 0 0
          0 0 0  0 0 0  0 0 0  0 0 0  0 0 0  0 0 0
          0 0 0  0 0 0  0 0 0  0 0 0  0 0 0  0 0 0
          0 0 0  0 0 0
SP1  D  1 1 1 1 1 1 1 1 1 1 1 1 1 1 1
           1 1 1 1 1 1 1 1 1 1 1 1 1 1 1
DS2  S  3 3 3 3 4 4 4 4 4 4 5 5 5 5 5 5
           6 6 6 6 6 6 7 7 7 7 7 7 8 8 8 8
SI3  22.40628324 43.80628324
SP3  0          1
SI4  45.44197824 66.84197824
SP4  0          1
SI5  68.47767324 89.87767324
SP5  0          1
SI6  91.51336824 112.9133682
SP6  0          1
SI7  114.5490632 135.9490632
SP7  0          1
SI8  137.5847582 158.9847582
SP8  0          1
DS9  S  10 11 12 13 14 10 11 12 13 15
           14 10 11 12 13 15 14 10 11 12 13 15
           14 10 11 12 13 15 10 11 12 13
SI10  45.44197824 66.84197824
SP10  0          1
SI11  68.47767324 89.87767324
SP11  0          1
SI12  91.51336824 112.9133682
SP12  0          1
SI13  114.5490632 135.9490632
SP13  0          1
```

```
SI14  22.40628324 43.80628324
SP14  0          1
SI15  137.5847582 158.9847582
SP15  0          1
SI16  9.1 397.2
SP16  0   1
SI17  0       2.00E-02 3.00E-02 4.50E-02 7.00E-02
       1.00E-01 1.50E-01 3.00E-01 4.50E-01 7.00E-01
       1.00E+00 1.50E+00 2.00E+00 2.50E+00 3.00E+00
       4.00E+00 6.00E+00 8.00E+00 1.10E+01
SP17  0 5.79E+15 1.27E+15 1.43E+15 1.05E+15
        7.77E+14 1.01E+15 7.38E+14 3.94E+14 5.83E+15
        1.83E+15 2.71E+14 2.23E+13 2.40E+13 5.46E+11
        4.98E+10 1.87E+07 2.16E+06 2.48E+05 2.04E+16
m1    92234.01p  0.00006     $Fuel
       92235.01p  0.039
       92238.01p  0.96094
        8016.01p  2
m2    50000.01p  1.5         $Cladding
       26000.01p  0.2
       24000.01p  0.1
       28000.01p  0.007
       40000.01p  98.193
m3     2004.01p -4.519E-3    $Mixture for top and bottom plenums
      50000.01p -0.019453
      26000.01p -0.00122
      24000.01p -0.000568
      28000.01p -4.48857E-5
      40000.01p -0.978668
m4     6000.01p  0.000151    $Air
       7014.01p  0.784437
       8016.01p  0.210750
      18000.01p  0.004671
m5   24000.01p  0.202087    $ MPC grid material
      25055.01p  0.020133
      26000.01p  0.688268
      28000.01p  0.089514
m6    13027.01p -0.6861      $ Boral
        6000.01p -0.0682
        5010.01p -0.044226
        5011.01p -0.201474
m7     6012.01p  0.022831    $Carbon steal
      26000.01p  0.977170
m8    14000.01p -0.315       $Concrete
      13027.01p -0.048
       8016.01p -0.5
       1001.01p -0.006
      11023.01p -0.017
      20000.01p -0.083
      26000.01p -0.012
      19000.01p -0.019
```

APPENDIX B

RADIATION SOURCE-TERM FOR THE ONE PWR SNF ASSEMBLY

Gamma Energy Groups and Their Respective Source Strengths

# Energy group	Energy group boundaries, (MeV)	Production rate, ($\gamma \cdot s^{-1} \cdot MeV^{-1}$)
1	0.00E+00 - 2.00E-02	5.79E+15
2	2.00E-02 - 3.00E-02	1.27E+15
3	3.00E-02 - 4.50E-02	1.43E+15
4	4.50E-02 - 7.00E-02	1.05E+15
5	7.00E-02 - 1.00E-01	7.77E+14
6	1.00E-01 - 1.50E-01	1.01E+15
7	1.50E-01 - 3.00E-01	7.38E+14
8	3.00E-01 - 4.50E-01	3.94E+14
9	4.50E-01 - 7.00E-01	5.83E+15
10	7.00E-01 - 1.00E+00	1.83E+15
11	1.00E+00 - 1.50E+00	2.71E+14
12	1.50E+00 - 2.00E+00	2.23E+13
13	2.00E+00 - 2.50E+00	2.40E+13
14	2.50E+00 - 3.00E+00	5.46E+11
15	3.00E+00 - 4.00E+00	4.98E+10
16	4.00E+00 - 6.00E+00	1.87E+07
17	6.00E+00 - 8.00E+00	2.16E+06
18	8.00E+00 - 1.10E+01	2.48E+05
Total:	-	2.04E+16

Neutron Energy Groups and Their Respective Productions Rates

# Energy group	Energy group boundaries, (MeV)	Production rate, ($n \cdot s^{-1} \cdot MeV^{-1}$)
1	3.000E-09 - 1.000E-11	2.92E-05
2	7.500E-09 - 3.000E-09	7.85E-05
3	1.000E-08 - 7.500E-09	5.61E-05
4	2.530E-08 - 1.000E-08	4.81E-04
5	3.000E-08 - 2.530E-08	1.86E-04
6	4.000E-08 - 3.000E-08	4.45E-04
7	5.000E-08 - 4.000E-08	5.04E-04
8	7.000E-08 - 5.000E-08	1.16E-03
9	1.000E-07 - 7.000E-08	2.07E-03
10	1.500E-07 - 1.000E-07	4.19E-03
11	2.000E-07 - 1.500E-07	4.97E-03
12	2.250E-07 - 2.000E-07	2.74E-03
13	2.500E-07 - 2.250E-07	2.90E-03
14	2.750E-07 - 2.500E-07	3.05E-03
15	3.250E-07 - 2.750E-07	6.51E-03
16	3.500E-07 - 3.250E-07	3.45E-03
17	3.750E-07 - 3.500E-07	3.58E-03
18	4.000E-07 - 3.750E-07	3.70E-03
19	6.250E-07 - 4.000E-07	3.82E-02
20	1.000E-06 - 6.250E-07	8.01E-02
21	1.770E-06 - 1.000E-06	2.15E-01
22	3.000E-06 - 1.770E-06	4.50E-01
23	4.750E-06 - 3.000E-06	8.16E-01
24	6.000E-06 - 4.750E-06	6.87E-01
25	8.100E-06 - 6.000E-06	1.32E+00
26	1.000E-05 - 8.100E-06	1.36E+00
27	3.000E-05 - 1.000E-05	2.10E+01
28	1.000E-04 - 3.000E-05	1.33E+02
29	5.500E-04 - 1.000E-04	1.89E+03
30	3.000E-03 - 5.500E-04	2.40E+04
31	1.700E-02 - 3.000E-03	3.24E+05
32	2.500E-02 - 1.700E-02	2.73E+05
33	1.000E-01 - 2.500E-02	4.26E+06
34	4.000E-01 - 1.000E-01	3.07E+07
35	9.000E-01 - 4.000E-01	6.71E+07
36	1.400E+00 - 9.000E-01	6.70E+07
37	1.850E+00 -1.400E+00	5.36E+07
38	2.354E+00 -1.850E+00	5.03E+07
39	2.479E+00 - 2.354E+00	1.09E+07
40	3.000E+00 - 2.479E+00	3.87E+07
41	4.800E+00 - 3.000E+00	7.06E+07
42	6.434E+00 - 4.800E+00	2.02E+07
43	8.187E+00 - 6.434E+00	6.43E+06
44	2.000E+01 - 8.187E+00	2.22E+06
Total		4.23E+08

APPENDIX C

TOTAL ABSORPTION CROSS-SECTION FOR CADMIUM

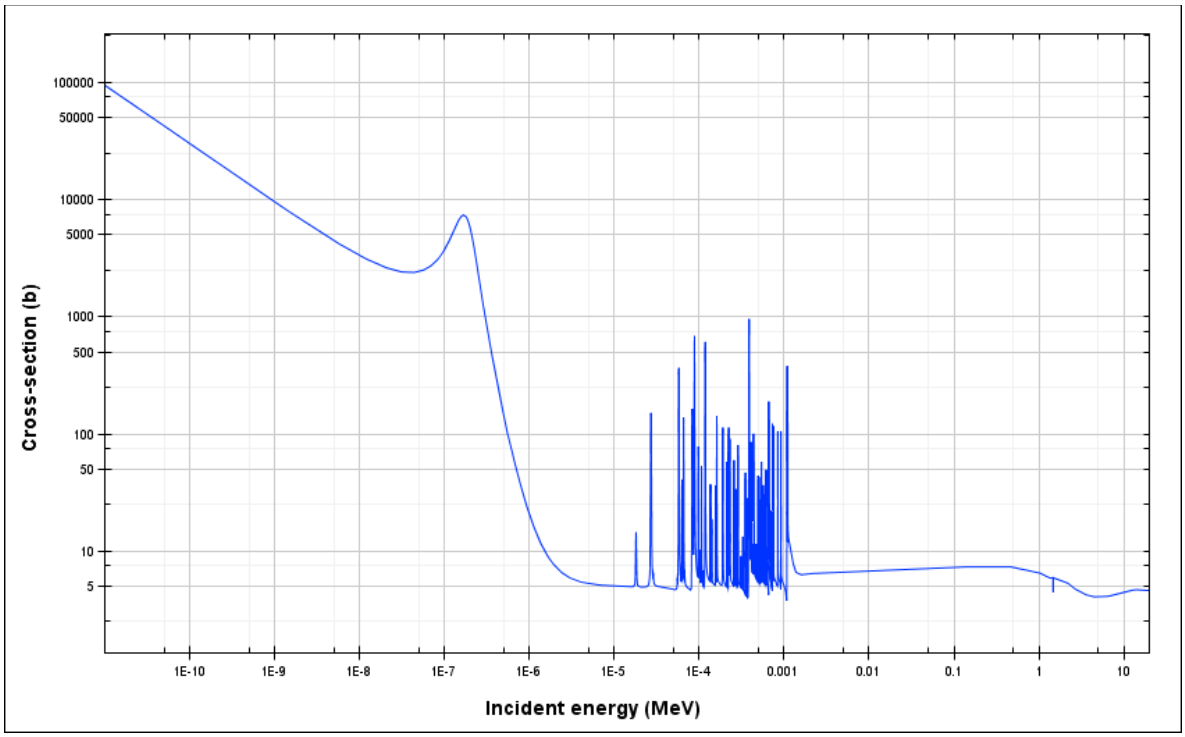

APPENDIX D

MCNP INPUT FILE FOR THE SIMPLIFIED DRY CASK MODEL

```
c    -- Cell Cards --
924   4  -1.205e-3  -601 -623  +107                                imp:n=1
925   5  -7.92       -601 -624  +623                                imp:n=1
926   4  -1.205e-3  -601 -625  +624 #201 #202 #203                 imp:n=1
929   8  -2.55       -601 -627  +625                                imp:n=1
930   5  -7.92       -601 -628  +627                                imp:n=1
201   9  -0.93       -201 +202 -203 +204 +624 -205 #202 #203       imp:n=1
202   0              -206 -208 +209                                 imp:n=1
203   0              -207 -208 +209                                 imp:n=1
931   0              -999 (+601:-107:+628)                          imp:n=0
999   0             +999                                            imp:n=0

c   -- Surface Cards --
107   pz   406.3
c
c   -Outer cylinders-
601   c/z   90.69552076 90.69552076 83.05637951
c
c    -Top and bottom layers-
623   pz   429.59
624   pz   453.59
625   pz   471.59
627   pz   491.59
628   pz   494.13
201   px   113.6955208
202   px   67.69552076
203   py   113.6955208
204   py   67.69552076
205   pz   460.39
206   c/y  102.2133682 456.99 2.4
207   c/y  79.17767324 456.99 2.4
208   py   102.1955208
209   py   79.19552076
c
c   -Problem boundary-
999   s    90.69552076 90.69552076 0 20000

c    -- Data Cards --
MODE n
SSR  OLD=107 NEW=107 PTY=N
f4:n   202
f14:n  203
fm4    1.76E+11
fm14   1.76E+11
e0     6E-08  3E-07  15E-06  1.6E-03    2E+01
```

```
m4     6000.66c  0.000151     $Air
       7014.66c  0.784437
        8016.66c  0.210750
      18000.35c  0.004671
m5    24000.50c  0.202087    $ Stainless Steel
      25055.50c  0.020133
      26000.50c  0.688268
      28000.50c  0.089514
m8    14000.50c -0.315          $Concrete
      13027.66c -0.048
        8016.66c -0.5
         1001.66c -0.006
      11023.66c -0.017
      20000.66c -0.083
      26000.50c -0.012
      19000.66c -0.019
m9     1001.66c -0.143716      $Polyethylene
       6012.50c -0.856284
NPS   1E8
PRDMP -60 -60
```

APPENDIX E

DIVERSION ANALYSIS RESULTS FOR THE FISSION CHAMBERS IN GRAPHICAL FORM AND RELATED NUMERICAL DATA

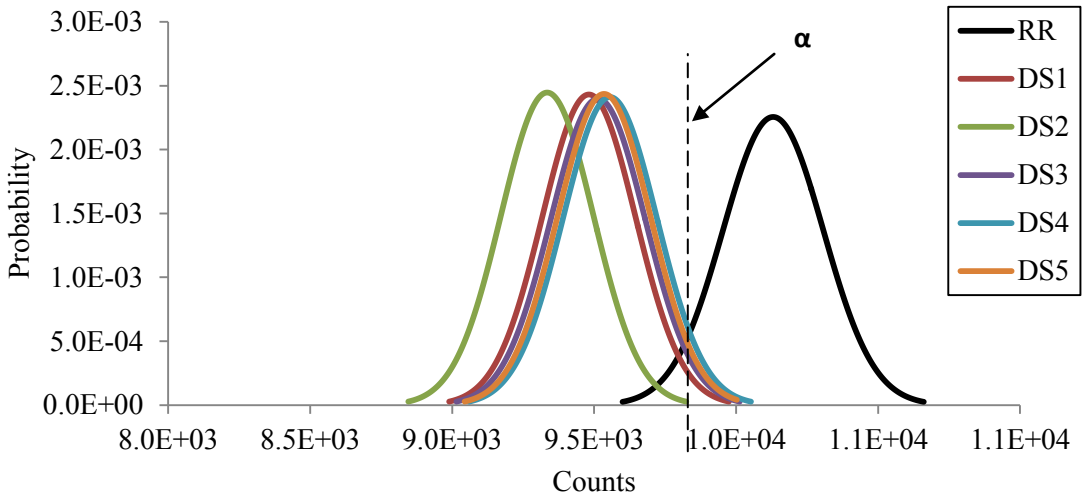

Fission chamber readings for the diversion scenarios #1-5 where one SNF assembly was removed. Measurement time – 1 (s)

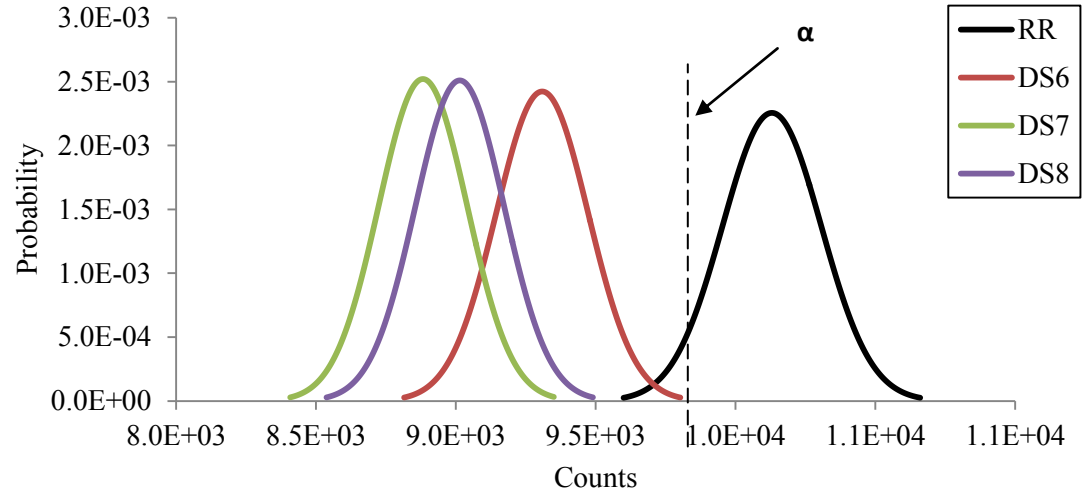

Fission chamber readings for the diversion scenarios #6-8 where two SNF were removed. Measurement time – 1 (s)

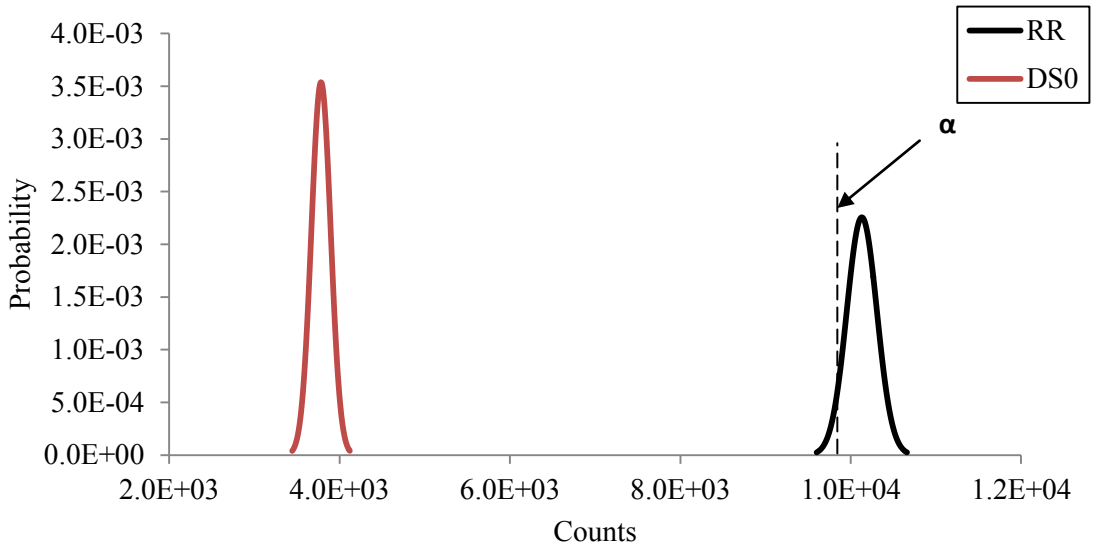

Fission chamber readings for the open lid case. Measurement time – 1 (s)

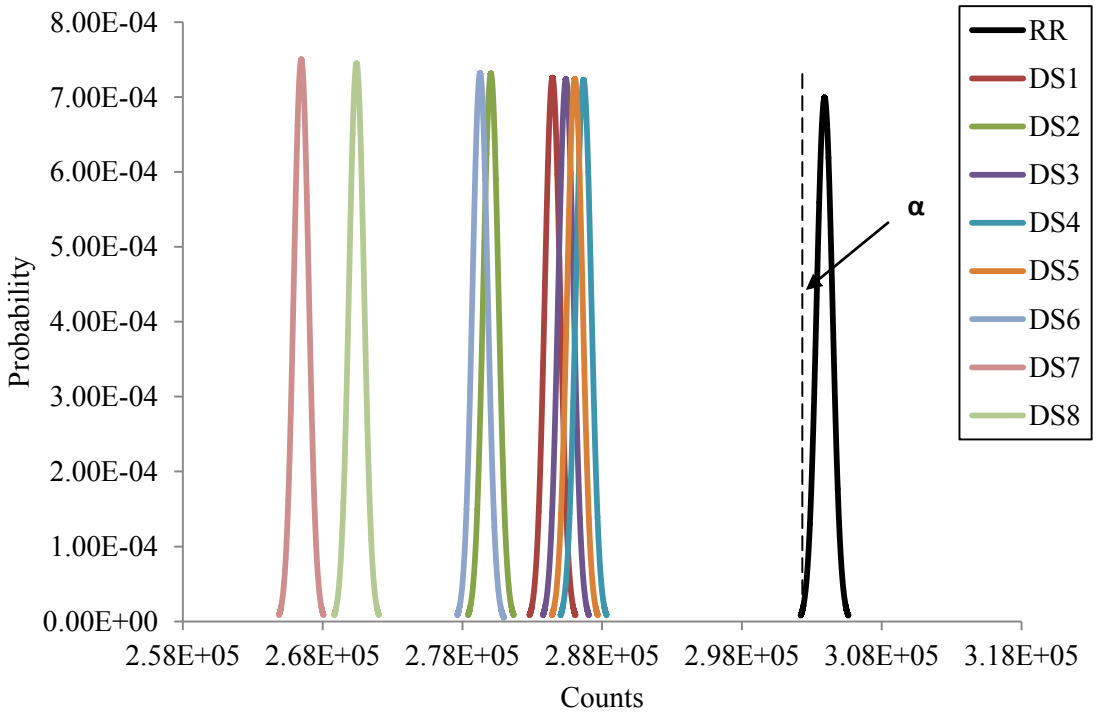

Fission chamber readings for the diversions scenarios #1-8. Measurement time – 30 (s)

Fission chamber readings and related uncertainty for diversion analysis results with neutron radiation signal and one SNF assembly removed

Measurement time 1 (s)	RR	DS1	DS2	DS3	DS4	DS5
Counts (mean)	1.01E+04	9.48E+03	9.33E+03	9.51E+03	9.56E+03	9.53E+03
MCNP uncertainty	1.45E+02	1.32E+02	1.31E+02	1.35E+02	1.33E+02	1.31E+02
Virtual measurement uncertainty	1.01E+02	9.74E+01	9.66E+01	9.75E+01	9.78E+01	9.76E+01
Total uncertainty	1.77E+02	1.64E+02	1.63E+02	1.66E+02	1.65E+02	1.64E+02

Measurement time 30 (s)	RR	DS1	DS2	DS3	DS4	DS5
Counts (mean)	3.04E+05	2.84E+05	2.80E+05	2.85E+05	2.87E+05	2.86E+05
MCNP uncertainty	1.45E+02	1.32E+02	1.31E+02	1.35E+02	1.33E+02	1.31E+02
Virtual measurement uncertainty	5.51E+02	5.33E+02	5.29E+02	5.34E+02	5.35E+02	5.35E+02
Total uncertainty	5.70E+02	5.49E+02	5.45E+02	5.51E+02	5.52E+02	5.51E+02

Fission chamber readings and related uncertainty for diversion analysis results with neutron radiation signal for two SNF assemblies removed and open lid scenario

Measurement time 1 (s)	RR	DS6	DS7	DS8	DS0 (Open lid)
Counts (mean)	1.01E+04	9.31E+03	8.88E+03	9.01E+03	3.78E+03
MCNP uncertainty	1.45E+02	1.33E+02	1.27E+02	1.27E+02	9.45E+01
Virtual measurement uncertainty	1.01E+02	9.65E+01	9.42E+01	9.49E+01	6.15E+01
Total uncertainty	1.77E+02	1.65E+02	1.58E+02	1.59E+02	1.13E+02

Measurement time 30 (s)	RR	DS6	DS7	DS8	DS0 (Open lid)
Neutron flux value (mean)	3.04E+05	2.79E+05	2.66E+05	2.70E+05	1.13E+05
MCNP uncertainty	1.45E+02	1.33E+02	1.27E+02	1.27E+02	9.45E+01
Virtual measurement uncertainty	5.51E+02	5.28E+02	5.16E+02	5.20E+02	3.37E+02
Total uncertainty	5.70E+02	5.45E+02	5.32E+02	5.35E+02	3.50E+02

APPENDIX F

DIVERSION ANALYSIS RESULTS FOR THE IONIZATION CHAMBERS IN GRAPHICAL FORM AND RELATED NUMERICAL DATA

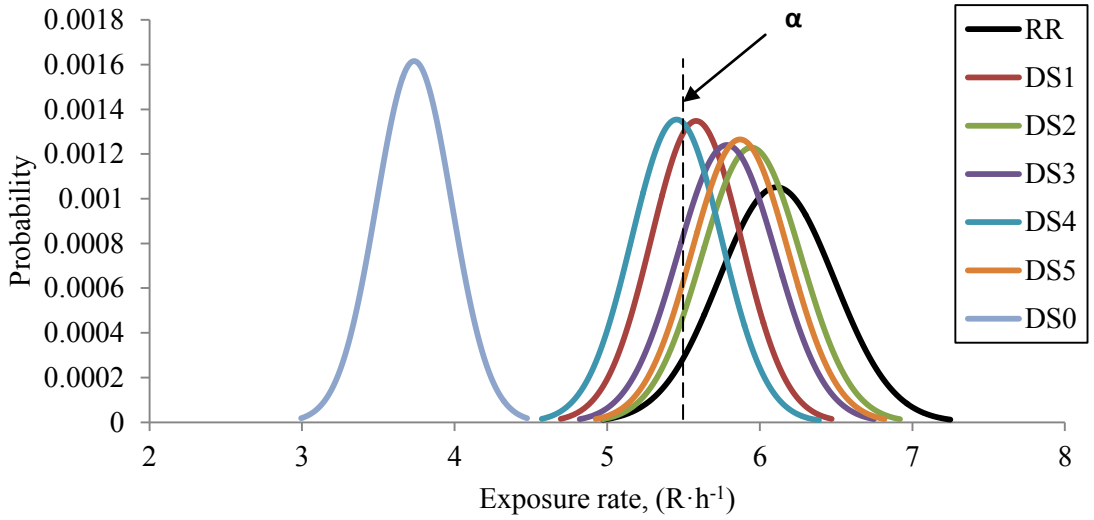

Central ionization chamber readings for the diversion scenarios #1-5 where one SNF assembly was removed and for open lid scenario

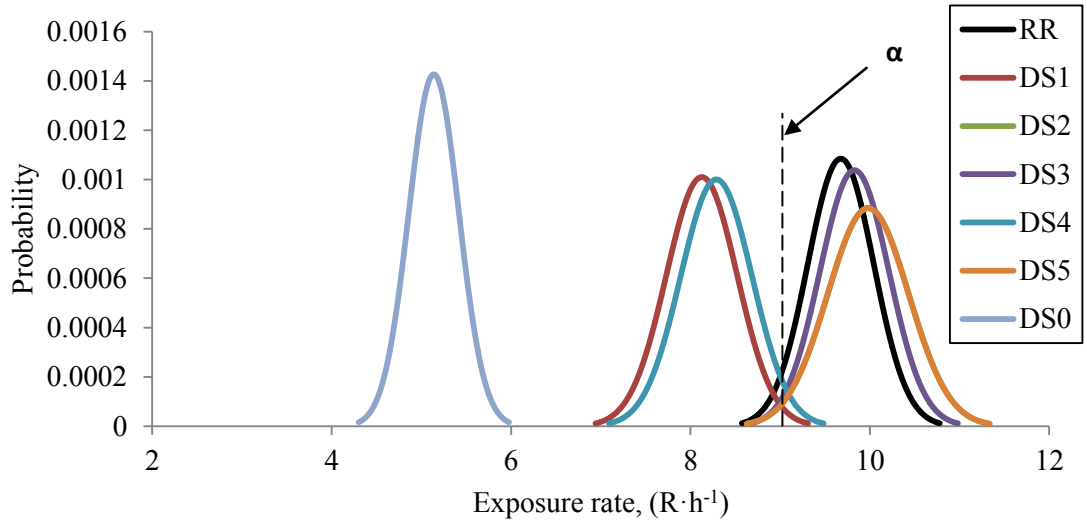

Edge ionization chamber readings for the diversion scenarios #1-5 where one SNF assembly was removed and for open lid scenario

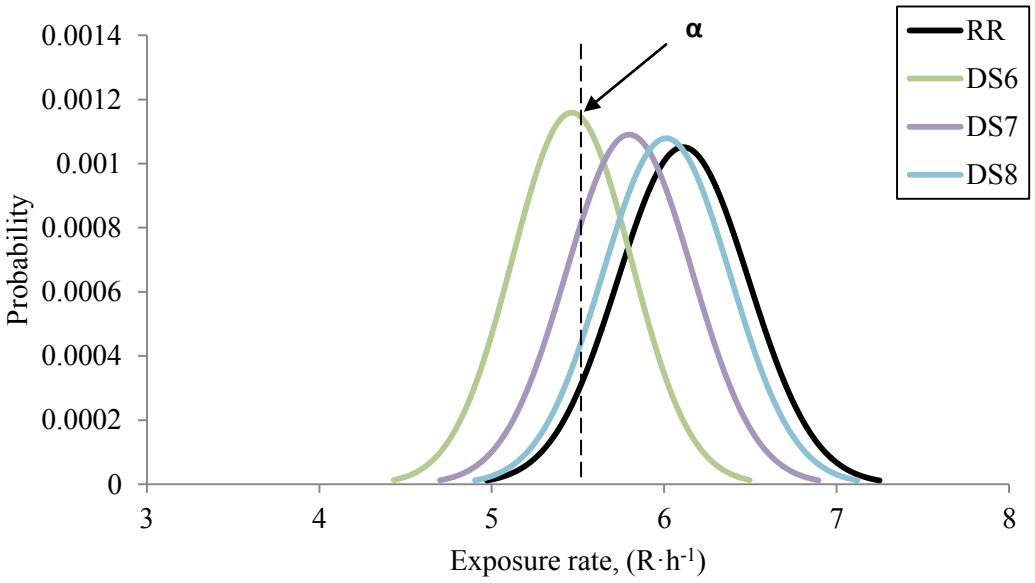

Diversion analyses results for the ionization chamber located in the center position (two assemblies removed)

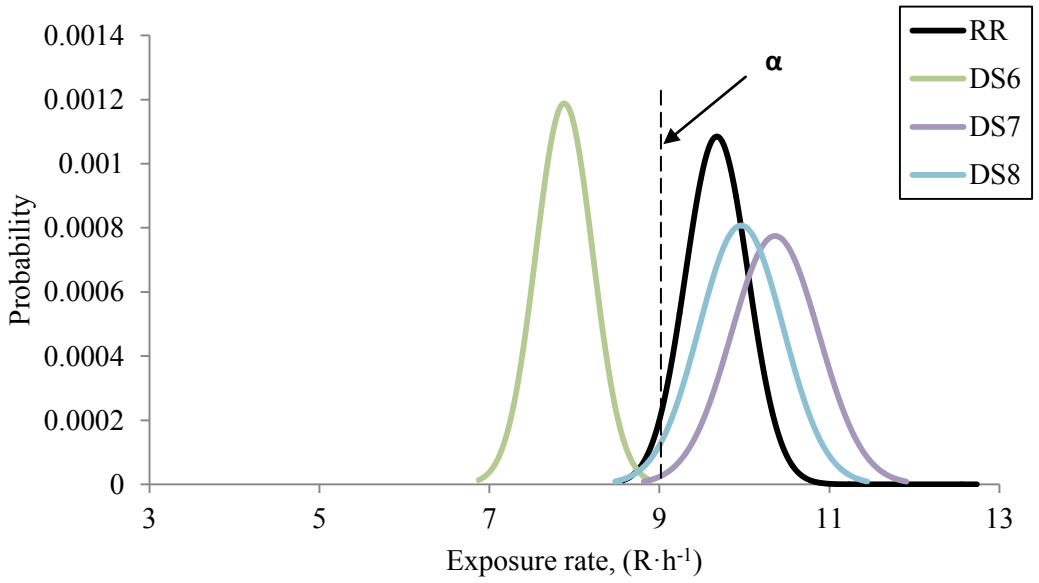

Diversion analyses results for the ionization chamber located in the edge position (two assemblies removed)

Ionization chamber readings and related uncertainty for diversion analysis results with gamma radiation signal and one SNF assembly removed

Central location	RR	DS1	DS2	DS3	DS4	DS5
Exposure rate (mean)	6.110	5.583	5.945	5.784	5.455	5.871
MCNP uncertainty	0.379	0.296	0.325	0.322	0.295	0.315
Virtual measurement uncertainty	0.306	0.279	0.297	0.289	0.273	0.294
Total uncertainty	0.487	0.407	0.440	0.433	0.401	0.431

Edge location	RR	DS1	DS2	DS3	DS4	DS5
Counts (mean)	9.676	8.126	9.982	9.828	8.289	9.981
MCNP uncertainty	0.368	0.395	0.451	0.384	0.399	0.451
Virtual measurement uncertainty	0.484	0.406	0.499	0.491	0.414	0.499
Total uncertainty	0.608	0.567	0.673	0.624	0.575	0.673

Ionization chamber readings and related uncertainty for diversion analysis results with gamma radiation signal for two SNF assemblies removed and open lid scenario

Central location	RR	DS6	DS7	DS8	DS0 (Open lid)
Exposure rate (mean)	6.110	5.464	5.798	6.012	3.735
MCNP uncertainty	0.379	0.344	0.366	0.370	0.247
Virtual measurement uncertainty	0.306	0.273	0.290	0.301	0.187
Total uncertainty	0.487	0.439	0.467	0.477	0.310

Edge location	RR	DS6	DS7	DS8	DS0 (Open lid)
Exposure rate (mean)	9.676	7.881	10.361	9.962	5.139
MCNP uncertainty	0.368	0.336	0.515	0.494	0.280
Virtual measurement uncertainty	0.484	0.394	0.518	0.498	0.257
Total uncertainty	0.608	0.518	0.730	0.702	0.380